2018

Computational study of flow past arrays of plates in the vicinity of surfaces

I-HAN LIU
Lehigh University

Computational study of flow past arrays of plates in the vicinity of surfaces

by

I-Han Liu

A Dissertation

Presented to the Graduate and Research Committee

of Lehigh University

in Candidacy for the Degree of

Doctor of Philosophy

in

Mechanical Engineering

Lehigh University

(May 2018)

Approved and recommended for acceptance as a dissertation in partial fulfillment of the requirements for the degree of Doctor of Philosophy

I-Han Liu
Computational study of flow past arrays of plates in the vicinity of surfaces

_____
Defense Date

_____
Dissertation Director
Dr. Alparslan Oztekin

_____
Approved Date

Committee Members:

_____
Dr. Yaling Liu

_____
Dr. Natasha Vermaak

_____
Dr. Tara Troy

ACKNOWLEDGMENTS

I would like to express my sincere appreciation to my advisor Dr. Alparslan Oztekin for his continuous support and guidance in my research. Without his help, this work would not have been possible. I am also grateful to my committee members, Dr. Yaling Liu, Dr. Natasha Vermaak, and Dr. Tara Troy, for their help in preparation of this dissertation. Thanks to my colleagues for their collaboration, encouragement, and companionship during my study in Lehigh. Working with them as a team has helped me get through those difficult times in research. In addition, I would like to thank my parents for their unconditional love and support in my life.

TABLE OF CONTENTS

LIST OF TABLES

LIST OF FIGURES

ABSTRACT

Flows past bluff bodies are encountered in many engineering applications. The bluff body situated in the flow experience a significant amount of pressure drag force. Therefore, it is important to predict flow conditions around bluff bodies when designing bridges, platforms, pipelines near seabed, offshore structures, and hydropower systems. In several engineering applications, structures could often be placed near surfaces. Transient flows past rectangular plates in the vicinity of surfaces are investigated in this study. Flow patterns and hydrodynamic forces acting on the plates become increasingly complicated due to the interactions between the plates and the surfaces. The study of free surface and wall proximity effects reveals that the drag exerted on the plates is sensitive to the submergence depth and the wall gap. Asymmetric flow patterns and an increase in drag coefficient of the plate are observed when the plate is placed near the surface. The array configuration of yawed plates provides distinct properties than tandem arrangements of plates, which are placed perpendicular to the flow. The yawed plates can be placed in a tighter arrangement without a significant penalty on drag reduction. Furthermore, with suitable spacing, the surface proximity effects increase the drag force exerted on plates when compared to those placed away from the wall. This study can help in optimizing the power generation of marine current energy harvesting systems, which consist of translating blades that operate in rivers or beneath offshore platforms.

CHAPTER 1 INTRODUCTION

1.1 Motivation

Flows past multiple bluff bodies are encountered in many engineering applications, such as chimney stacks, buildings, bridges, and offshore structures. Offshore structures such as marine current energy harvesting devices are often placed in multiple units in an array configuration. Turbulent wake flows generated by upstream units will increase the fluctuation of hydrodynamic forces on downstream units and thus can compromise the durability of structures. Rectangular plates placed perpendicular to the flow direction are simple geometries used in this study to understand complex phenomena such as flow separation, wake instabilities, unsteady vortex shedding formation, and forces acting on the plates. Understanding the solid-fluid interactions in flows past structures are important when designing and optimizing marine current devices.

In most of the hydraulic engineering applications, structures are often operated near surfaces. The flow structure near the body is expected to be influenced by the presence of the rigid surface. For example, when an energy harvesting device is operating beneath an offshore platform or near a seabed, interactions between the wake flow induced by the blades and the flow inside a boundary layer could influence the hydrodynamic loadings on the blade. Vortex shedding patterns induced by the blade become asymmetric due to the interference of the solid surface. If the blades are placed near a surface, vortex shedding can be completely disrupted and suppressed. Similarly, structures such as bridges and hydropower systems can often interact with the free surface. Therefore,

characterizing flow dynamics around the structures while under the free surface effect is another important issue. Estimating structural hydrodynamic forces is necessary for designing consideration for offshore structures under unsteady flow operation conditions. Hydrokinetic turbines for river current applications typically operate near free surfaces and the effect of the free surface on the performance of these energy harvesting devices could be profound. A single flat plate submerged at different water depths and wall gaps are investigated here to understand the influence of the free surface and a rigid wall on the flow field around the body.

Despite extensive studies of flows past bluff bodies in the literature, the understanding of flow structures around finite plates under surface effects are still limited. Simulations performed in this dissertation can be a preliminary study of a potential linear energy harvesting device, which consists of multiple translating blades. The concept of such system is illustrated in Figure 1. As shown in Figure 1(b), the bottom half of the device is submerged in the flow, and the blades inside the water are fully submerged. Blades of this device are connected to a belt and are pushed by the flow, which in turn converts the kinetic energy of water into mechanical energy. This device can be operated either in a river close to a free surface or mounted underneath an offshore platform. The primary objective of this study is to investigate the surface proximity effect on the flow dynamics around a single and arrays of plates. Therefore, results obtained from simulations conducted in this dissertation can be beneficial when designing such energy harvesting devices.

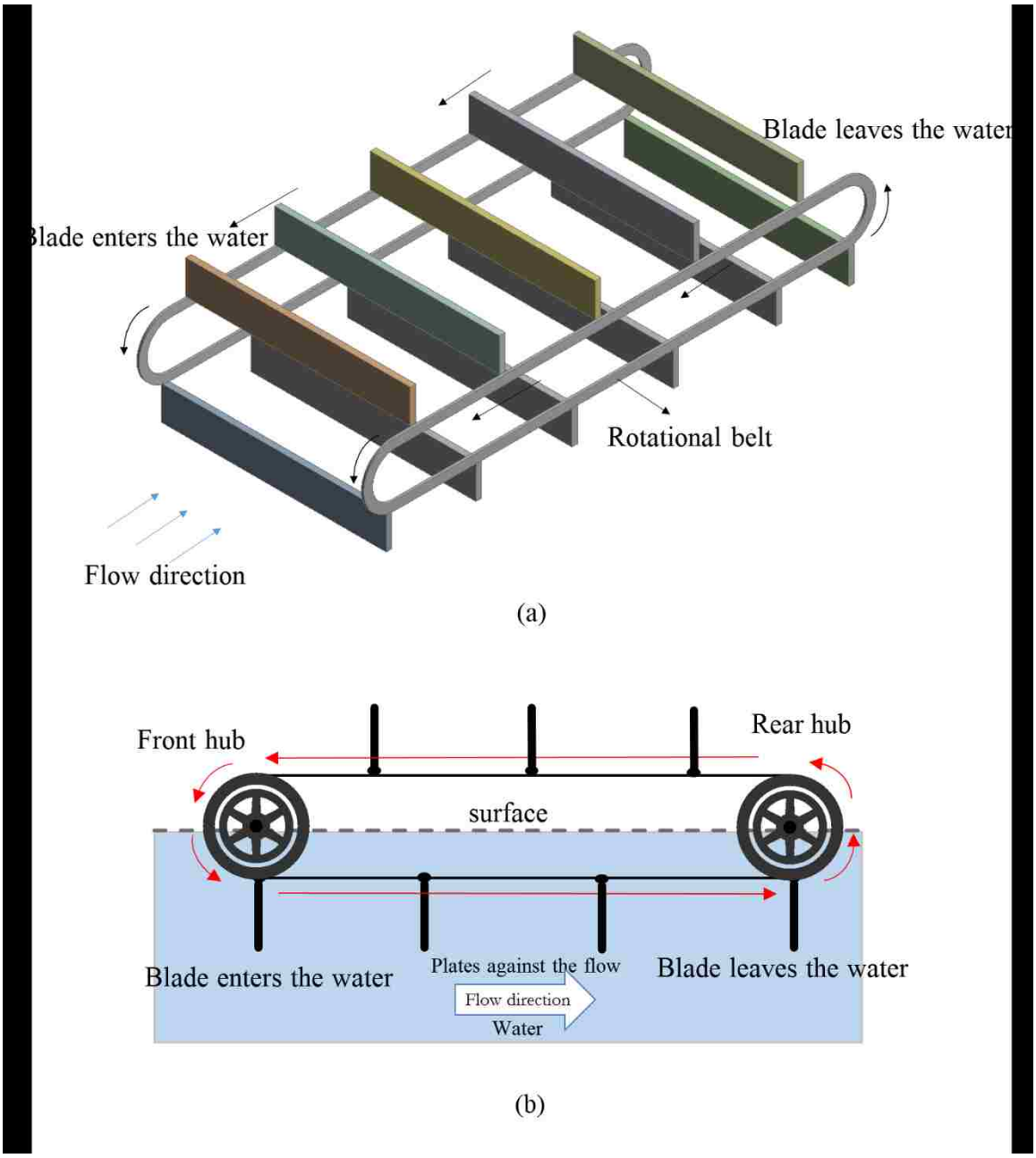

Figure 1. Concept of energy harvesting system in (a) three-dimensional view (b) side view.

1.2 Literature Review

Flow past bluff bodies in an infinite fluid domain have been widely studied both experimentally and numerically. Simple geometries such as circular cylinders, rectangular prisms, and flat plates have been investigated to understand the vortex dynamics in the flow field, and hydrodynamic forces exerted on a body. An object is considered as a bluff body when a significant pressure drag is involved while the object is exposed to wind or water flows [1]. Researchers have conducted experiments in a wind tunnel or a water channel to investigate flows past bluff bodies. Fage and Johansen [2] and Kisely [3] experimentally studied flows past rectangular prisms. They found that the incline angle and the aspect ratio of prisms influence pressure around the prism and the Strouhal numbers. More recently, Narasimhamurthy and Andersson, Najjar and Vanka, and Tian *et al*. [4-6] numerically studied the structure and dynamics of the wake flow behind a flat plate. The mean drag coefficients vary with respect to different aspect ratio of the plate is reported.

When multiple prisms are in the field with proximity to each other, flow structures become more complex because of the interactions between wake flows and prisms. Prisms situated downstream interfere with the wake flow structure induced by upstream prisms. This interaction has a profound influence on the drag and the lift forces exerted on prisms. Flows past multiple prisms in the tandem arrangement are classical flow problems in engineering applications and have been studied by many investigators [7-10].

It is well documented that flow patterns are strongly dependent on the spacing ratio, G/D, where G is the gap between two successive infinite prisms, and D is the diameter of the prism. Different flow regimes are encountered depending on values of G/D. Three types of wake behavior are classified [11-13]. At low values of G/D, the vortex shedding from the upstream prism is suppressed. Two prisms act like a single body because the shear layer separated from the upstream prism wraps around the downstream prism. At intermediate values of G/D, the vortex shedding from the downstream prism synchronized with shedding from the upstream prism. At larger values of G/D, Karman vortex streets generated from upstream and downstream prisms hardly interfere with each other. Critical values of G/D can be identified as wake flow transitions from one pattern to another [13]. Drag and lift coefficients and Strouhal number display rapid changes at around the critical values of G/D, as reported in Sakamoto *et al*. [7] and Liu and Chen [8]. Several investigators have reported hydrodynamic loads in flows past arrays of tandem cylinders at various values of G/D. An extensive review of this topic is given by Sumner [11]. For lower and intermediate values of G/D, C_D of the upstream cylinder in an array is lower than C_D of the single cylinder at the same Reynolds number (Re). C_D of the upstream cylinder increases as G/D is increased. At values of G/D near criticality, C_D of the upstream prism increases rapidly. A sudden increase in C_D coincides with wake flow pattern changes induced by the Karman vortex shedding. Vortex shedding is set off from both upstream and downstream prisms for G/D around the critical value. As G/D is increased beyond the critical value, C_D gradually approaches the value of C_D in flows past a single prism. Generally

speaking, C_D of the downstream prism is lower than that of the upstream prism due to wake effects [10].

In several engineering applications, prisms could often be placed near a free surface or a rigid surface. Recently, Malavasi and Guadagnini [14] and Liu *et al.* [15] have documented that hydrodynamic forces acting on a rectangular prism decrease as the prism is placed closer to a free surface. The presence of the free surface breaks the symmetry of vortex shedding, resulting in irregular hydrodynamics. Similarly, when the prism is near a rigid surface, both the hydrodynamic forces acting on the prism and the flow patterns downstream of the prism are altered depending on the distance between the prism and the surface. Past studies [16-20] have reported that the regular pattern of the vortex street is broken when the sharp-edged plate is nearby of a rigid surface. Due to the wall boundary layer influence, characteristics of the top and the bottom shear layers differ significantly, which results in distorted vortex shedding from the top and the bottom of the prism [21]. Bosch *et al*., Agelinchaab *et al*., and Shi *et al*. [18, 20, 22] performed experiments to study flows past a rectangular prism above a plane boundary. Bosch *et al*. [18] found that vortex shedding is suppressed at critical gaps less than $0.35D$, where D is the height of the prism. Agelinchaab *et al*. and Shi *et al*. [20, 22] reported that due to the strong interaction between the wake and the wall, regular vortex shedding becomes very weak or it is completely suppressed. The suppression of vortex shedding in flows past a square cylinder near a wall is also documented in the numerical investigation by Bhattacharyya and Maiti [16]. Vortices shed from the wall side of the prism are stretched and migrated away from the wall, resulting in oblique wake structure. This indicates that

vortices near the wall transfer energy in a longitudinal direction [20]. Recently, Bayraktar *et al*. [23] conducted simulations for flows past a rectangular prism under the influence of a wall. They reported that the interaction between induced vortices by the plate and vortices induced by the wall dominates flow structures near the plate and downstream of the plate. They also reported that vortex shedding is suppressed when the gap is smaller than the critical value. As the prism is placed away from the wall the wake flow asymptotically approaches that of flows past a plate in an unbounded domain.

Hydrodynamic forces exerted on a prism are sensitive to the proximity of a plate to a rigid surface. Several studies have investigated the wall effects on hydrodynamic forces around a prism. They reported a decrease in drag coefficient, C_D, when the cylinder is placed near the wall. The reduction of drag coefficient is associated with the change of near wake flow structures around the cylinder, and base pressure increases as the gap between the prism and the wall decreases. Numerical studies by Kumaran and Vengadesan [24] and Mahir [19], and experimental observation by Martinuzzi *et al*. [25] showed that both drag and lift in flows past a sharp-edged prisms are strongly influenced by the presence of the wall. They concluded that the decrease in drag coefficient is directly related to the suppression of vortex shedding. Bayraktar *et al*. [23] also reported a decrease in drag coefficient when the gap between a square cylinder and the wall is decreased. In addition to drag force, they also reported intensified vortex shedding when the gap is increased.

Free surface flows are challenging hydraulic engineering scenarios. For instance, the forces acting on the cylinder become increasingly complicated due to the interaction

between the free surface and the cylinder. Also, the wake behind structures and water surface deformation are altered in such free surface scenarios as well. Several researchers approached this problem numerically [26-28] and experimentally [14, 26, 27, 29-31] by employing circular or rectangular prisms.

Generally, hydrodynamic forces acting on the object decreases when the object is closer to the surface, as described in Miyata *et al*. and Malavasi and Guadagnini [14, 26]. A simultaneously occurring abrupt drop in drag coefficient and increase in Strouhal number is reported. Malavasi and Guadagnini [14] experimentally investigated a rectangular prism submerged in a water channel at various depths. They found that the drag coefficient decreases drastically and Strouhal number increases with decreasing depth of the prism at small depths. Both Miyata *et al*. and Sheridan *et al*. [26, 29] studied the wake structure of flow past a circular cylinder close to the free surface. The presence of the cylinder, which caused the formation of surface waves, altered the dynamics of the free surface and produced a jet-like flow near the free surface. When the cylinder is shallowly submerged, the free surface distortion and asymmetric vortex shedding from the cylinder occurred. Such asymmetric vortex shedding resulted in intense turbulent fluctuations due to the flow confinement on top. Another study on the free surface deformation and wake behavior with respect to Froude number are presented in Reichl *et al*. [30] and Arslan *et al*. [27]. Results of two-dimensional simulations showed that the surface deformation is sensitive to the Froude number. The surface deformation and the intensity of surface waves became substantial as the Froude number increased. The magnitude of the drag force is also very sensitive to the submergence ratio.

Aforementioned studies consider prisms whose axes are perpendicular to the oncoming flow. Flows past an infinite yawed prism are also well documented. Shirakashi *et al*. [32] conducted experiments in flows past a yawed cylinder and reported that the vortex shedding becomes irregular and the vortex shedding frequency is lower for the yawed cylinder compared to that for the perpendicular cylinder. Numerical investigations of flows past a yawed cylinder reported by Yeo and Jones [33] concluded the swirling flow around the cylinder is responsible for generating low-frequency loadings. Zhao *et al*. [34] performed direct numerical simulation to study the effects of the yaw angle on wake structures, vortex shedding frequencies, and hydrodynamic forces. They have documented that vortices shed from the cylinder propagate along the axis of the cylinder while they are convected downstream. They also reported that the drag coefficient increases gradually as the incline angle is increased. The yaw angle in these studies is defined as the angle between the oncoming flow direction and the direction perpendicular to the axis of the prism. Jordan [35] investigated flow past yawed cylinders at the angle of 45º and 60º as referenced to the flow direction. Jordan [35] characterized the flow transition to turbulence in the wake of yawed cylinders.

Despite extensive studies in flow past infinite prisms (cylinders), many actual structures should be modeled as a finite rectangular prism with free ends. Several investigators studied flows past a finite-length prism or a cylinder with one free end [36-38]. Sumner [39], recently reported a comprehensive review on the subject. To date, there are not many investigations considering flows past multiple bluff bodies with two free ends.

Flow patterns in the wake of finite prisms with free ends are fully three-dimensional. The wake flow field is characterized by both the alternating Karman vortex shedding that occurs along the prism and the tip vortices formed at free ends [40]. Wang *et al*. [36] experimentally studied interactions between the boundary layer and the wake of a wall-mounted finite square prism. They concluded that the highly three-dimensional flow patterns around a finite square prism were induced by the Karman vortex along the surface of the prism and tip and base vortices within the wake. Rostamy *et al*. [41] conducted experiments for finite square prisms of various length-to-diameter (L/D) ratios. Their results showed aspect ratio has a profound influence on the velocity field around free ends. The wake is dominated by tip vortices at lower values of L/D, while for higher values of L/D, the Karman vortex shedding from the prism sides dominates the wake flow pattern.

The drag coefficient of finite length cylinder for different values of L/D has been reported extensively. C_D is decreased as L/D is decreased [37, 42-44]. Zdravkovich *et al*. [42] carried out experiments on a finite length circular cylinder with two free ends for various values of L/D. It is observed that C_D decreases with decreasing L/D. In-flow around cylinder ends causes an increase of pressure at the back side of the cylinder, which in turn reduces the drag coefficient. Strouhal number (St) varies with L/D. Vortex shedding behind the prism becomes more irregular due to the presence of unstable tip vortices. Wang and Zhou [44] experimentally studied the near wake of a finite length square cylinder. They reported that the spatial wake configuration is dependent on the interaction between Karman vortex shedding (asymmetric flow pattern) and the tip

vortices (symmetric flow pattern). As L/D ratio is decreased, tip vortices dominate wake flow patterns. Symmetrical vortex patterns correspond to weaker stresses, which lead to lower C_D compared to infinitely long cylinders. They concluded that the presence of tip vortices contributes to the decrease of C_D monotonically with a decrease of L/D. There are only a few studies of flows past finite yawed prisms. As reported by Hu *et al*. [45], the flow field in the vicinity of a finite prism differs from that of an infinite prism. Large eddy simulations presented by Hu *et al.* [45] revealed that the drag coefficient of the finite yawed prism decreased as the yaw angle (as specified, an angle from the vertical axis) is increased. Down-wash and up-wash flow behind the yawed cylinder resulted in downward and upward axial flows, respectively. Vortex pairs at the free end also cause a decrease in shedding frequency.

1.3 Objective

The present study focuses on investigating wall proximity effect and free surface effect for flows past a single and arrays of finite plates. Turbulence models such as Reynolds-Averaged Navier Stokes (RANS) equations, Large Eddy Simulations (LES) and Volume of Fluid (VOF) multiphase model were employed to characterize the flow field. The change of hydrodynamic forces, wake structures, pressure on the plate's surfaces, and free surface deformation were investigated. All these complex flow phenomena will be discussed in details in the following chapters.

Various wall distances of the plate were considered to study the wall proximity effect. The boundary layer thickness was calculated in order to characterize the critical wall distance. Simulations for several plate depths were conducted to investigate free surface effect. Plate depths were characterized by Froude number. Different spacing ratios between the upstream and the downstream plates were examined in simulations for arrays of plates. Wall proximity effect was studied for arrays of yawed plates. Understanding the influence of surface effects on the plate and the flow fields were able to aid in designing marine structures such as energy harvesting devices.

CHAPTER 2 MATHEMATICAL MODEL

2.1 Turbulence Modeling

Turbulence is an irregular fluid flow that has complex fluid dynamic phenomena. Flow separation, unsteady vortex shedding, and large-scale turbulent structures are involved in flows past bluff bodies. The numerical solution is often used to predict such flow physics and the hydrodynamic forces exerted on the body. Reynolds averaged Navier-Stokes (RANS) model and Large Eddy Simulation (LES) are commonly employed turbulence methods to simulate these complex flow problems. RANS model directly predicts the averaged flow field without resolving the large-scale eddies. The averaging approach is an easier way to solve and represent the flow. This model requires less computational resource, but it has difficulties when encountered complex phenomena. LES, on the other hand, is more suitable in problems like flow past bluff bodies because the large scales are resolved by solving Navier-Stokes equations, while only the small scales turbulent motion is modeled using filtering approach. This method is good in capturing large-scale eddy structures, especially when unsteady vortex shedding and dynamic loadings on the body are significant in the problem.

2.2 Reynolds Averaged Navier-Stokes Equations

The k-ω model is an effective turbulence model in predicting flow separation. The two equation k-ω model solves for the turbulence kinetic energy and the specific dissipation rate. The k-ω SST model has been formulated to avoid the upstream

sensitivity of the standard *k-ω* model by combining the advantages of the *k-ω* model and *k-ε* model. The equations for turbulent kinetic energy and specific dissipation rate are written in the following form [46-48] :

$$\frac{\partial k}{\partial t} + u_j \frac{\partial k}{\partial x_j} = \tau_{ij} \frac{\partial u_i}{\partial x_j} - \beta^* k\omega + \frac{\partial}{\partial x_j}\left[(\nu + \sigma_k \nu_T)\frac{\partial k}{\partial x_j}\right] \quad (1)$$

$$\frac{\partial \omega}{\partial t} + u_j \frac{\partial \omega}{\partial x_j} = aS^2 - \beta\omega^2 + \frac{\partial}{\partial x_j}\left[(\nu + \sigma_\omega \nu_T)\frac{\partial \omega}{\partial x_j}\right] + 2(1 - F_1)\sigma_{\omega 2}\frac{1}{\omega}\frac{\partial k}{\partial x_i}\frac{\partial \omega}{\partial x_i} \quad (2)$$

The eddy viscosity and the extra stress tensor are defined as

$$\nu_T = \frac{a_1 k}{\max(a_1\omega, \Omega F_2)} \quad (3)$$

$$\tau_{ij} = \nu_T\left(\frac{\partial u_i}{\partial x_j} + \frac{\partial u_j}{\partial x_i} - \frac{2}{3}\frac{\partial u_k}{\partial x_k}\delta_{ij}\right) - \frac{2}{3}k\delta_{ij} \quad (4)$$

Here, Ω is the vorticity magnitude, $a, a_1, \beta, \beta^*, \sigma_k, \sigma_\omega, \sigma_{\omega_2}$ are closure coefficients, ν is the kinematic viscosity, k is the turbulent kinetic energy, ω is the specific dissipation rate, u_j is the velocity, S is the mean rate-of-strain tensor, and F_1, F_2 are the blending functions. Details of the closure parameters can be found in [47]. Recently, this turbulence model is successfully employed by investigators to characterize turbulent flow structures near micro-hydro turbines [49-53].

2.3 Large Eddy Simulations

Large eddy simulation approach applies spatial filtering to the Navier-Stokes equation. The large-scale eddies are resolved numerically and the smaller scale eddies – eddies that are smaller than the grid size - are not resolved, but are approximated.

Resolving the large scale motions enables LES to predict instantaneous flow characteristics and to resolve turbulent flow structures.

Time- and spatial-averaged Navier-Stokes equations with low pass filtering yield

$$\frac{\partial \bar{u}_j}{\partial x_j} = 0 \tag{5}$$

$$\frac{\partial \rho \bar{u}_i}{\partial t} + \frac{\partial \rho \bar{u}_j \bar{u}_i}{\partial x_j} = -\frac{\partial \bar{p}}{\partial x_i} - \frac{\partial \tau_{ij}}{\partial x_j} + \mu \frac{\partial^2 \bar{u}_i}{\partial x_j \partial x_j} + \rho g \tag{6}$$

where $\bar{u}_j = u_j - \acute{u}_j$ represents the filtered velocity vector and the over bar denotes filtering operator; ρ is the fluid density; and $\bar{p}$ is the resolved pressure.

The subgrid shear stress $\tau_{ij} = \overline{u_i u_j} - \bar{u}_j \bar{u}_i$ is calculated using the subgrid-scale (SGS) models. Employing the Boussinesq hypothesis the SGS turbulent stress is computed from

$$\tau_{ij} - \frac{1}{3}\tau_{kk}\delta_{ij} = -2\nu_t \bar{S}_{ij} \tag{7}$$

where δ_{ij} is the Kronecker delta; ν_t is the SGS eddy viscosity; and $\bar{S}_{ij} = \frac{1}{2}\left(\frac{\partial \bar{u}_i}{\partial x_j} + \frac{\partial \bar{u}_j}{\partial x_i}\right)$ is the rate-of-strain tensor.

The wall-adapting local eddy-viscosity (WALE) method is used to model the SGS eddy viscosity [54]:

$$\nu_t = L_s^2 \frac{\left(S_{ij}^d S_{ij}^d\right)^{3/2}}{\left(\bar{S}_{ij}\bar{S}_{ij}\right)^{5/2} + \left(S_{ij}^d S_{ij}^d\right)^{5/4}} \tag{8}$$

$$S_{ij}^d = \frac{1}{2}\left(\left(\frac{\partial \bar{u}_i}{\partial x_j}\right)^2 + \left(\frac{\partial \bar{u}_j}{\partial x_i}\right)^2\right) - \frac{1}{3}\delta_{ij}\left(\frac{\partial \bar{u}_k}{\partial x_k}\right)^2 \tag{9}$$

$$L_s = min\left(\kappa y, C_w \mathrm{V}^{1/3}\right) \tag{10}$$

Here L_s is the mixing length for subgrid scales; κ is the von Karman constant; y is the shortest distance to the wall; the WALE constant C_w is 0.325; and V is the mesh cell volume. Details of the WALE model are documented by [54].

2.4 Multiphase Model – Volume of Fluid (VOF)

The VOF method models two immiscible fluids by solving mass and momentum conservation equations. The volume fraction of each fluid in cells can be tracked throughout the domain. The air volume fraction is defined by a scalar function α, which is the volume of air divided by the volume of the local cell. Volume fraction is bounded between $0 \leq \alpha \leq 1$, corresponding to water-filled cells and air-filled cells, respectively. When $0 < \alpha < 1$, the cell contains the interface between air and water. α is expressed as

$$\alpha = \frac{\forall_{air}}{\forall_{cell}} = \frac{\forall_{air}}{\forall_{air}+\forall_{water}} \tag{11}$$

where $\forall_{cell}$ is the volume of a cell, $\forall_{air}$ is the volume of air within the cell, and $\forall_{water}$ is the volume of the water within the cell. The mass and momentum equations for multiphase flow are written as [55, 56]

$$\frac{\partial \rho}{\partial t} + \frac{\partial \rho u_i}{\partial x_i} = 0 \tag{12}$$

$$\frac{\partial}{\partial t}(\rho u_i) + \frac{\partial}{\partial x_j}(\rho u_j u_i) = -\frac{\partial P}{\partial x_i} + \frac{\partial}{\partial x_j}\left[\mu\left(\frac{\partial u_j}{\partial x_i} + \frac{\partial u_i}{\partial x_j}\right)\right] + \rho g \tag{13}$$

where u_i is the velocity, ρ is the density, μ is the dynamic viscosity, P is the pressure, and g is gravity. The density of the mixture is defined in terms of α as

$$\rho = \alpha\rho_1 + (1-\alpha)\rho_2 \tag{14}$$

where ρ_1 denotes the density of the primary phase (air) and ρ_2 denotes the density of the secondary phase (water). Interface tracking between water and air is accomplished by solving the continuity equation for the phase's volume fraction, which has the following form:

$$\frac{\partial}{\partial t}(\alpha\rho_1) + \frac{\partial}{\partial x_i}(\alpha\rho_1 u_1) = 0 \tag{15}$$

where u_1 represents the velocity of the primary phase.

Two or more fluids can be depicted in the VOF model by solving a single set of momentum equations and tracking the volume fraction of each fluid throughout the domain. The implicit scheme is used for time discretization for obtaining the face fluxes for all cells:

$$\frac{\alpha_1^{n+1}\rho_1^{n+1} - \alpha_1^n\rho_1^n}{\triangle t}\forall_{cell} + \sum_f\left(\rho_1^{n+1}U_f^{n+1}\alpha_{1,f}^{n+1}\right) = 0 \tag{16}$$

where $n+1$ denotes the index for current time step while n denotes the index for previous time step. $\alpha_{1,f}$ is the face value of the air volume fraction, and U_f is the volume flux through the face based on normal velocity.

2.5 Dimensionless Parameters

The Reynolds number is based on the upstream water velocity U_∞ and the plate height D. It is calculated as $Re = \rho U_\infty D / \mu$, where ρ is the density of the water and μ is water dynamic viscosity. In order to find out how much energy can be extracted, the

force acting on the plate must be determined. The drag and lift coefficients (C_D and C_L) are defined as

$$C_D = \frac{F_D}{\frac{1}{2}\rho U_\infty{}^2 A}, C_L = \frac{F_L}{\frac{1}{2}\rho U_\infty{}^2 A} \quad (17)$$

where F_D is the drag force, F_L is the lift force, and A is the area of the immersed object projected over the incoming flow.

Strouhal number, $St = fD / U_\infty$, is the dimensionless number utilized in the flow characterization of oscillating flow mechanics, where f is the frequency of fluctuating lift coefficient, C_L, and is calculated by performing fast Fourier transform to the time signature of C_L. Non-dimensional time and non-dimensional time step are defined as $\lambda = tU_\infty / D$ and $\Delta\lambda = \Delta t U_\infty / D$, respectively.

Open channel flow, such as rivers and spillways, involve the existence of a free surface between air and water. In these cases, the free surface behavior becomes important. The flow is governed by the forces of gravity and inertia, and it can be characterized by the dimensionless parameter, Froude Number, $Fr = U_\infty / \sqrt{gd}$, where d is the distance between free surface and the plate tip. The Froude number based on d basically represents the local Froude number and is suitable to characterize the effect of the free surface on the physics of flows near the submerged object [29].

CHAPTER 3 THREE-DIMENSIONAL TRANSIENT FLOWS PAST A SINGLE PLATE AND ARRAYS OF YAWED PLATES

This chapter focuses on the characterization of three-dimensional transient flows past arrays of yawed prisms in different arrangements. Simulations employing LES approach are carried out to study the wake flow patterns and their influence on drag coefficients in flows past a single and multiple finite length plates with two free ends. The drag coefficient of prisms in various arrays is presented. The spacing ratio, G/D, and the yaw angle, θ, are varied and their influence on the flow structures is presented. To the best knowledge of the author, three-dimensional flows past arrays of yawed prisms with tandem and staggered arrangements have not been considered previously. This study can aid designing and optimizing marine current energy harvesting devices by characterizing wake flow patterns and their influence on the forces exerted on structures.

3.1 Computational Overview

LES for flows past plates are conducted at Re = 50,000. The schematic of the three-dimensional computational domain is shown in Figure 2(a-c) while the top views (x-z plane) are shown in Figure 2(d-e). Figure 2(a,d) show prisms that are arranged in a tandem array and situated perpendicular to the oncoming flow. Figure 2(c,e) shows plates that are arranged in a staggered array and placed against the oncoming flow with a yaw

angle, θ. The yaw angle in the present study is defined as the angle between the axis of the plate and the oncoming flow direction. The geometry of a single prism is depicted in Figure 2(b). The length, height, and width of the prism are L, D, and w, respectively. The spacing between two successive prisms, G, and the yaw angle, θ, are illustrated in Figure 2. For staggered arrays, distance from prism tip to the centerline is defined as e. Simulations for flows past staggered arrays of prisms are conducted for a fixed value of e. Prisms in tandem arrays are labeled as Pi while prisms in staggered arrays are labeled as Ai. Prisms are numbered in order from upstream to downstream. Values of physical properties and geometric and flow parameters used in the present simulations are listed in Table 1. Table 2 lists different prism array configurations. Each configuration has different spacing, G, yaw angle, θ, and number of prisms in the arrangement.

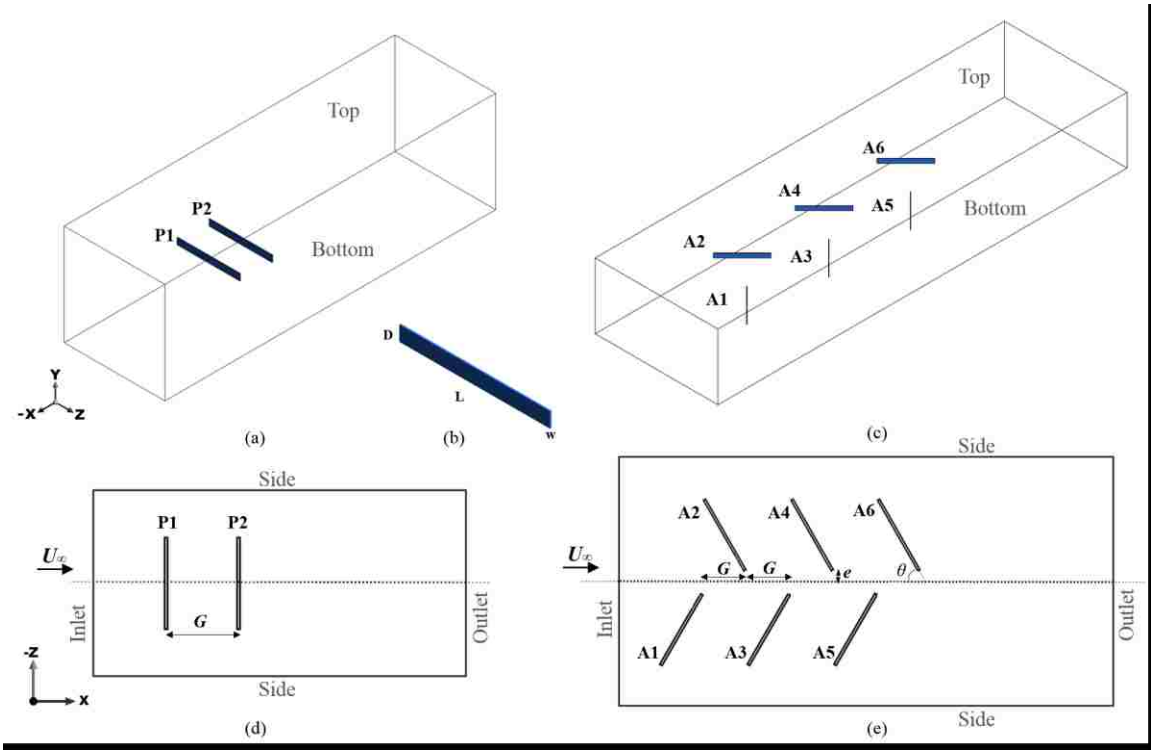

Figure 2. Schematic diagram of the plate arrays (a) in a tandem arrangement, (c) in a staggered arrangement, (d) in a tandem arrangement illustrated at $y = 0$ plane, and (e) in a staggered arrangement illustrated at $y = 0$ plane. (b) Schematic of a single plate geometry.

Table 1. Parameters used in the present study.

Parameter	*Values*				
D	0.1	[m]	U_∞	0.5	[m s^{-1}]
e	0.2	[m]	w	0.01	[m]
L	1	[m]	ρ	1000	[kg m^{-3}]
Re	50,000	[-]	μ	0.001	[kg m^{-1} s^{-1}]

Table 2. Various array arrangements of prisms.

	Spacing	**Angle**	**Prism label**							
	G	***θ***	**P1**	**P2**	**A1**	**A2**	**A3**	**A4**	**A5**	**A6**
Single prism in different angles										
Case 1	-	45˚	-	-	√	-	-	-	-	-
Case 2	-	60˚	-	-	√	-	-	-	-	-
Case 3	-	90˚	-	-	√	-	-	-	-	-
Two tandem prisms with different gaps										
Case 4	5*D*	90˚	√	√	-	-	-	-	-	-
Case 5	7*D*	90˚	√	√	-	-	-	-	-	-
Case 6	10*D*	90˚	√	√	-	-	-	-	-	-
Case 7	20*D*	90˚	√	√	-	-	-	-	-	-
Multiple staggered prisms with different gaps and angles										
Case 8	10*D*	45˚	-	-	√	√	-	-	-	-
Case 9	10*D*	60˚	-	-	√	√	-	-	-	-
Case 10	10*D*	45˚	-	-	√	√	√	√	-	-
Case 11	2.5*D*	45˚	-	-	√	√	√	√	-	-
Case 12	10*D*	60˚	-	-	√	√	√	√	-	-
Case 13	5*D*	45˚	-	-	√	√	√	√	-	-
Case 14	10*D*	45˚	-	-	√	√	√	√	√	√

The size of the computational domain varies among cases based on the configuration. For example, dimensions of the domain for case 5 are $52.5D \times 16D \times 16D$ while dimensions for case 11 are $60D \times 16D \times 30D$ in stream-wise, cross stream, and span-wise directions, respectively. For all cases, the length of the inlet region - distance from inlet to the closest upstream plate – is selected as $12D$ and the distance from outlet to the closest downstream plate is selected as $30D$ to minimize the influence of the imposed inlet and the outlet velocity boundary conditions on the flow field near plates.

3.2 Numerical Methods, Convergence, and Validation Studies

ANSYS FLUENT commercial software is utilized to conduct simulations. The semi-implicit method for pressure-linked equations (SIMPLE) solution algorithm that fully couples the velocity and the pressure field is employed to solve the mathematical model. The bounded central differencing and bounded second-order implicit scheme are used for discretizing momentum equation and time, respectively. Detailed descriptions of numerical schemes and simulation tools are provided in ANSYS theory guide and ANSYS user guide [57, 58].

The boundary conditions for simulations in ANSYS FLUENT are as follows. Mass flow rate is prescribed at the inlet while zero gauge pressure is applied at the outlet. No-slip and no-penetration boundary conditions are imposed along surfaces of prisms and top and bottom surfaces of the channel. Symmetry boundary conditions are imposed on the side surfaces of the computational domain.

OpenFOAM, an open source CFD software package, is used here to validate the numerical model implemented in ANSYS FLUENT. Flow geometries depicted in case 3 and case 5 are considered for the validation study. The “pimpleFoam” solver that combines the Pressure-Implicit with Splitting of Operators (PISO) and SIMPLE algorithms are employed. An adjustable time step function with a constraint in Courant number in pimpleFoam solver is employed to enhance numerical stability. Details of the methods are documented by Greenshields [59].

3.2.1 Spatial and Temporal Convergence

Mesh structures for cases 5 and 11 are shown in Figure 3. Finer mesh is used in regions near the surface of prisms to capture boundary layer separations and to resolve near wake flow patterns. Mesh becomes gradually coarser away from prisms, as depicted in Figure 3. A mesh optimization study is conducted for case 5. Meshes of different density generated are 1.2×10^6 elements (m_1), 2.4×10^6 elements (m_2), and 5.7×10^6 elements (m_3). The main difference between mesh m_1 and mesh m_2 is an increased number of cells in the region near the plates. The average value of drag coefficient for each prism in the array is calculated for m_1, m_2, and m_3. Drag coefficient is defined by $C_D = F_D/\left(\frac{1}{2}\rho U_\infty^2 A\right)$, where F_D is the drag force exerted by fluid on the prism and A is the area of the prism projected perpendicular to the oncoming flow. Non-dimensional time and non-dimensional time step are defined as $\lambda = tU_\infty/D$ and $\Delta\lambda = \Delta tU_\infty/D$, respectively.

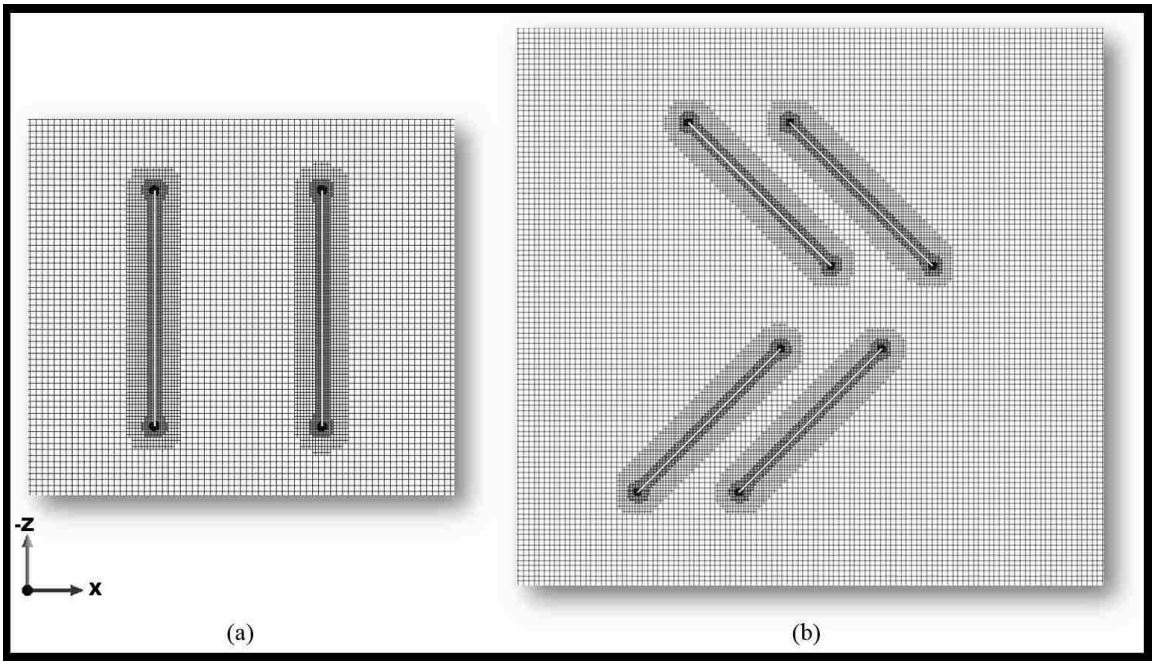

Figure 3. Examples of mesh around plates for (a) case 5 and (b) case 11. Images are taken at $y = 0$ plane.

The drag coefficient calculated by using FLUENT and OpenFOAM solver for case 5 is shown in Figure 4 as a function of time. $\Delta\lambda = 0.004$ is used for simulations conducted with FLUENT while adjustable time step is used for simulations conducted with OpenFOAM. Graphs in the left column denote drag coefficient of the upstream plate P1 and graphs on the right column denote drag coefficient of the downstream plate P2. Rows from top to bottom denote time signature of drag coefficient obtained using m_1, m_2, and m_3 mesh, respectively. The last two rows show drag coefficients predicted by OpenFOAM solver using m_1 and m_3 mesh density. Presence of irregular fluctuations in drag coefficient signal, as shown in Figure 4(a) and Figure 4(d), indicates alternating flow patterns in the wake region. Similar characteristics have been reported in flows past

a normal prism [60, 61]. In order to demonstrate if these flow patterns alternate periodically or irregularly, simulations need to be carried out with much larger flow times. Because of limited computational resources, present simulations are halted at λ = 700. High frequency fluctuations are detected in the signature of C_D for P2. This is because the fact that oncoming flows for P2 are highly turbulent wake flows induced by the presence of P1 in the field.

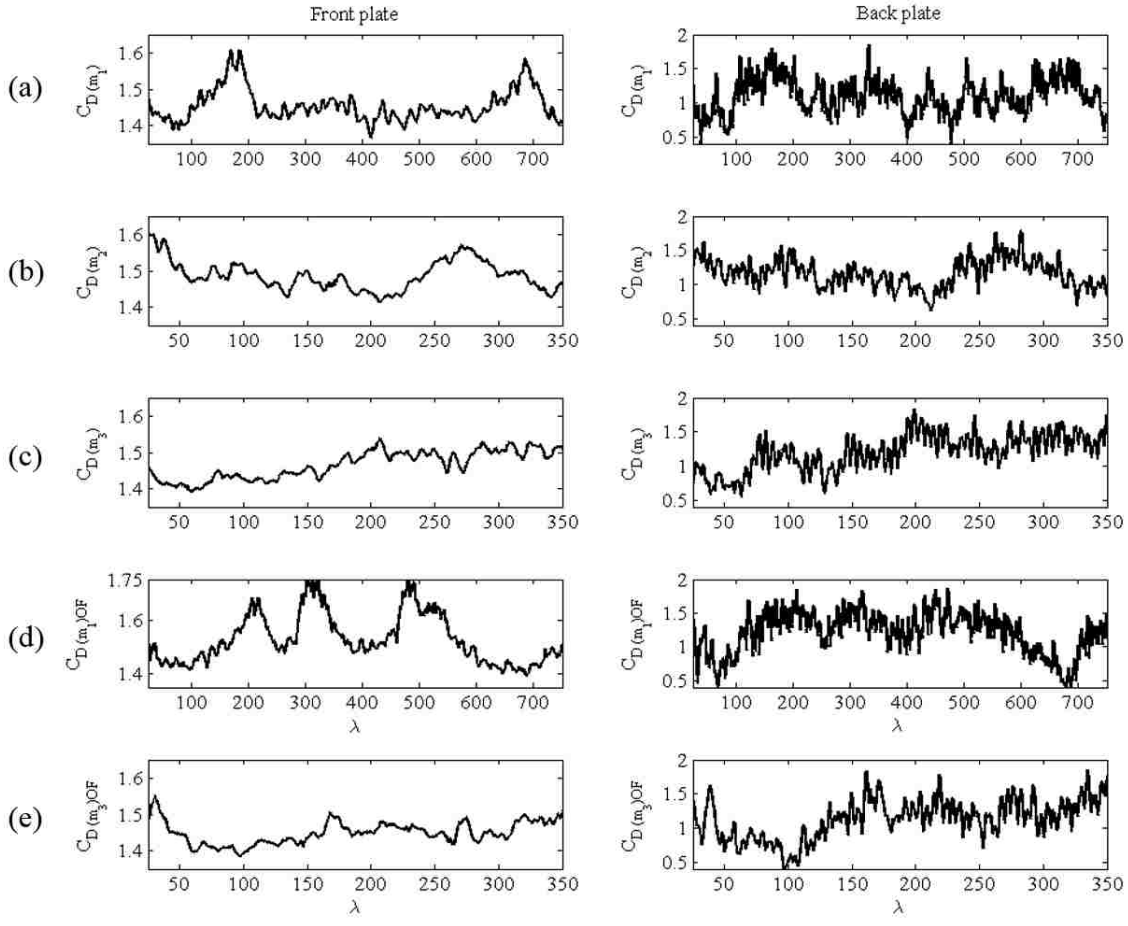

Figure 4. Drag coefficient as a function of time obtained with mesh (a) m_1, (b) m_2, and (c) m_3 by using FLUENT and obtained with (d) m_1 and (e) m_3 by using OpenFOAM.

Time-averaged values of drag coefficient, $\overline{C_D}$, and standard deviation of fluctuations predicted by FLUENT and OpenFOAM are listed in Table 3. Time steps and mesh density used are also listed in Table 3. Strouhal number is determined by performing fast Fourier transform to the time signature of the lift coefficient of P1 and P2. Strouhal numbers predicted using m_1, m_2, and m_3 are around 0.096, implying that time signature of hydrodynamic loadings is not sensitive to the mesh density. Strouhal number is defined by $St = fD/U_\infty$, where f is the frequency of fluctuating lift coefficient, C_L. Lift coefficient is defined by $C_L = F_L/\left(\frac{1}{2}\rho U_\infty^2 A\right)$, where F_L is the lift force exerted by fluid on the plate. The lift force acting on finite plates has more complicated dynamics when compared to that on infinite plates. Smaller amplitude fluctuations are observed in the time signature of drag coefficient for P1 compared to that for P2. That is attributed to the turbulent nature of induced wake flows as oncoming flows for P2 (see Figure 4). Time-averaged value of C_D for m_1, m_2, and m_3 are similar, as listed in Table 3. Drag coefficient for m_1 are also very close at $\Delta\lambda$ = 0.004 and at $\Delta\lambda$ = 0.012. Because of the irregular dynamics, root mean square values listed in Table 3 are relatively large, especially for P2 plate. It is demonstrated here that grid m_1 and time step of 0.004 are sufficient to ensure spatial and temporal convergence. Results presented in this chapter are obtained using mesh m_1 and $\Delta\lambda$ = 0.004. A stronger claim for spatial and temporal convergence could be made by refining the mesh further and using smaller time step. The level of computation and available computational resources make that a challenging task.

Table 3. Mean drag coefficient and root mean squre value of P1 and P2.

Case No.	Mesh Size	Solver	Time step $\Delta\lambda$	P1		P2	
				$\bar{C}_D$	C_{Drms}	$\bar{C}_D$	C_{Drms}
5	**m_1**	FLUENT	0.004	1.46	0.06	1.12	0.30
5	**m_1**	OpenFOAM	0.01	1.54	0.09	1.23	0.30
5	**m_2**	FLUENT	0.004	1.48	0.04	1.13	0.20
5	**m_3**	FLUENT	0.004	1.48	0.04	1.26	0.26
5	**m_1**	FLUENT	0.012	1.49	0.04	1.22	0.21
5	**m_3**	OpenFOAM	0.0025	1.45	0.03	1.17	0.27
3	**m_1**	FLUENT	0.004	1.51	0.04	-	-
3	**m_1**	OpenFOAM	0.007	1.47	0.04	-	-

Table 4 lists the maximum value of Courant number and y^+ values of P1 and P2 for test cases. Courant number, $C = u\Delta t/\Delta x$, is a non-dimensional stability indicator that shows if a solution satisfies the Courant-Freidrichs-Lewy (CFL) condition of $C \leq 1$. This condition ensures the numerical stability of simulations. Courant number in all test cases is bounded by 1.67, and the maximum value is only observed for few cells in the vicinity of the plates. y^+ value of P1 and P2 for m_1, m_2, and m_3 in case 5 range from 8 to 38. A smaller value of y^+ indicates a better quality of mesh. Mean drag coefficients of both prisms predicted using m_1 and m_3 mesh densities are very similar. Even though m_3 provides a better quality of mesh, grid m_1 is selected to conduct simulations here to reduce computational cost.

Table 4. Maximum value of Courant number and y^+ of P1 and P2.

Case No.	Mesh Size	Solver	Time step $\Delta\lambda$	C_{max}	P1	P2
					y^+	y^+
5	$\mathbf{m_1}$	FLUENT	0.004	0.34	30.03	33.65
5	$\mathbf{m_1}$	OpenFOAM	0.01	0.99	22.91	28.02
5	$\mathbf{m_2}$	FLUENT	0.004	0.79	10.09	26.07
5	$\mathbf{m_3}$	FLUENT	0.004	1.67	8.47	8.04
5	$\mathbf{m_3}$	OpenFOAM	0.0025	0.99	7.98	7.63
5	$\mathbf{m_1}$	FLUENT	0.012	1.11	31.95	38.01
3	$\mathbf{m_1}$	FLUENT	0.004	0.57	10.63	-
3	$\mathbf{m_1}$	OpenFOAM	0.007	0.99	8.97	-

Flow patterns and drag coefficients predicted by FLUENT and OpenFOAM solver for case 3 and case 5 are compared. Isosurfaces of vorticity, contours of vorticity, and velocity are depicted in Figure 5 for flows past two finite tandem plates (case 5). Isosurfaces of vorticity are presented at the Q-criterion of 0.01. The Q-criterion is the second invariant of the velocity gradient tensor that describes the vortex core regions (see ref. [62] for a detailed description). The Q-criterion is calculated by $\mathrm{Q} = -0.5(\|S\|^2 - \|\Omega\|^2)$, where S and Ω are the strain and the rotation tensor, respectively. Isosurfaces of the Q-criterion is colored with the normalized vorticity magnitude, $\omega D/U_\infty$, where ω is the vorticity magnitude. Images in the left column denote flow patterns predicted by FLUENT solver while images in the right column denote flow field predicted by OpenFOAM solver. Flow characteristics obtained by both solvers are very similar. Similar results are obtained for flow past a single plate (images not shown here). The time signature in drag coefficient predicted by both solver is also very similar, as shown in Figure 4. Drag coefficients predicted by FLUENT and OpenFOAM differ less than 6%

for P1 and less than 9% for P2 for case 5. The difference in the drag coefficient is less than 3% for case 3. Flow field and hydrodynamic loading predicted by each solver is nearly the same, validating the numerical methods employed here.

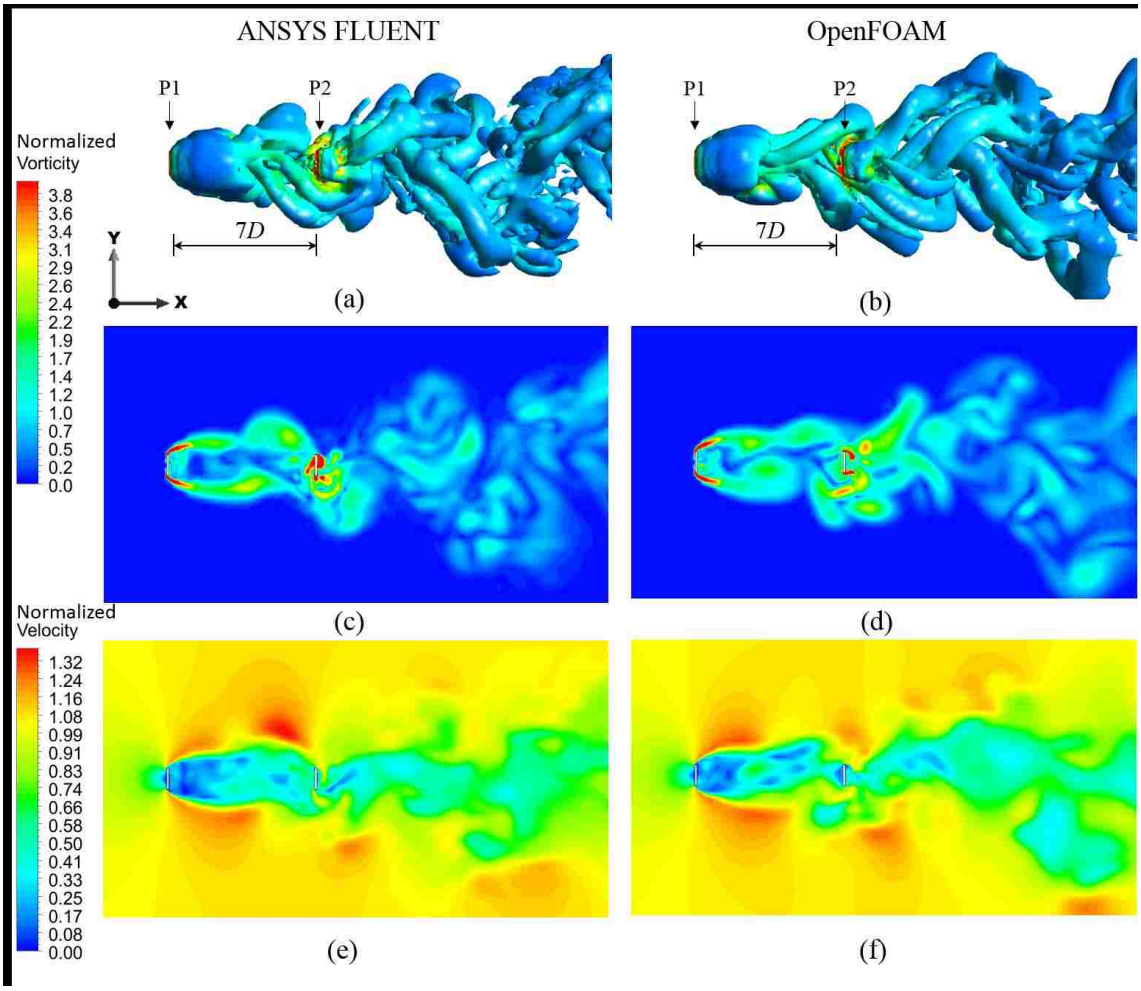

Figure 5. (a,b) Isosurface of vorticity at Q = 0.01, (c,d) contours of vorticity, and (e,f) contours of velocity acquired at y = 0 plane for case 5. Results are obtained by using (a,c,e) ANSYS FLUENT and by using (b,d,f) OpenFOAM solver.

3.2.2 Validation Study

A simulation is conducted for flows past two tandem square cross-sectioned prisms in order to validate mathematical models and numerical methods employed. Results are compared with experimental results reported by Liu and Chen [8]. The schematic of the computational domain used in the validation study is depicted in Figure 6(a) with the side view shown in Figure 6(b). The upstream and downstream plates are labeled as S1 and S2, respectively. The origin of the computational domain is located at the center of S1. The height of cylinders is defined as *h*, where *h* is 0.2m. The spacing between cylinders from center to center is 4.25*h*. Inlet is located at 18*h* upstream of the origin and the outlet is located at 37*h* downstream of the origin. The height of the computational domain is 15.25*h* and the length in the span-wise direction is 10*h*. Reynolds number is set to 2700.

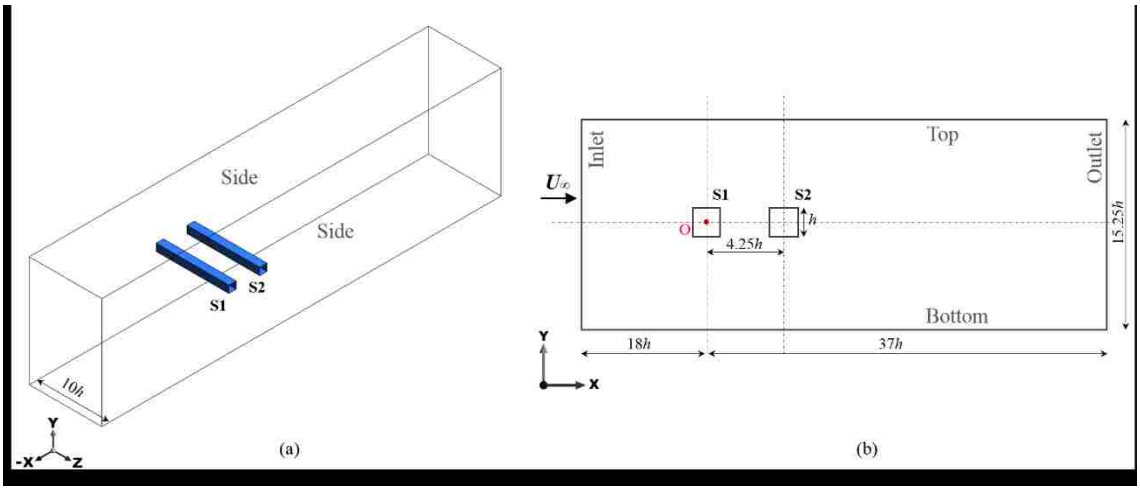

Figure 6. Schematic diagram of flows past two tandem square cross-sectioned plates in (a) a three-dimensional view and (b) a side view.

Drag and lift coefficients as a function of time and the pressure coefficient along the surface of the prisms are depicted in Figure 7. The hysteresis phenomenon induced by flow transition is observed at this spacing of prisms, as reported by Liu and Cheng [8]. Hydrodynamic loading on prisms changes drastically as flow transition occurs. Flow characteristics referred to as Mode I and Mode II are observed at different stages. Mode I is only observed at the early stage of the flow while Mode II becomes persistent after the onset of flow transition. The vorticity contours acquired at $y = 0$ plane demonstrate both flow patterns associated with Mode I and Mode II, as depicted in Figure 8. Similar to the observations, flow patterns associated with Mode I occur at the earlier stage then the flow pattern switches to Mode II following the flow transition. Flow patterns predicted by the present study match qualitatively with those reported in ref. [10] for each mode. Drag coefficient of S1 prism for flow Mode I is obtained as 1.67 while it is 2.07 for flow Mode II. Drag coefficient of S2 prism for flow Mode I and II are -0.03 and 0.8, respectively. These values match well with those documented in ref. [10]. Drag coefficient values reported in Liu and Cheng [8] for S1 prism are around 1.6 for flow Mode I and 1.9~2.1 for flow Mode II. C_D of S2 is around -0.4 for flow Mode I and 0.7 for flow Mode II. Slight deviations in drag coefficient for S2 prism can be attributed to the fact that finer mesh might be needed to determine complex unsteady wake flow structures near S2 prism, see Figure 8. Lift coefficients of both prisms transition to larger amplitude fluctuations as flow transition from Mode I to Mode II.

The pressure coefficient, C_p, is defined by $C_p = (p - p_\infty)/\left(\frac{1}{2}\rho U_\infty^2\right)$, where p_∞ is zero gauge pressure. The pressure is significantly greater along the front face of the prism

S1 and it decreases rapidly to a lower value at the side and back faces for both Modes I and II. The distribution of mean pressure coefficient predicted here along the surfaces of S1 and S2 are in good agreement with experimental results reported in ref. [10]. Overall, the hysteresis phenomenon, hydrodynamic loadings on prisms, and flow structures observed by Liu and Cheng [8] are predicted by the current study; validating mathematical models and numerical methods employed.

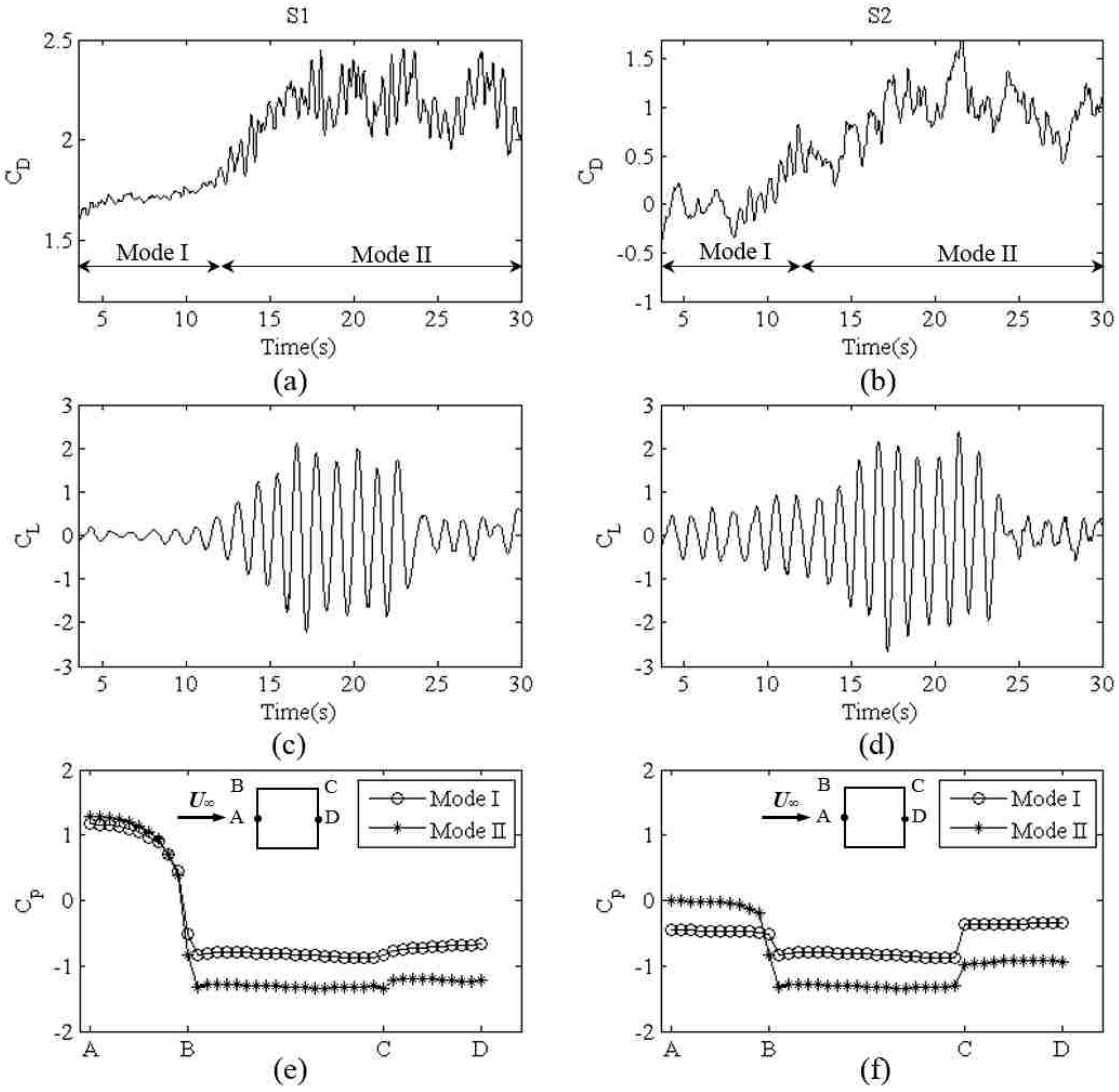

Figure 7. (a,b) Drag coefficient and (c,d) lift coefficient as a function of time, and (e,f) distribution of pressure coefficient along surfaces of prisms. Force coefficients are calculated for (a,c,e) S1 prism and for (b,d,e) S2 prism.

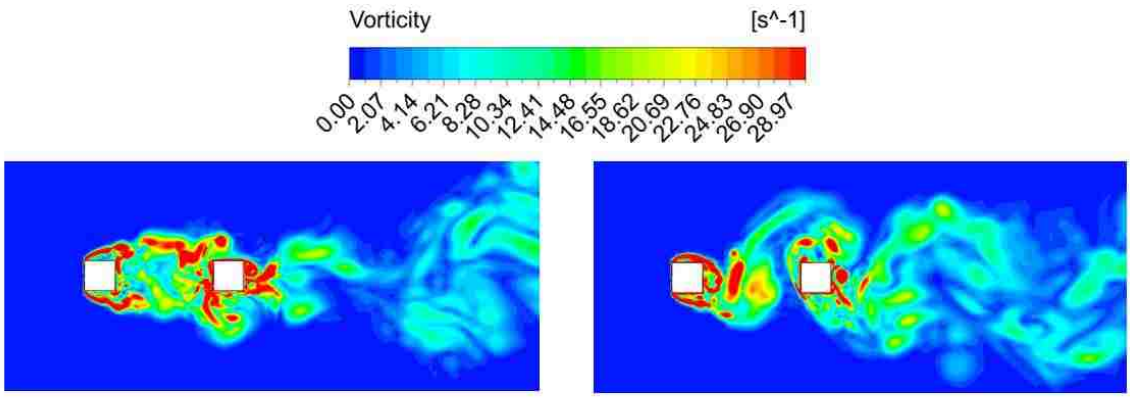

(a) *Mode I* (b) *Mode II*

Figure 8. Instantaneous vorticity contour acquired at y = 0 plane for (a) flow Mode I at 6.2 s and for (b) flow Mode II at 16.6 s.

3.3 Results and Discussions

3.3.1 Flows Past an Infinite and a Finite Plate

The drag coefficient of a finite prism is vastly different from that of infinitely long prism, as documented by several investigators. It is also well-documented that drag coefficient of finite cylinder strongly depends on the aspect ratio L/D. Transient simulations in three-dimensional geometry are conducted for flows past an infinitely long plate. Drag coefficients measured by Fage and Johansen [2] is 2.13 and predicted by Najjar and Vanka [5] and Tian *et al*. [61] are 2.26 and 2.30, respectively. The drag coefficient predicted by the current study is 2.22, which agrees well with those documented by previous investigators. As a base case (case 3), flows past a finite plate with L/D of 10 are simulated. The mean drag coefficient is calculated to be 1.5, which is 32% smaller than that of infinitely long plate. The tip vortices spawned from the plate's

free ends make the flow highly three-dimensional. Fluid passed the free ends and wrapped around the back of the plate. Such flow alters the pressure field and leads to a reduction in drag coefficient. Isosurfaces of vorticity at Q = 0.01 and the vorticity contour in flows past a finite and an infinite plate are depicted in Figure 9. Drag coefficient determined for case 3 is used as a reference in flows past tandem plates.

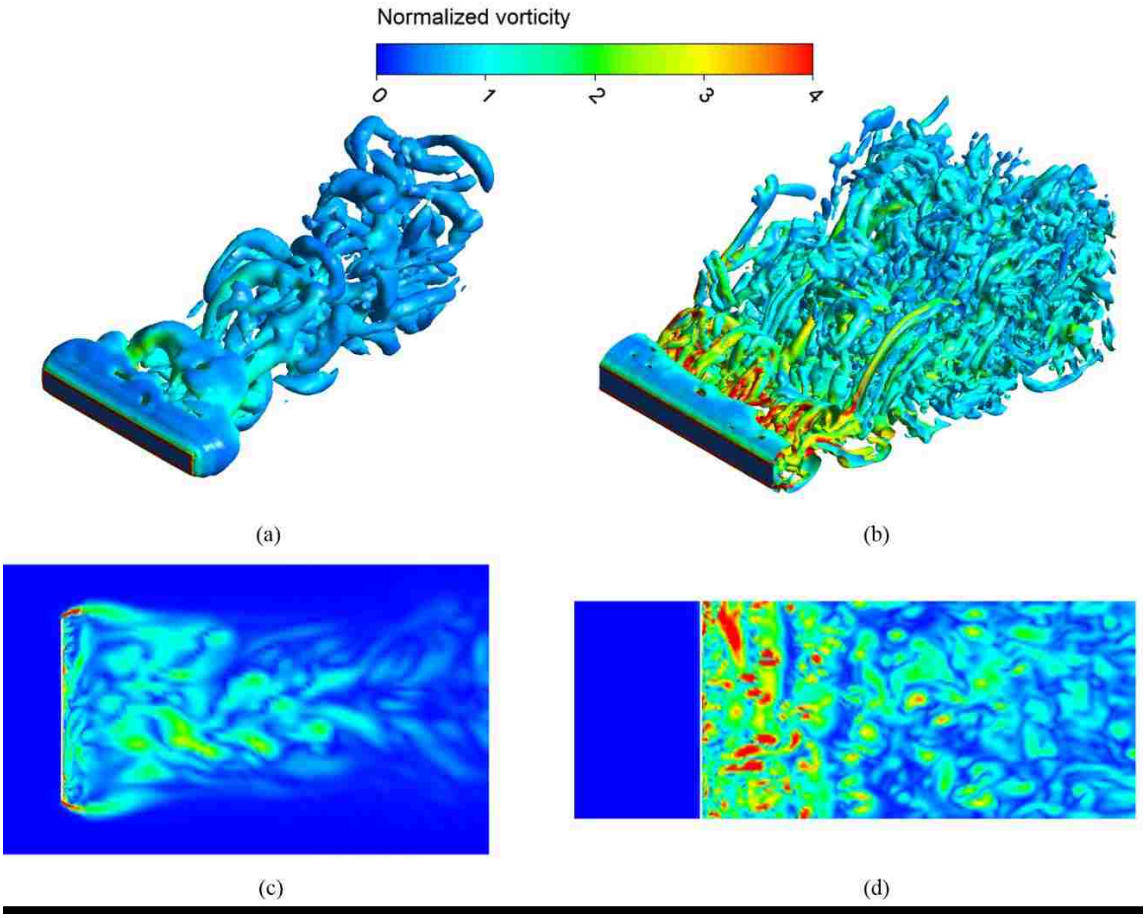

Figure 9. (a, b) Isosurfaces of Q = 0.01 and (c, d) contours of instantaneous vorticity at *y* = 0 plane. Images are acquired for (a, c) a finite plate (b, d) an infinite plate.

3.3.2 Flow Past Plates in Tandem Arrays

Cases 4-7 represent two tandem prisms in arrays with different spacings *G*/*D*. Simulations in two-dimensional and three-dimensional geometries are conducted for the same *G*/*D*, and results are shown in Figure 10. The *x*-*y* plane is used in simulations for a two-dimensional geometry. Drag coefficient predicted in three-dimensional flows differs drastically from those predicted in two-dimensional flows. Solid symbols denote drag coefficient for P1 while hollow symbols denote drag coefficient for P2. Circles designate drag coefficients predicted by two-dimensional transient LES simulations and squares designate drag coefficients predicted by three-dimensional simulations. It is documented that two-dimensional flow models over-predict drag coefficient [5, 6]. The drag coefficient of the downstream prism, P2, is lower than that of P1. Intense turbulent wake flows induced by P1 influence the drag coefficient of P2 strongly for low values of *G*/*D*. As *G*/*D* is increased, the influence of wake decreases and drag coefficient of downstream plate increases. Drag coefficients of both plates predicted by three-dimensional simulations become nearly the same for *G*/*D* of 10. On the other hand, drag coefficient predicted by two-dimensional simulations for downstream plate rebound very little even for *G*/*D* = 20, as depicted in Figure 10. It is clear that there is a flow transition occurring as *G*/*D* is varied. The critical value of *G*/*D* for the onset of flow transition is around 7. The flow transition manifests itself by rapid rebound in drag coefficient of the downstream plate P2. Obviously, two-dimensional flow modeling fails to capture such flow transitions, or it predicts the flow transition at values of *G*/*D* much greater than 20.

Characteristics of flow transition can be identified better by examining flow structures near plates.

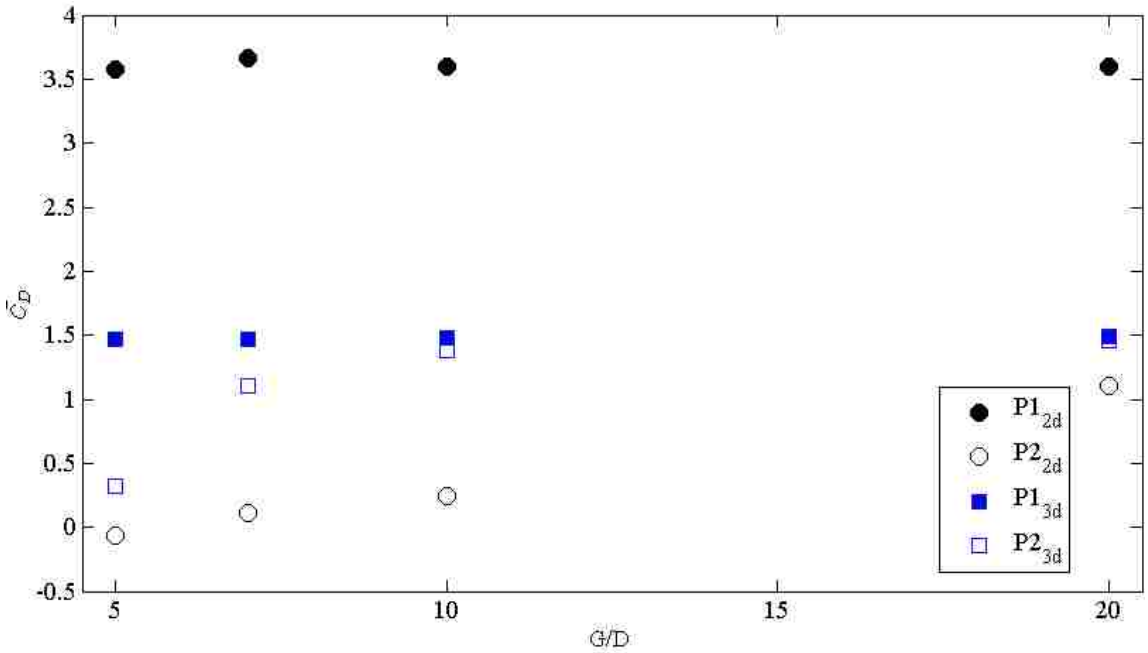

Figure 10. Mean drag coefficient of P1 and P2 predicted by two and three-dimensional flows simulations for various values of *G*/*D*.

3.3.2.1 Three-Dimensional Flow Patterns

Isosurface of vorticity, based on Q-criterion, and contours of vorticity in flows past two tandem plates with different spacings are depicted in Figure 11. Contours of magnitude of vorticity are depicted at $y = 0$ plane for $G/D = 5$, 7, 10, and 20. Streamlines originating from upstream of P1 are superimposed on images to better understand flow structures near plates. Black lines in Figure 11 denote streamlines. Streamlines originating from the mid-plane ($y = 0$) do not penetrate the wake of plates. It should be

noted that flows studied here are three-dimensional and streamlines from other planes will fill the wake region. Flow characteristics near two tandem prisms are strongly influenced by the spacing between prisms, as also reported by Sohankar [10]. When two plates are apart by 5*D*, the downstream plate, P2, is shielded by the shear layers induced by the upstream plate, P1. The intensity of vorticity field downstream and upstream of P2 is similar. Hence it is expected that the pressure difference between the upstream and downstream face of P2 is smaller. This translates to a radical drop in drag coefficient of this plate. For $G/D = 7$, shear layers formed from P1 reattach onto P2, and upstream and downstream of P2 display noticeable difference in flow patterns. As a result the drag coefficient of P2 rebounds, as illustrated in Figure 10. For $G/D = 10$, both plates start generating the Karman vortex streets individually. Vortices generated from P1 still impinge on P2 periodically, as shown in Figure 11(e) and Figure 11(f). The intensity of vortices impinging on P2 is decreased significantly for $G/D = 20$. The drag coefficient of both P1 and P2 becomes nearly the same for $G/D = 20$ (see Figure 10).

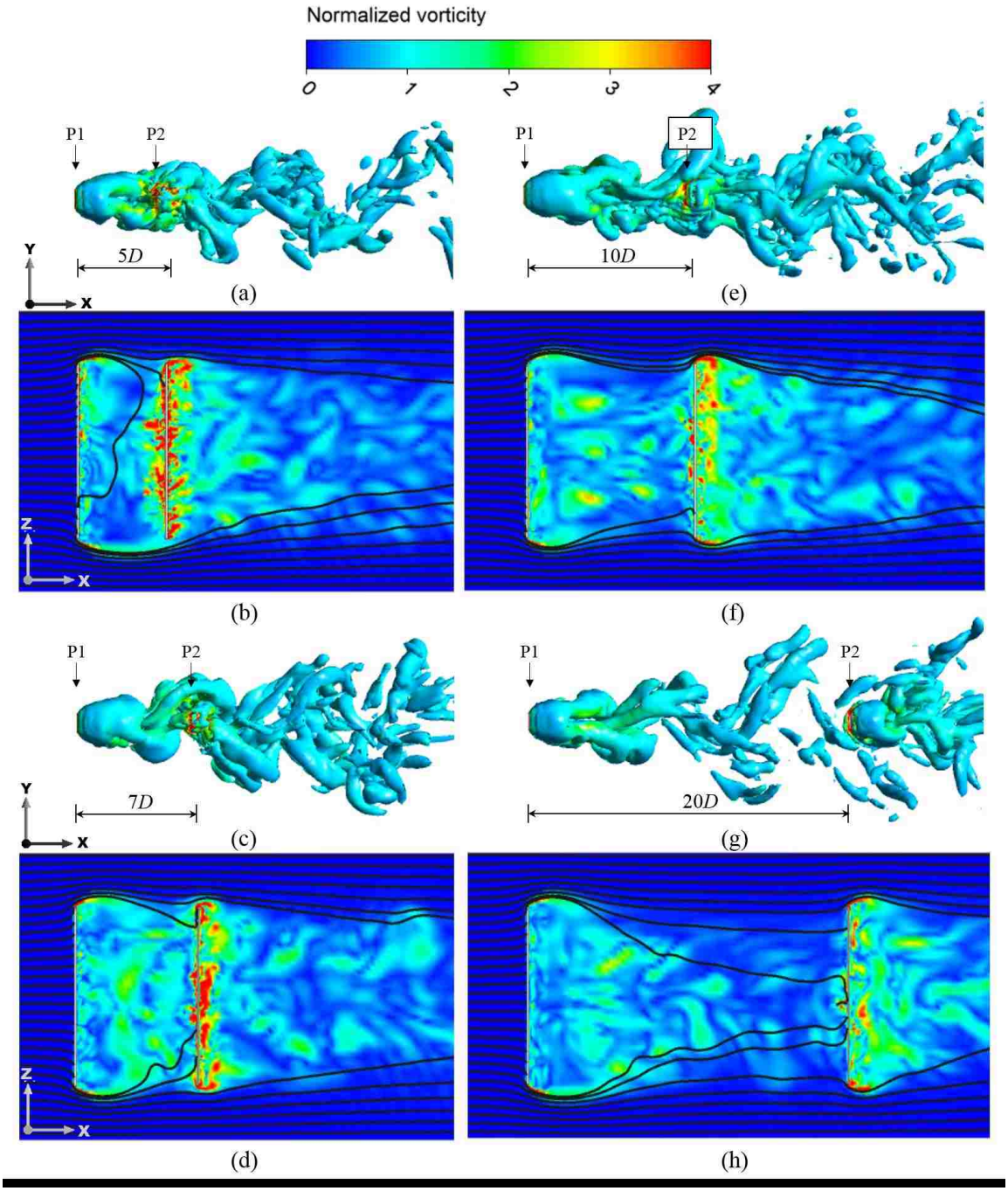

Figure 11. (a,c,e,g) Isosurface of vorticity at Q = 0.01 and (b,d,f,h) contours of instantaneous vorticity in flows past two tandem prisms for different values of *G*/*D*. Prisms are separated by 5*D* (case 4), 7*D* (case 5), 10*D* (case 6), and 20*D* (case 7), as illustrated in the figure.

3.3.3 Flow Past a Yawed Finite Plate

Flows past a single plate for different values of the yaw angle are simulated. Drag coefficients for the yaw angles of 45˚ (case 1), 60˚ (case 2), and 90˚ (case 3), are calculated to be 1.08, 1.42, and 1.50, respectively. Isosurface and contours of instantaneous vorticity for these three cases are depicted in Figure 12. Contours are acquired at the $y = 0$ plane. In cases 1 and 2, there is a stationary tip vortex attached to the leading edge of the plate, as shown in Figure 12(a, d) and Figure 12(b, e). Flow patterns in the wake become less turbulent. The absence of large and small eddies is obvious from the images. As the yaw angle is decreased, the turbulent intensity decreases and the region where turbulent eddies present shrinks. This well-documented streamlining effect will result in a decrease in the drag coefficient, as predicted in the present study.

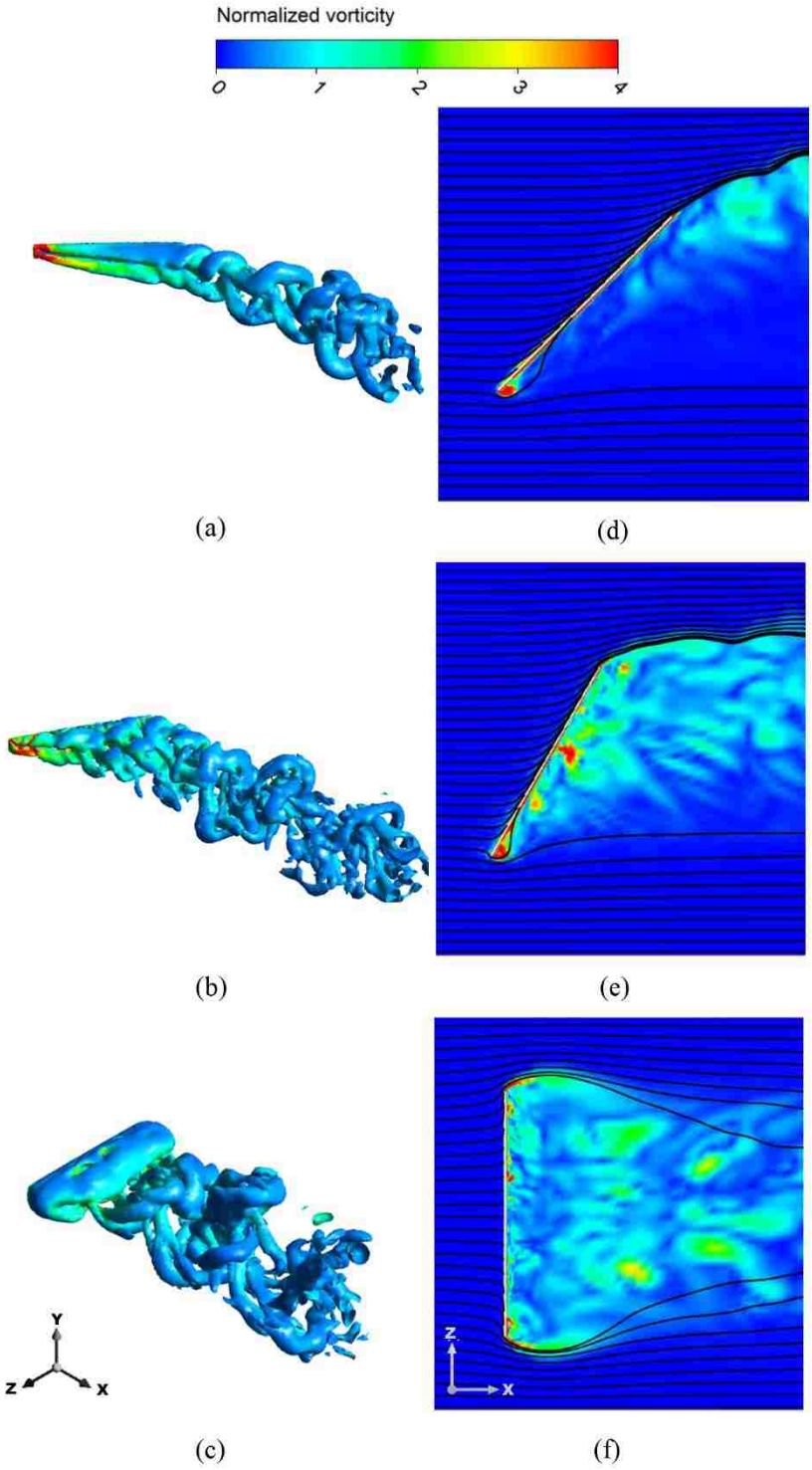

Figure 12. (a,b,c) Isosurface of vorticity at Q = 0.01 and (d,e,f) contours of instantaneous vorticity. Images are acquired for the yaw angle of (a,d) 45º (case 1), (b,e) 60º (case 2), and (c,f) 90º (case 3).

3.3.4 Flow Past Yawed Finite Plates in Staggered Arrays

Flows past two yawed prisms in a staggered array are studied for a yaw angle of 45˚ (case 8) and 60˚ (case 9). Simulations for both cases are conducted for *G*/*D* of 10. Drag coefficients of plates A1 and A2 for case 8 are calculated to be 1.06 and 1.13, respectively. For case 9, drag coefficients of plate A1 and A2 are 1.41 and 1.46. For each case, drag coefficient of the downstream plate is slightly higher than that of the upstream plate. This slight increase in drag coefficient of the downstream plate can be ascribed to the observation that the fluid accelerating past plate A1 is transported toward plate A2. Flow pattern for cases 8 and 9 are depicted in Figure 13. Stationary tip vortex is present in both plates. Vortices shed from each prism roll up toward the center, and are convected downstream, as shown in Figure 13. The region where vortices are concentrated becomes smaller as the yaw angle is decreased. It is also noticed that as the yaw angle is increased the shear layer near the centerline is formed. The wake of each plate is separated by the shear layer.

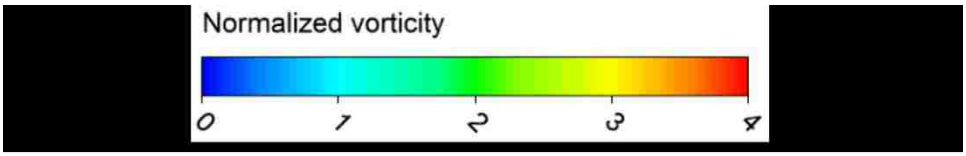

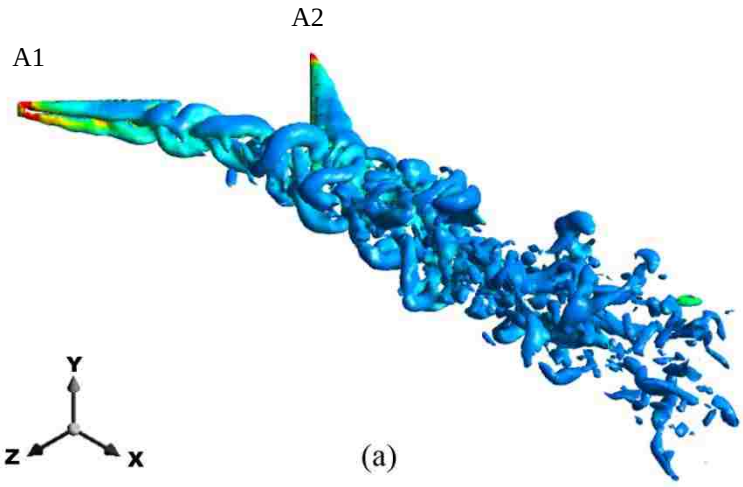

(a)

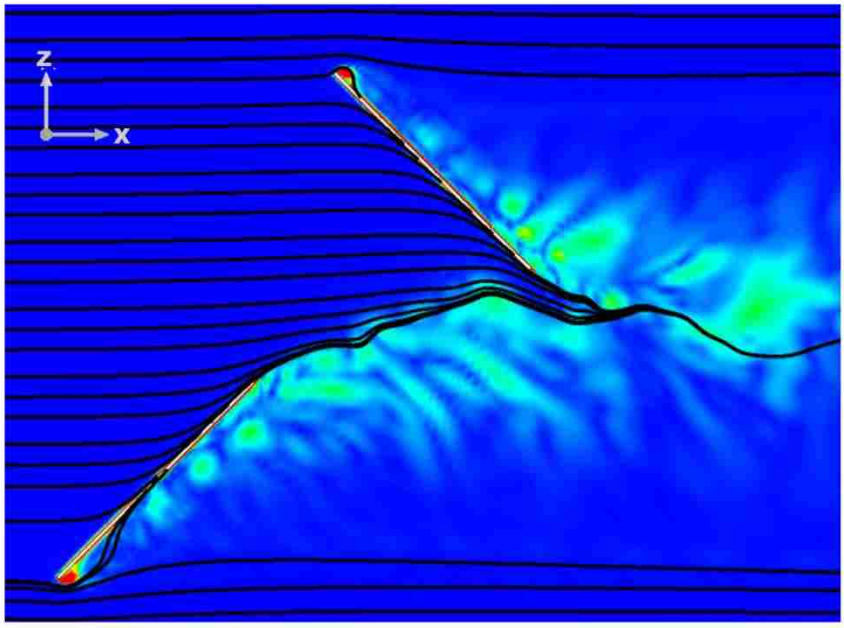

(b)

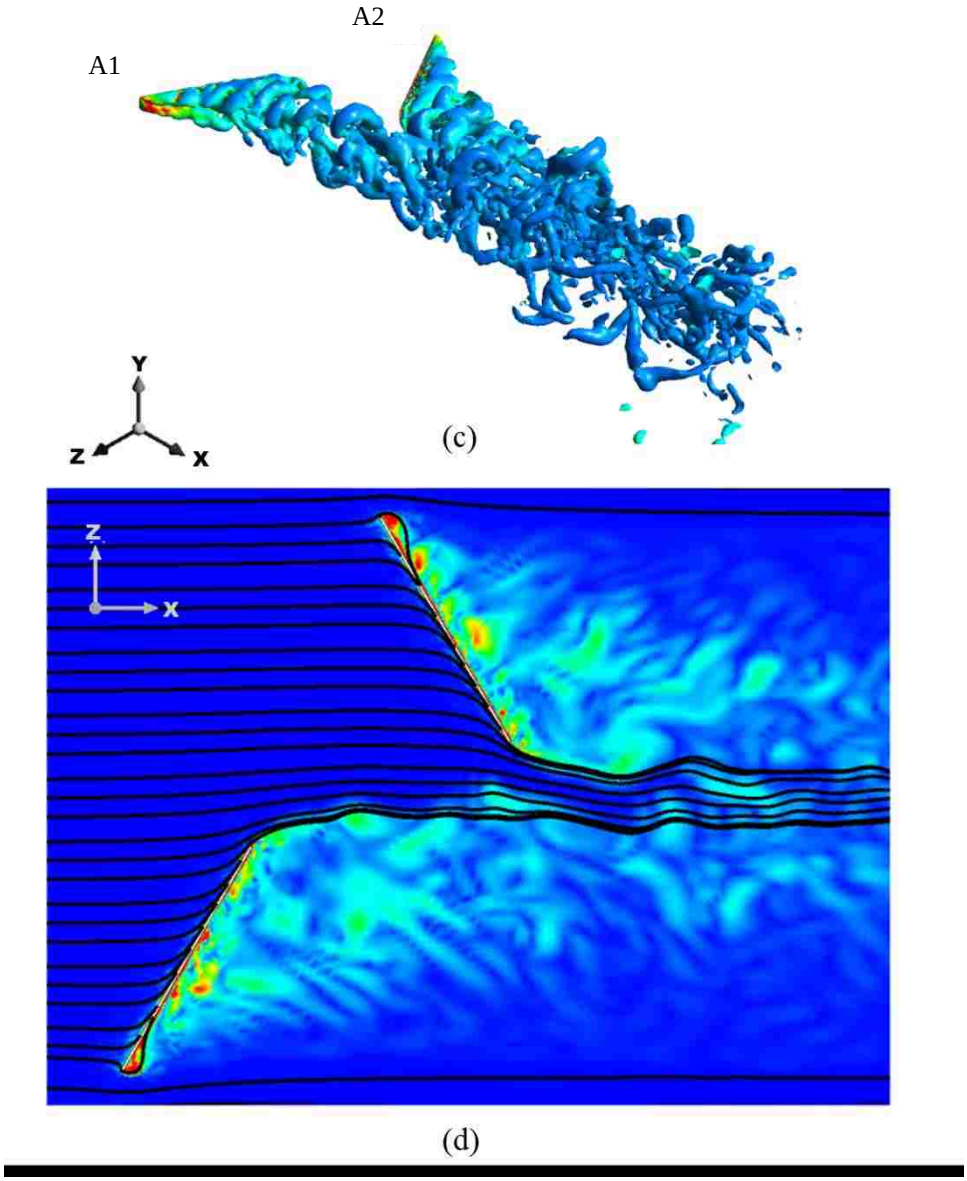

Figure 13. (a,c) Isosurface of vorticity at Q = 0.01 and (b,d) contours of instantaneous vorticity for two plates in a staggered arrangement. Plates have the yaw angle of (a,b) 45° (case 8) and (c,d) 60° (case 9).

Simulations of three-dimensional flows past four yawed prisms are conducted with the yaw angle of 45° (case 10) and 60° (case 12) in a staggered arrangement for *G*/*D* of 10. Drag coefficient of each plate in cases 10 and 12 is calculated. Drag coefficients of

A1, A2, A3, and A4 are 1.06, 1.13, 1.09, and 1.09, respectively, for case 10. Drag coefficients of plates for case 12 are 1.38, 1.46, 1.32, and 1.34, for A1, A2, A3, and A4, respectively. It is noted that drag coefficient for A2 again is slightly larger than that of the others for both cases. Drag coefficients of A3 and A4 are similar to that of A1, indicating that the turbulent wake flow patterns induced by upstream plates are hardly influencing the force exerted on these plates. Flow images depict that vorticity shed from upstream plates still impinges on part of the downstream plates, as shown in Figure 14. For yaw angle of 45° and smaller, vortices impinge on a small region near the trailing edge of upstream plates. Stationary tip vortex is attached to the leading edge of each plate in both cases, as depicted in Figure 14. As the number of plates in staggered arrays is increased the drag coefficient of downstream plates remains the same. This implies that wake flow patterns are repeated behind each plate. Drag coefficients of six yawed plates in a staggered array (case 14) are 1.06, 1.12, 1.10, 1.10, 1.12, and 1.12, for A1 through A6, respectively. Plates with spacing G/D of 10 are situated at 45° yaw angle against the oncoming flow. Flow patterns near plates for case 14 are depicted in Figure 15. Downstream plates do not experience highly turbulent wake flows as oncoming flow. That could be an important design consideration for offshore and marine structures. Highly turbulent flows impinging on structures increases the risk of failures in these systems.

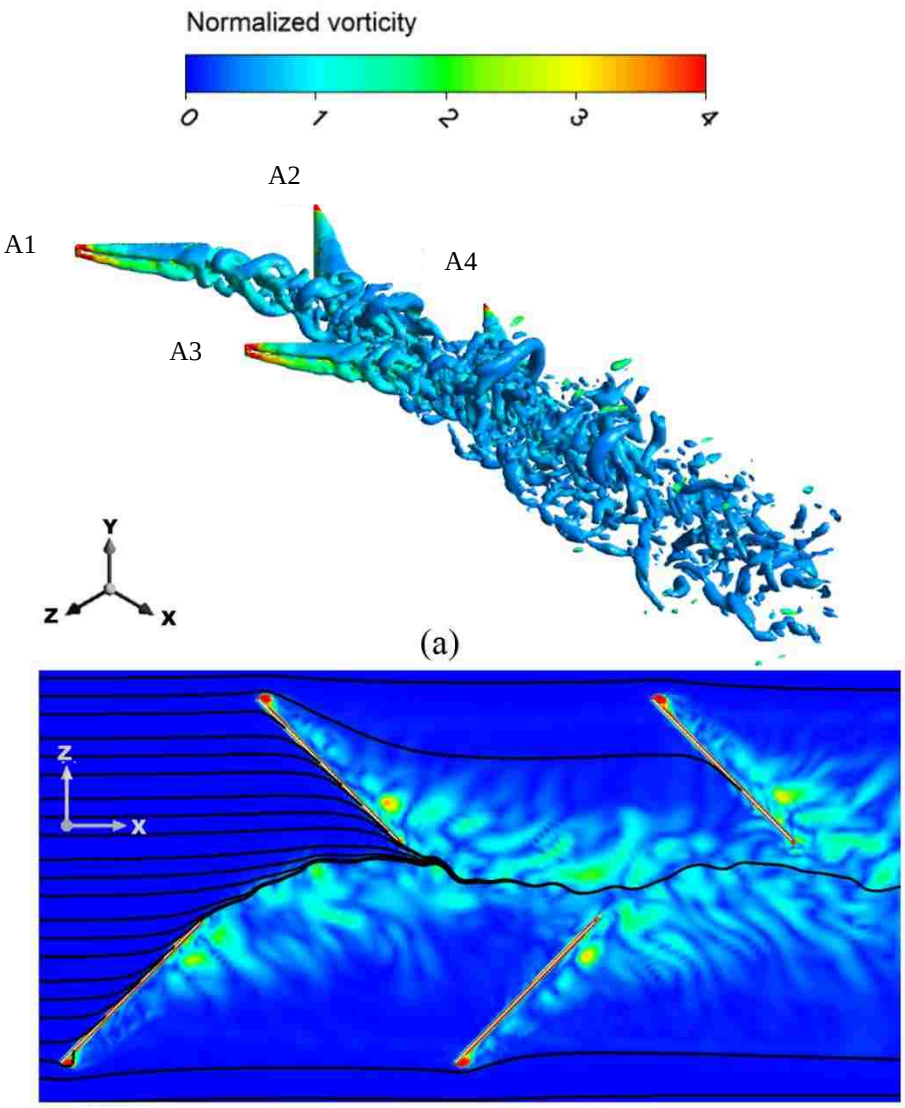

(a)

(b)

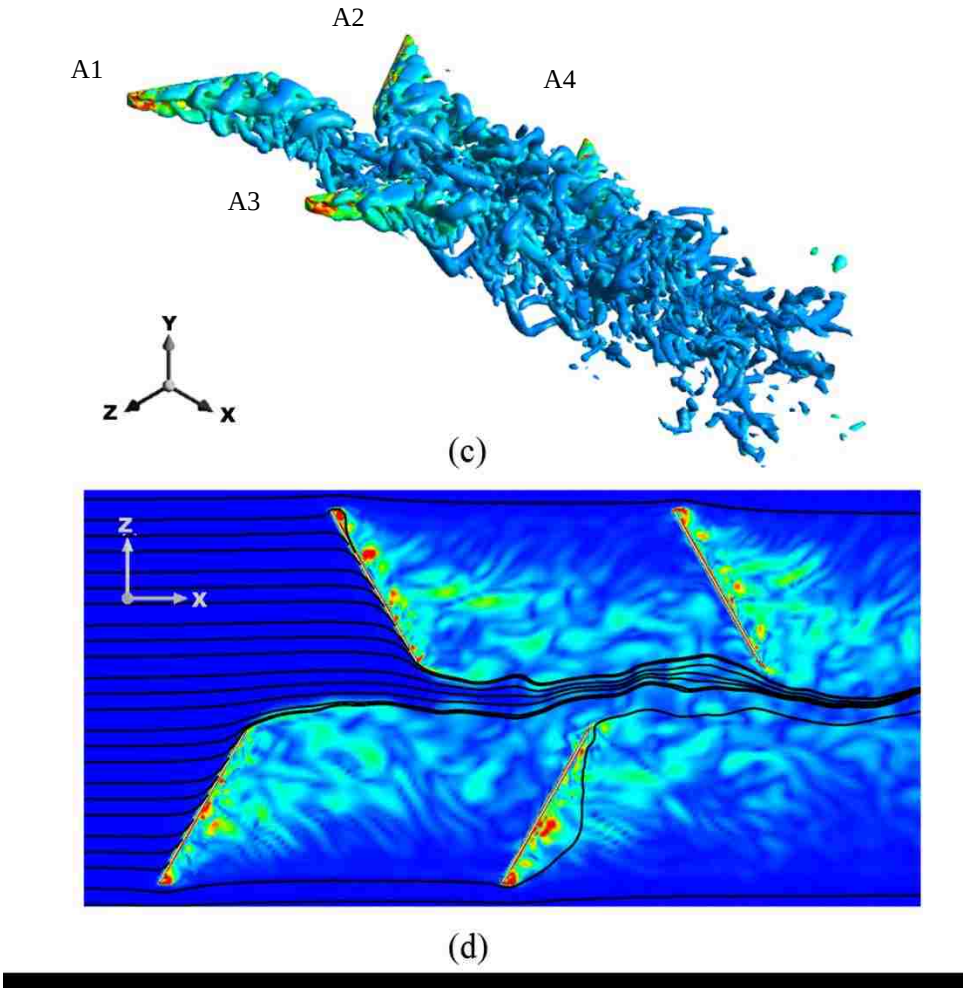

Figure 14. (a,c) Isosurfaces of vorticity at Q = 0.01 and (b,d) contours of instantaneous vorticity for four staggered plates. Images are acquired for the yaw angle of (a,b) 45˚ (case 10) and (c,d) 60˚ (case 12).

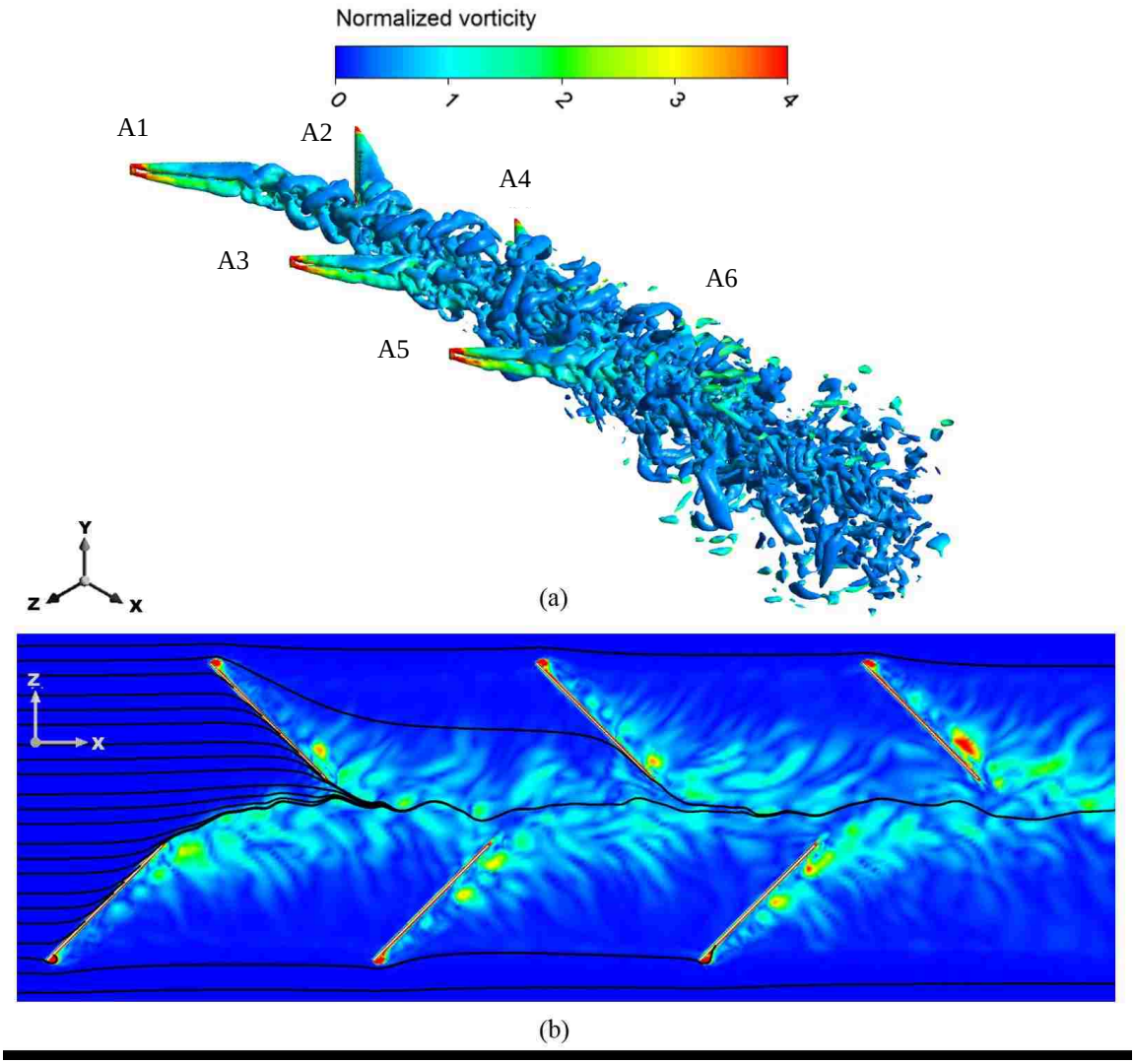

Figure 15. (a) Isosurface of vorticity at Q = 0.01 and (b) contour of instantaneous vorticity for six staggered plates with the yaw angle 45˚ (case 14).

Figure 16 illustrates flow patterns near four yawed plates with a yaw angle of 45˚ and spacing of G/D = 2.5 and 5. Even though plates are tightly spaced, drag coefficient of the downstream plate is still 66% of the drag coefficient of the upstream plate for the case of G/D = 2.5. Drag coefficients are calculated to be 1.04, 1.08, 0.66, and 0.66. It is clear that when plates are closely spaced, staggered arrays of yawed plates will perform much

better, as listed in Table 5. Drag coefficients of downstream and upstream plates in tandem and a staggered array are compared in Table 5. For staggered yawed plates drag coefficient of the downstream plate is slightly smaller for tight spacing. For perpendicular plates in a tandem arrangement with a spacing of $G/D = 5$ - not as tight as in case 11 - drag coefficient drops nearly 78% for the downstream plate, as listed in Table 5 for case 4. Tightly packed arrangement is desirable to be used in energy harvesting devices for marine current applications. Staggered arrangements of yawed plates could be an integral part of design and optimization processes in these systems.

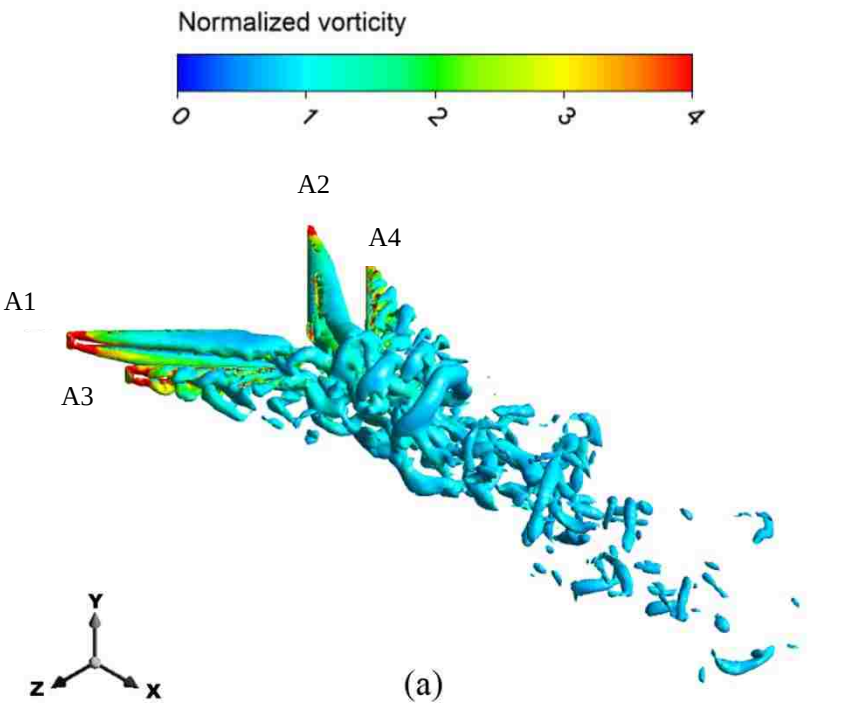

(a)

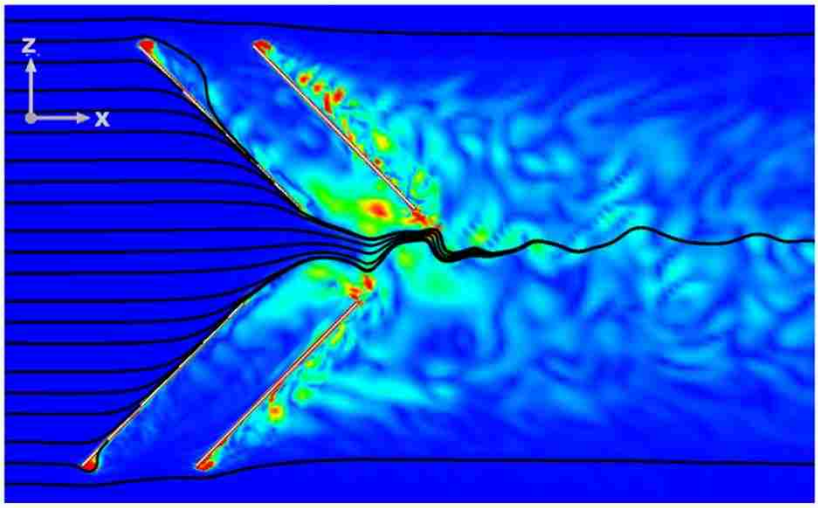

(b)

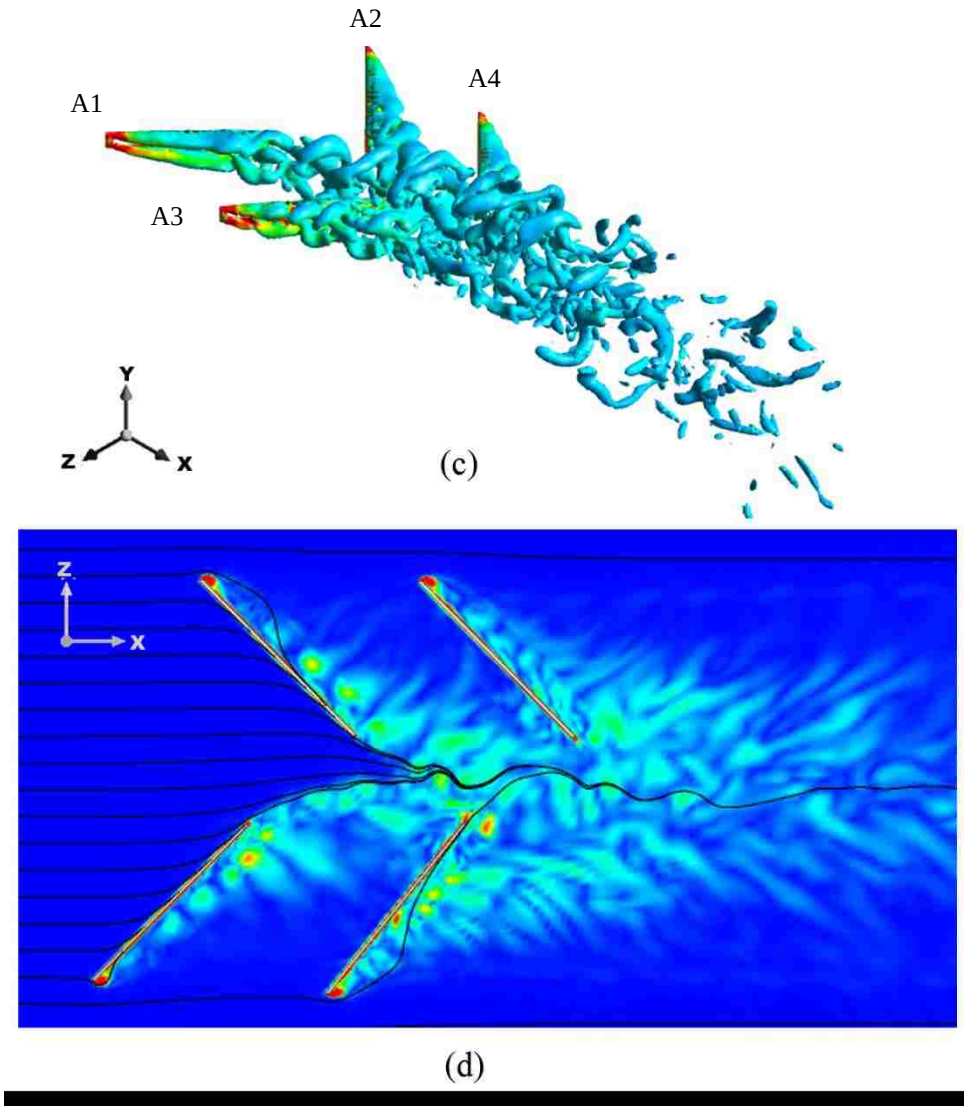

Figure 16. (a,c) Isosurfaces of vorticity at Q = 0.01 and (b,d) contours of instantaneous vorticity for four staggered plates. Plates are placed with the yaw angle of 45˚ and the spacing of (a,b) 2.5*D* (case 11) and (c,d) 5*D* (case 13).

Table 5. Average value of drag coefficient of upstream and downstream plates in a tandem arrangement of perpendicular plates and a staggered arrangement of yawed plates.

	Tandem (case 4-7)		**Staggered (case 11, 13, 10)**	
G/D	$\overline{C}_{D\_P1}$	$\overline{C}_{D\_P2}$	$\overline{C}_{D\_A2}$	$\overline{C}_{D\_A4}$
2.5	-	-	1.08	0.66
5	1.47	0.32	1.11	0.92
7	1.47	1.11	-	-
10	1.48	1.38	1.13	1.09
20	1.49	1.46	-	-

In summary, LES simulations are carried out to study three-dimensional flows past arrays of finite yawed plates at Re = 50,000 by FLUENT and OpenFOAM solver. Wake flow patterns are characterized for different values of spacing G/D and yaw angle in tandem and staggered arrays. Finite plates of L/D = 10 with two free ends are used in simulations. The average value of drag coefficient for each plate in tandem and staggered arrays are calculated. Results predicted by FLUENT and OpenFOAM solvers agrees well. Mathematical models and the numerical method employed in the current study are validated by comparing simulated results against experimental results reported by Liu and Chen [10].

As expected, drag coefficient of a finite plate situated perpendicular to the oncoming flow is lower than that of an infinitely long plate. This is attributed to the three-dimensional wake flows induced by the presence of tip vortices at the free ends of finite plates. The effect of spacing in tandem arrays predicted by three-dimensional simulations is vastly different from that predicted by two-dimensional modeling. For G/D = 5, three-dimensional flow modeling predicts that average drag coefficient of the downstream plate is about 22% of the drag coefficient of the upstream plate, while simulations in two-dimensional geometry predict average drag of the downstream plate is nearly zero. Three-dimensional flow model also predicts that drag coefficient of the downstream plate rebounds quickly as G/D is increased to 7 and recovers almost fully as G/D is increased to 10. On the other hand, drag coefficient predicted by simulations in two-dimensional geometry rebounds very slowly. Drag coefficient of downstream plate for G/D of 20 is still about 30% of the drag coefficient of upstream plate predicted by

two-dimensional modeling. Flow transitions observed in wake flows are responsible for the influence of spacing on drag coefficients. For $G/D \leq 7$, the shear layers induced by P1 wrap around or reattach to P2 and influence oncoming flows of the downstream plate. For $G/D = 10$ and higher, both upstream and downstream plates generate Karman vortex street almost independently.

Due simply to streamlining effects, the drag coefficient of yawed plates is less than that of plates oriented perpendicular to oncoming flows. Nevertheless, when yawed plates are placed in staggered arrays, the outcome could be very favorable in terms of stability and power generation for marine current energy harvesting applications. Yawed plates situated in the downstream part of the array could be outside of the turbulent wake flows induced by upstream plates. As presented by the present study, even for very tightly spaced yawed plates ($G/D = 2.5$) drag coefficient of downstream plates can still be 63% of the drag coefficient of upstream plates. Tighter spacing of plates aids in compact design of energy harvesting devices for the same power generation. This study shows that designing and optimizing offshore structures requires accurate spatial and temporal characteristics of the flows near structures. Orientation, arrangement, and spacing of these systems are critical variables in design and optimization of energy harvesting modules.

CHAPTER 4 THREE-DIMENSIONAL TRANSIENT FLOWS PAST PLATES TRANSLATING BENEATH A WALL

In this chapter, flows past yawed, finite plates placed near a translating wall are examined here in three-dimensional geometries. LES simulations are carried out to understand the effect of the moving wall on flow structures and hydrodynamic forces exerted on the prisms. A wide range of wall distance to plate height ratio, S/D, are considered. For staggered arrays of yawed plates, the effect of the spacing is also investigated. This study aids in designing the marine current energy harvesting devices consisting of translating blades near ocean platforms or river docks. This study provides the insight of the wake flow structures and hydrodynamic forces exerted on the blades in the vicinity of structures.

4.1 Computational overview

Flows past plates translating near a wall is investigated by conducting LES simulations in three-dimensional geometries. In a stationary frame, plates are translating with speed U_w in the same direction as the free stream near a stationary wall. However, relative to the reference frame attached to the translating plates, the wall is moving with the speed U_w in the direction opposite to the free stream while the plate is stationary. Reynolds number is defined by $Re = \rho U_\infty D / \mu$, where U_∞ is the speed of the free stream relative to the moving reference frame, D is the plate height, and μ is the dynamic

viscosity. The Reynolds number is fixed at 50,000 for all simulations. The schematic of the computational domain is shown in Figure 17. Figure 17(a) depicts the geometry for a single plate situated perpendicular to the free stream and Figure 17(b) illustrates the computational domain for arrays of yawed plates in a staggered arrangement. The red spot *O* denotes the origin of the coordinate system. For a single plate simulation, the origin is located at the center of the plate. Inlet is located at 12*D* upstream, outlet is located at 25*D* downstream, and the bottom surface is 8*D* away. For arrays of yawed plates, the origin is located at 18*D* from the inlet and 42*D* from the outlet and 8*D* from the bottom surfaces and at the midpoint between the side surfaces, as shown in Figure 17(b). Inlet and outlet regions are long enough that boundary conditions imposed at the inlet and the outlet have an indiscernible influence on the flow characteristics near prisms. Figure 17 (c) illustrates dimensions of a finite plate: the length, *L*, width, *w*, and height, *D*, of the plate. The length to height ratio (*L/D*) of the plate used in this study is 10. The size of the computational domain varies among cases based on the configuration and the plate gap near the wall, *S*. Dimensions of the computational domain for a single plate are 37*D* × *R* × 16*D*, while dimensions for arrays of yawed plates are 60*D* × *R* × 30*D* in the stream-wise, the cross stream, and the span-wise directions, respectively. The domain height *R* is defined as 8.5*D* + *S*. Blockage ratio is calculated based on the projection area of the plate in a stream-wise direction to the cross-sectional area of the domain around the plate. Blockage ratio varies with the wall distance. For single plate simulations, blockage ratios range from 3.9% (*S* = 7.5*D*) to 7.26% (*S* = 0.1*D*). For arrays of yawed plates, blockage ratios range from 2.9% (*S* = 7.5*D*) to 5.4% (*S* = 0.1*D*). For these low

values of blockage ratio, the influence of the bottom wall on the flow structure near prisms and on the hydrodynamic forces acting on prisms is expected to be very small.

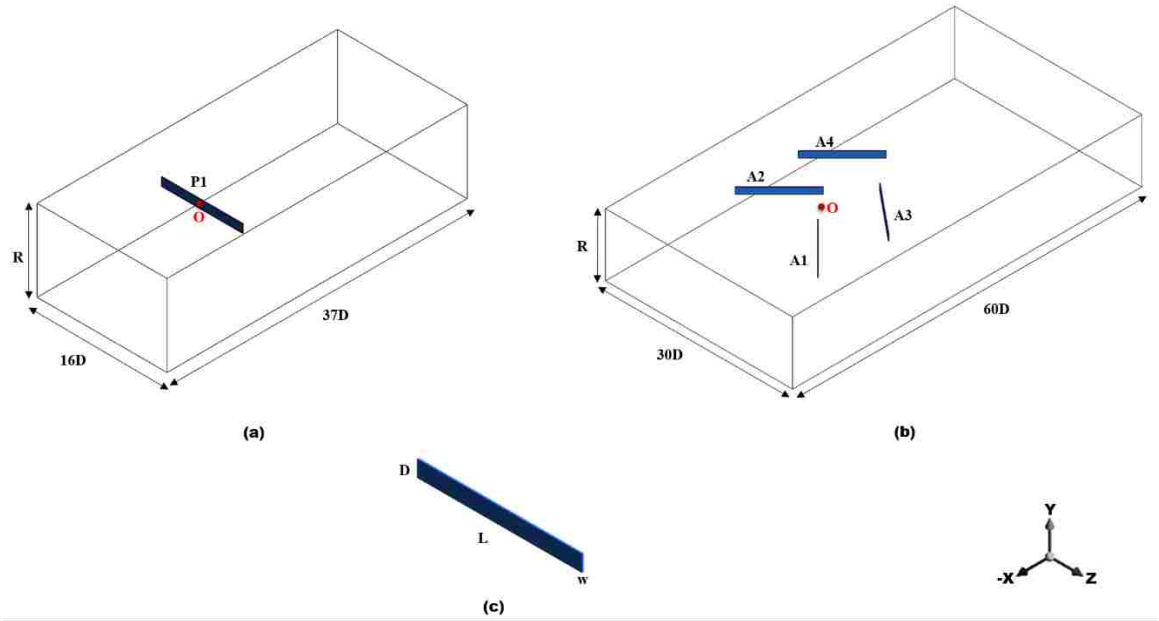

Figure 17. Schematic diagram of the three-dimensional computational domain for (a) a single plate (b) a staggered array of yawed plates. (c) Dimensions of a single plate.

The top and side view of the computational domain for a single plate geometry are shown in Figure 18(a) and Figure 18(c). Figure 18(b) and Figure 18(d) illustrate the top and the side view of the computational domain in a staggered array with a yaw angle, θ. The yaw angle in the present study is defined as the angle between the axis of the plate and the stream-wise direction. The spacing between two successive plates, G, and the yaw angle, θ, are depicted in Figure 18(b). For staggered arrays, distance from plate tip to the centerline is fixed as d. The plates in staggered arrays are labeled from upstream to downstream as A1 through A4, respectively. Here S is the distance between the tip of the

plate and the moving wall. Table 6 lists values of the geometrical and the physical properties used in the present simulations.

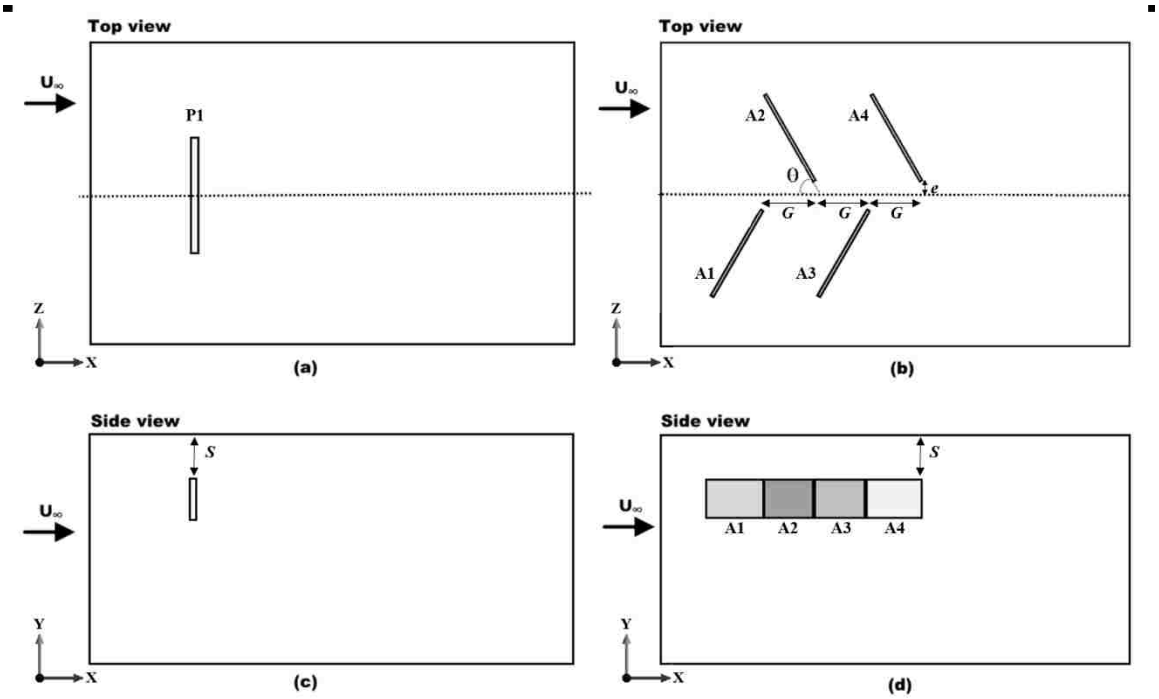

Figure 18. Schematic of flow past a single plate and yawed plates in a staggered array. (a), (b) top view of the schematic geometry and (c), (d) side view of the geometry.

Table 6. Parameters used in the present study.

Parameter	*Values*				
D	0.1	[m]	U_∞	0.5	[m s^{-1}]
e	0.2	[m]	U_w	0.25	[m s^{-1}]
G/D	2.5, 5	[-]	w	0.01	[m]
L	1	[m]	ρ	1000	[kg m^{-3}]
Re	50,000	[-]	μ	0.001	[kg m^{-1} s^{-1}]
S/D	0.1 - 7.5	[-]	θ	45	[degree]

Structure mesh is used in the discretization of the computational domain. The mesh is finer near the plate in order to better capture shear layer separations and the wake flow structures. Figure 19 shows examples of the mesh around the plates at $Y = 0$ plane. Cutcell assembly meshing method is used for all simulations. The minimum mesh edge length near the plate is 0.01D, the maximum mesh edge length at far wake region in the computational domain is 0.16D. The face sizing on the plate is 0.02D. The mesh growth rate is selected to be 1.2.

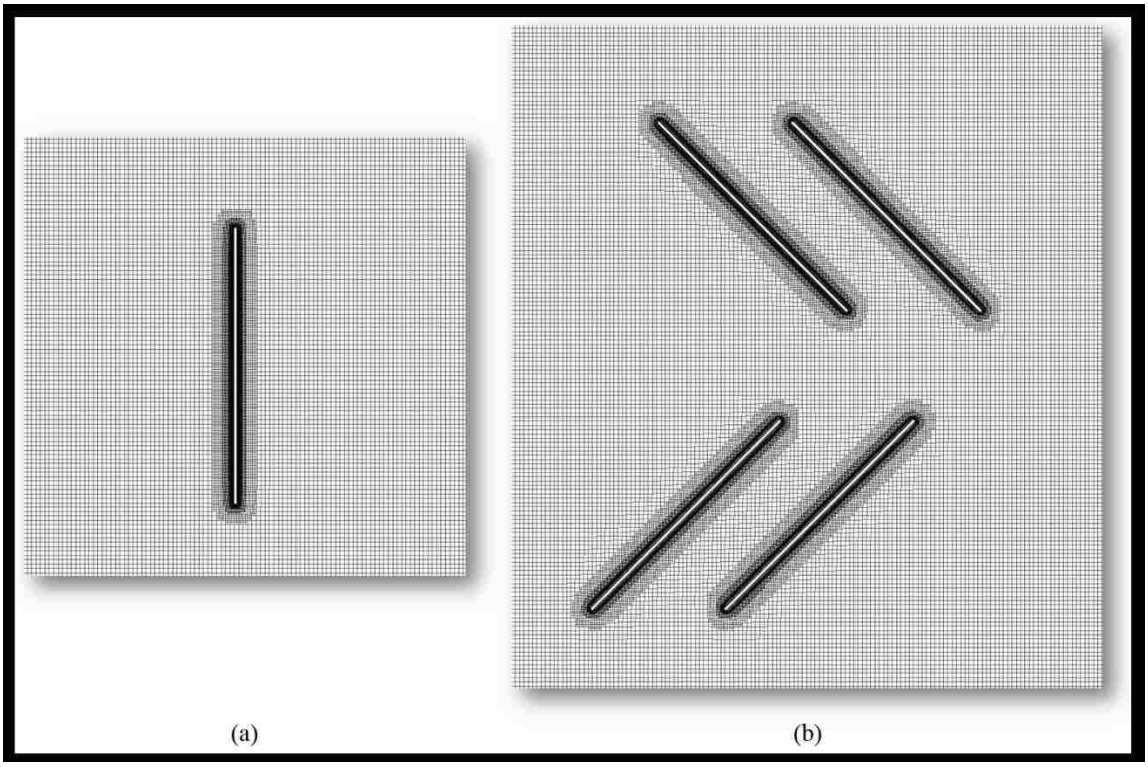

Figure 19. Examples of the structure mesh around (a) a single plate (b) a staggered array of yawed plates for $G/D = 2.5$ at the $Y = 0$ plane.

The mesh size varies with the arrangement and wall distance. For a single plate at S/D of 0.1, 0.25, and 0.5, 6.03 million, 6.4 million, and 7.6 million mesh elements are

used, respectively. In these geometries finer mesh elements are employed in the region within 6.8D upstream and downstream of the plate, and in the region near the top wall. For $S/D \geq 0.75$, mesh size ranges from 2.2 million to 3.2 million. Since the boundary layer influence is weaker in these geometries, mesh refinement is applied only in regions near the plate. The mesh size for the staggered array of yawed plates for S/D = 1.5 and G/D = 2.5 and 5 is around 7.7 million. The averaged value of y^+ calculated for a single plate is less than 11.1. The averaged value of y^+ calculated for arrays of yawed plates is less than 14.32. The y^+ value indicates that the grid size is adequate to predict shear layer separation. The non-dimensional wall distance is defined as $y^+ = u_* y/\nu$, where y is the distance to the nearest wall and u_* is the friction velocity at the nearest wall. The Courant-Freidrichs-Lewy (CFL) condition states the stability of simulation. For a stable, unsteady solution the fluid should move less than one grid spacing at each time step. The Courant number ($u\Delta t/\Delta x$) is a non-dimensional parameter that shows whether the solution satisfies the CFL condition. The maximum Courant number calculated for a single plate at all values of wall distance is less than 2.28, while for arrays of yawed plates it is less than 1.55. The maximum Courant number only happens at few cells in the computational domain. The average value of y^+ and the maximum Courant number of each case are recorded in Table 7.

Table 7. Averaged y^+ value of the plate and the maximum Courant number for each simulation

Single plate	**Depth ratio *S/D***							
P1	**0.1**	**0.25**	**0.5**	**0.75**	**1.5**	**2.5**	**4**	**7.5**
y+	11.1	8.08	5.46	7.82	8.39	8.04	7.83	7.72
C_{max}	1.59	1.92	2.26	0.74	1.20	0.79	0.75	0.68
4 plates	***S/D* = 1.5 *G/D* = 2.5**				***S/D* = 1.5 *G/D* = 5**			
	A1	A2	A3	A4	A1	A2	A3	A4
y+	13.81	14.32	12.88	13.12	14.17	14.09	13.80	13.79
C_{max}	1.35				1.55			

Simulations using higher mesh density are conducted for three cases in order to perform a mesh convergence study: a single plate at *S*/*D* = 7.5 and staggered arrays of yawed plates at *S*/*D* = 1.5 and *G*/*D* = 2.5 and 5. The increase in mesh density is mostly due to the finer mesh employed near the plates. For a single plate case, simulations are conducted with a mesh size of 3.2 million and 5.9 million elements. With 5.9 million mesh elements, the minimum mesh edge length is decreased to 0.002*D* and the face sizing is decreased to 0.015*D*. For the staggered array of yawed plates, simulations with mesh size of 7.7, 7.5 million elements and 9.7, 9.6 million elements are compared, respectively, for a spacing of 2.5 and 5. With mesh density of 9.7 and 9.6 million elements, the minimum mesh edge length is decreased to 0.003*D* and the mesh growth rate is decreased to 1.1. The y^+ values and time-averaged values of drag coefficient, $\overline{C_D}$, for each plate calculated at both regular and finer meshes are listed in Table 8. Drag coefficient is defined as $C_D = F_D/\left(\frac{1}{2}\rho U_\infty^2 A\right)$, where F_D is the drag force acting on the plate and *A* is the projection area of the plate against the flow. The non-dimensional time step is defined as $\Delta\lambda = \Delta t U_\infty/D$. $\Delta\lambda = 0.004$ is used in all simulations. The time averaged

drag coefficients predicted using the regular mesh and the finer mesh in both a single plate and staggered array of yawed plates are similar. The y^+ values obtained for finer mesh are three to four times lower than those for regular mesh. It is demonstrated here that the regular mesh is sufficient to characterize hydrodynamic loadings on prisms. Results presented in this paper are obtained using regular mesh. It is important to note that the accuracy of results presented here can be improved by refining the mesh further in the vicinity of prisms. Limitations in the computational resources make that task challenging.

Table 8. Mean drag coefficient value and *y*+ values of P1 and A1 to A4.

Case	**Mesh Size**	**P1/A1**		**A2**		**A3**		**A4**	
		$\overline{C}_D$	y^+	$\overline{C}_D$	y^+	$\overline{C}_D$	y^+	$\overline{C}_D$	y^+
1 plate	3.2m	1.50	7.72	-	-	-	-	-	-
***S*/*D* = 7.5**	5.9m	1.51	1.81	-	-	-	-	-	-
4 plate	7.7m	1.16	13.81	1.25	14.32	0.67	12.88	0.67	13.12
***S*/*D* = 1.5**	9.7m	1.16	4.12	1.22	4.21	0.70	3.86	0.75	3.90
***G*/*D* = 2.5**									
4 plate	7.5m	1.20	14.17	1.29	14.09	1.38	13.80	1.07	13.79
***S*/*D* = 1.5**	9.6m	1.19	4.14	1.30	4.26	1.38	4.09	1.06	4.13
***G*/*D* = 5**									

Boundary conditions imposed are as follows. Mass flow rate is specified at the inlet while zero gauge pressure is applied at the outlet. No-slip boundary conditions are applied along surfaces of plates. The top and the bottom surfaces are no-slip walls translating with a constant speed of 0.25 m/s in the direction opposite to the free stream. Periodic boundary conditions are invoked on the side surfaces of the computational domain.

The semi-implicit method for pressure-linked equations (SIMPLE) solution algorithm is employed to resolve fully coupled velocity and pressure field. Discretization is performed by using the bounded central differencing and bounded second order implicit scheme. Simulations are performed by using ANSYS 14.5 Fluent commercial software. Details of numerical schemes and descriptions of simulation tools can be found in ANSYS theory guide and ANSYS user guide [57, 58].

4.2 Results and discussions

Results are presented for flows past arrays of finite plates placed near a moving wall. Flow patterns near plates and the hydrodynamic forces exerted on the plates are acquired for the scaled time, $\lambda = tU_\infty/D$, up to 250. Flow images are presented at λ= 250.

4.2.1 Flows Past a Single Plate Near a Wall

Isosurfaces of Q-criterion (Q = 0.01) near a finite plate placed at various values of wall gap are depicted in Figure 20. Isosurfaces of Q-criterion is colored with the normalized vorticity magnitude, $\omega D/U_\infty$. When the plate is placed far away from the wall, S/D = 7.5, the vortex shedding is regular. There are well-organized large eddies induced by vortex shedding present in the wake of the plate. These eddies extend far downstream of the plate with little dissipation, as seen in Figure 20(a). As the wall distance is decreased, the wall influence on the vorticity field in the far wake region becomes visible. Wall effects become stronger and flow structures in the near wake region are influenced

as the plate is placed closer to the wall, as shown in Figure 20. The wake gradually becomes asymmetric, and large eddies break into smaller eddies. Coherent flow structures in the wake disappear, and they become spatially irregular and less organized. When the wall gap ratio is even smaller, $S/D < 0.5$, eddies generated inside the boundary layer of the wall and the wake of the plate interact strongly. Intense vortical activities are observed in the region between the plate and the wall. Smaller scale eddies occupy the gap between the wall and the plate. As the plate is placed closer to the wall, small eddies are generated upstream of the plate, as seen in Figure 20(f)-(h).

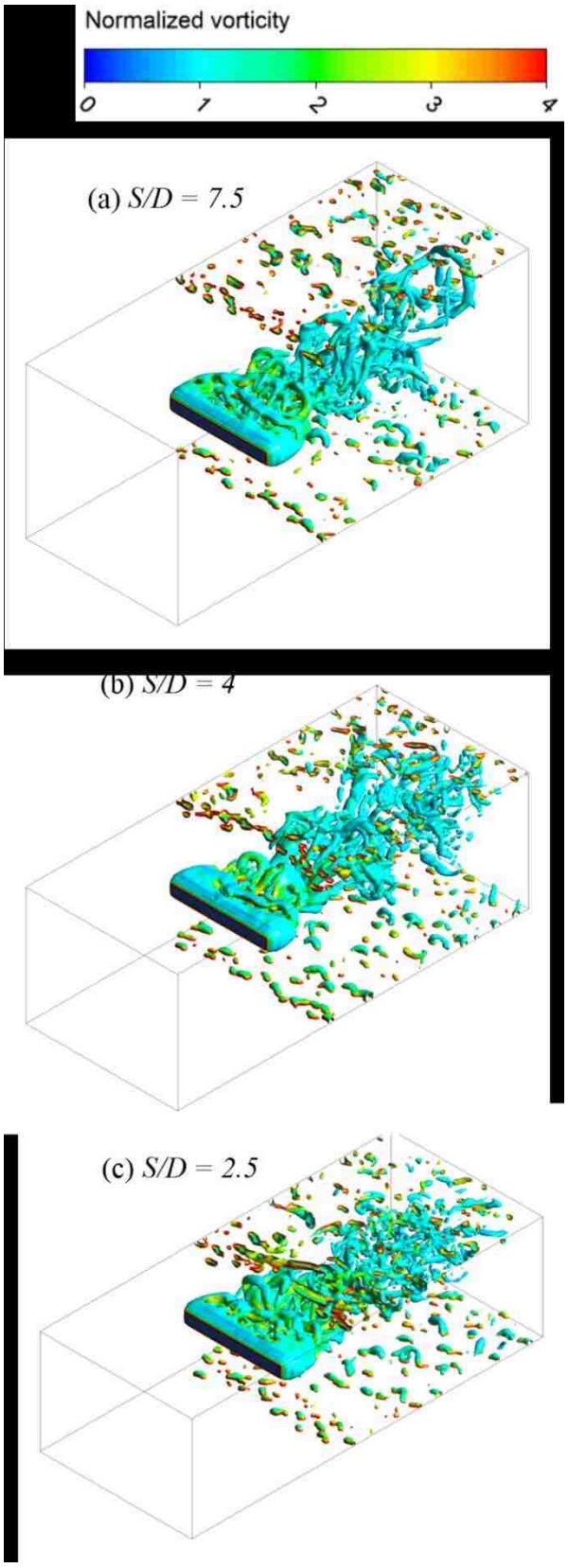
Normalized vorticity
0
1
2
3
4
(a) S/D = 7.5
(b) S/D = 4
(c) S/D = 2.5

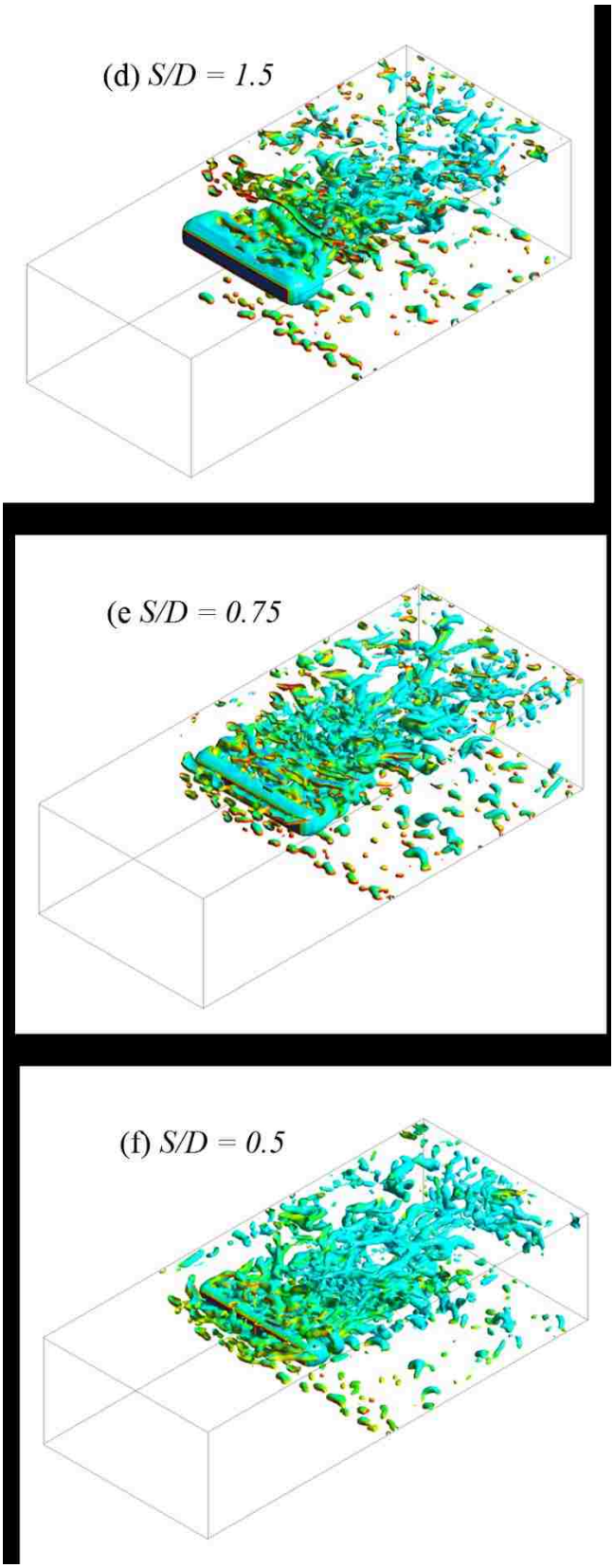
(d) S/D = 1.5
(e S/D = 0.75
(f) S/D = 0.5

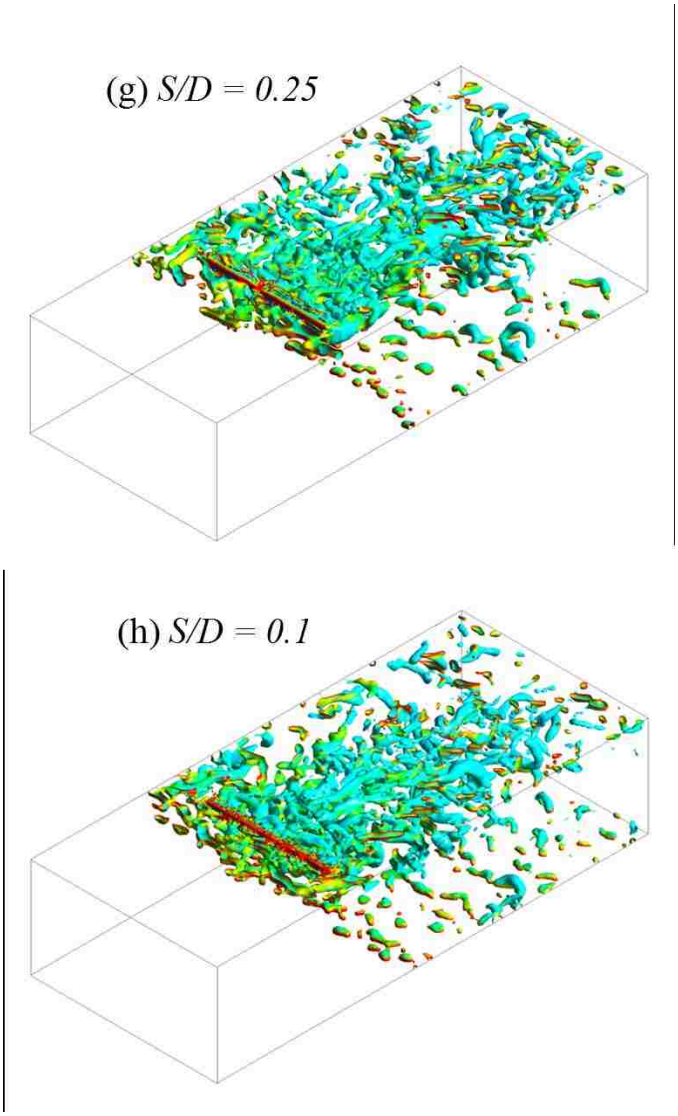

Figure 20. Isosurfaces of Q = 0.01 with the normalized vorticity magnitude at λ = 250 for various values of *S*/*D* = (a) 7.5 (b) 4 (c) 2.5 (d) 1.5 (e) 0.75 (f) 0.5 (g) 0.25 (h) 0.1.

Figure 21 depicts iso-surfaces of Q-criterion at the Z = 0 plane and profiles of the stream-wise component of the velocity at various locations upstream of the plate for *S*/*D* = 0.1, 0.25, and 0.5. Vortex structures displayed in Figure 21(a) and (b), when the plate is closer to the wall, clearly indicate there is a strong interaction between the vortices generated from the top of the plate and the vortices of the wall boundary layer. The

strong influence of the wall is also visible by the presence of small eddies in the region near the front face of the plate when the plate is situated close to the wall, see Figure 21(a) and (b). Time-averaged stream-wise component of velocity profiles are plotted at 1*D*, 3*D*, 5*D*, and 6*D* upstream of the plate. The locations where profiles are calculated are shown in dashed lines in Figure 21(c). The boundary layer thickness predicted by simulations at 6*D* are 0.266*D*, 0.191*D*, and 0.178*D*, respectively for *S*/*D* = 0.1, 0.25, and 0.5. The boundary layer thickness estimated by the Prandtl power law at 6*D* upstream of the plate is 0.164*D*. It is noted that at *S*/*D* = 0.1 and 0.25 the interaction of the flow near the plate and the boundary layer is so strong, the boundary layer velocity profiles as far as 6*D* upstream of the plate are altered. As the plate is placed further away from the wall the classical boundary layer flow near the top wall is recovered. Prandtl power law model is $\delta_x = \frac{0.37x}{Re_x^{0.2}}$, where $Re_x = \frac{\rho\left(U_\infty + U_w\right)x}{\mu}$ is the Reynolds number based on the upstream distance. Turbulent boundary layer thickness of the wall, δ_x, calculated at x=12*D* for the single plate geometry is 0.286*D*. For *S*/*D* = 0.1 and 0.25, the fact that the plate is placed inside the boundary layer can help explaining the strong interaction between the boundary layer and the wake flow.

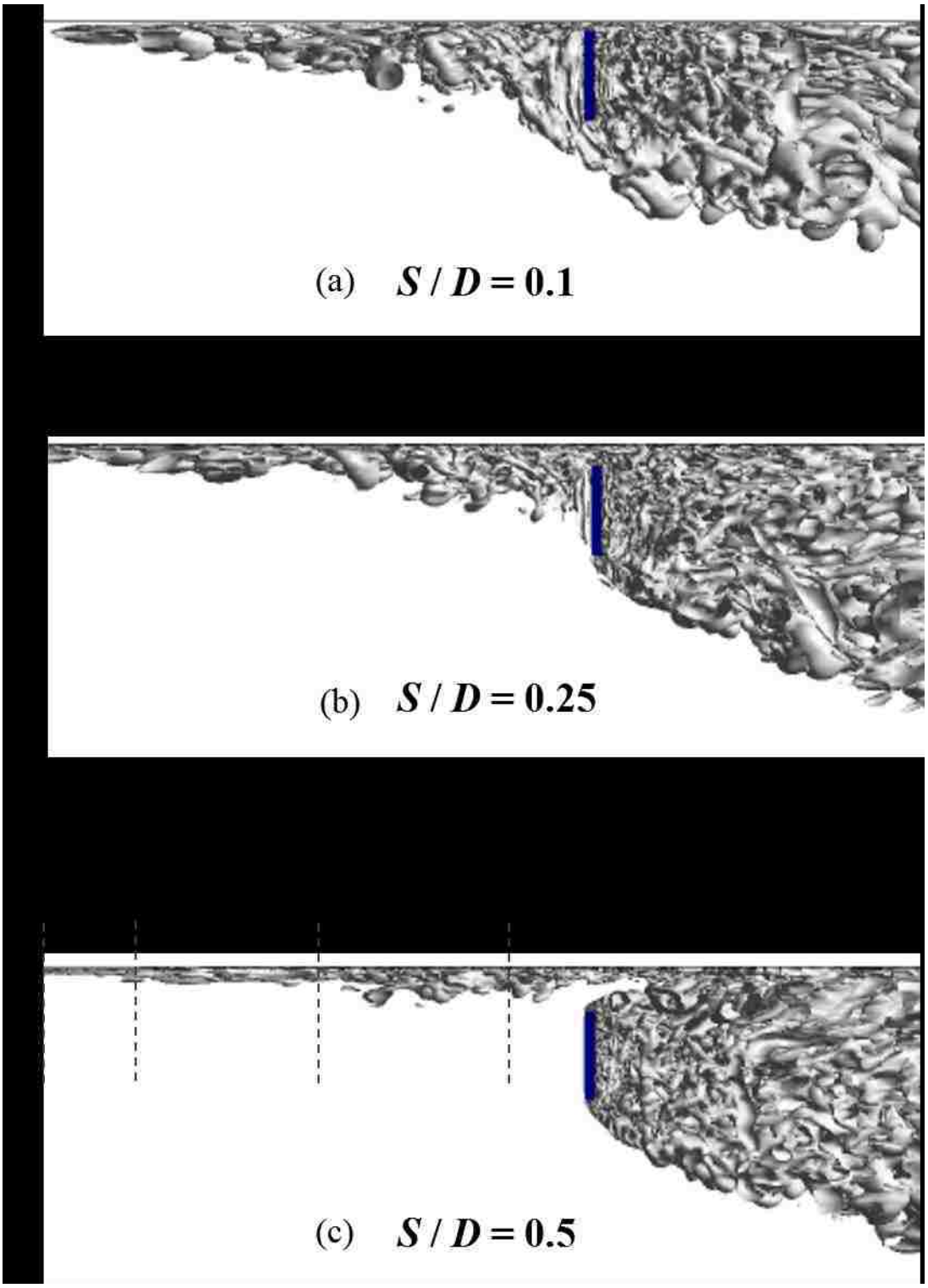
(a) S / D = 0.1
(b) S / D = 0.25
(c) S / D = 0.5

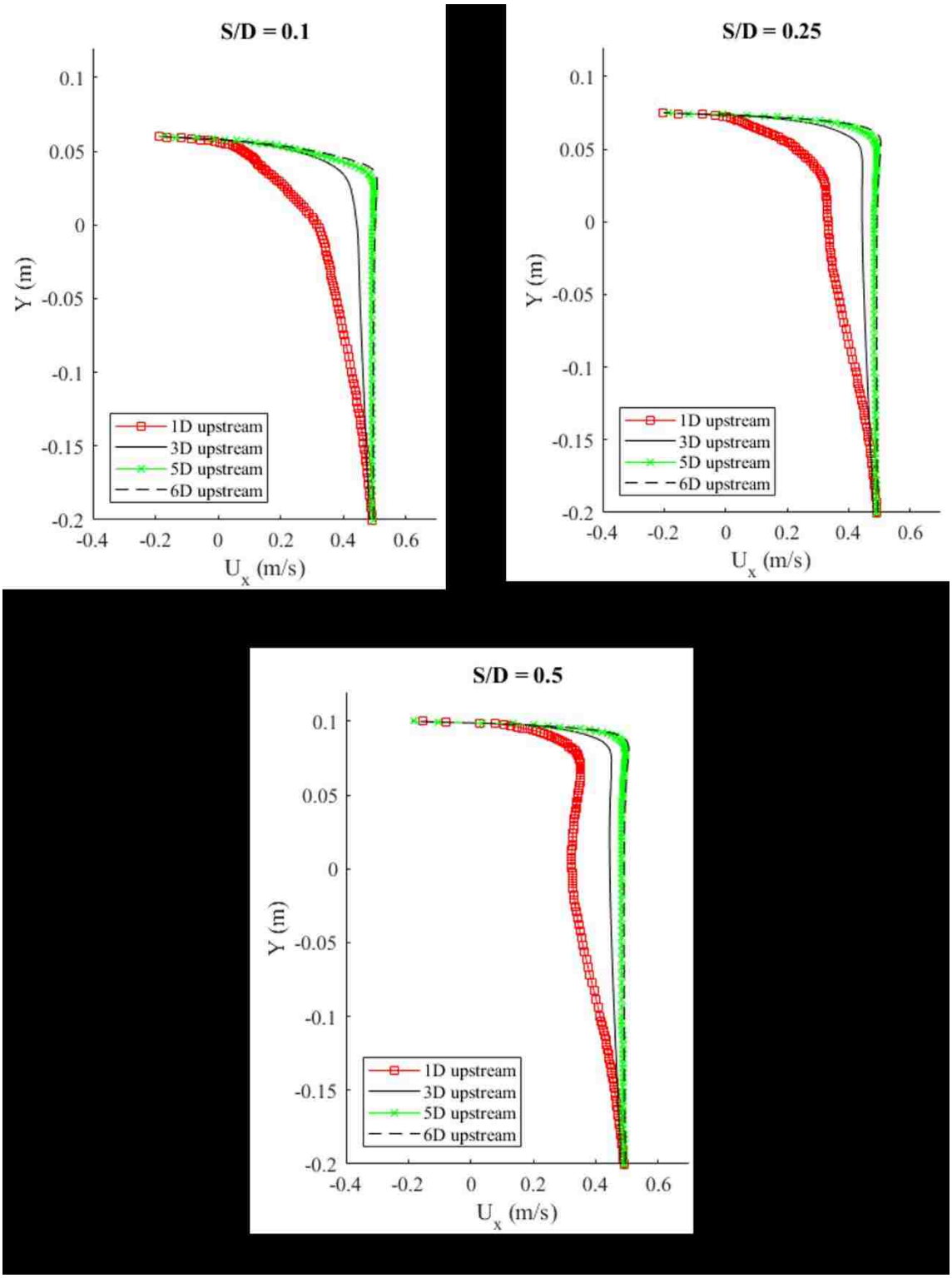

Figure 21. Iso-surfaces of Q = 0.01 at Z = 0 plane and time-averaged stream-wise component of velocity profiles for S/D = (a)(d) 0.1, (b)(c) 0.25, and (c)(f) 0.5.

A more detailed description of the flow field is depicted in Figure 22. Instantaneous contours of the span-wise component of the normalized vorticity are plotted for a range of S/D from 7.5 to 0.1. When $S/D \geq 4$ the wake flow is completely detached from the wall boundary layer. Flow patterns in the near and the far wake region are dominated by the alternating vortex shedding from the plate. As S/D is reduced to 2.5 and 1.5, the wake flow is still dominated by the vortex shedding from the plate, but the flow structure in the far downstream is altered by the presence of the wall. As S/D is decreased further to 0.75 and 0.5, the vortex shedding patterns at the top and the bottom of the plate differ significantly and the wake flow becomes asymmetric, as seen in Figure 22(e) and Figure 22(f). Vortices shedding from the side closer to the wall are fully suppressed as the plate is placed closer to the wall. Significant vortical activities are seen upstream of the plate, especially for cases that have wall gaps smaller than the turbulent boundary layer thickness of the top wall ($0.286D$), see Figure 22(g)- Figure 22(h). The boundary layer thickness here is calculated based on upstream length $x = 12D$. Vortices shedding from the top of the plate are disrupted due to the boundary layer effect. Since the wall is moving relative to plate in the direction opposite of the free-stream flow, it is creating a wake-like flow in front of the plate. This effect is strong enough to influence the flow field when the plate is placed very close to the wall. Large-scale vortices initiated from the surface closer to the wall remain near the wall and extends further downstream of the plate for $S/D = 0.1$. These alterations in the flow structures near a plate could have profound effects on hydrodynamic forces acting on the plate. That will in turn influence the performance of energy harvesting device for marine current applications.

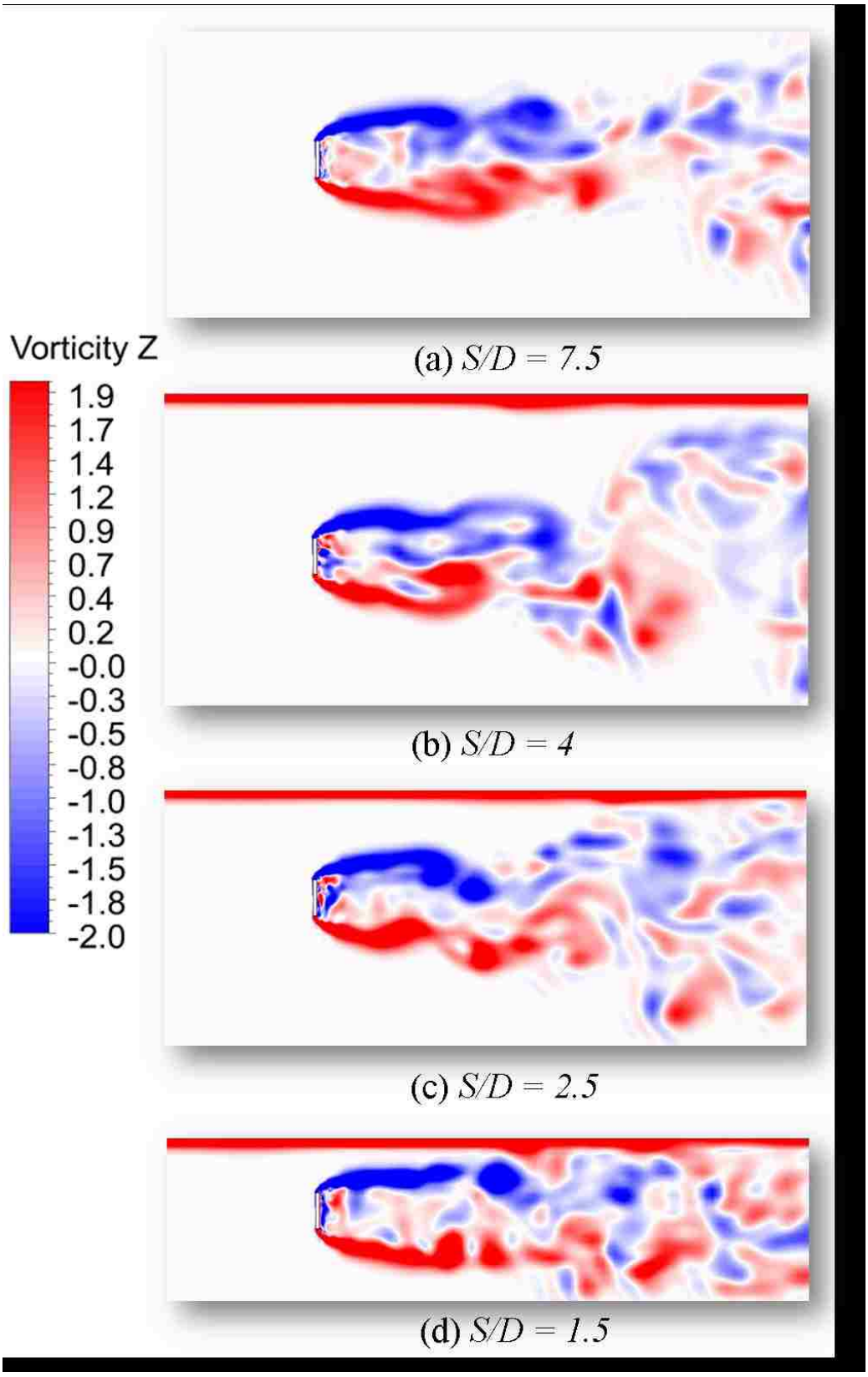
Vorticity Z
1.9
1.7
1.4
1.2
0.9
0.7
0.4
0.2
-0.0
-0.3
-0.5
-0.8
-1.0
-1.3
-1.5
-1.8
-2.0
(a) S/D = 7.5
(b) S/D = 4
(c) S/D = 2.5
(d) S/D = 1.5

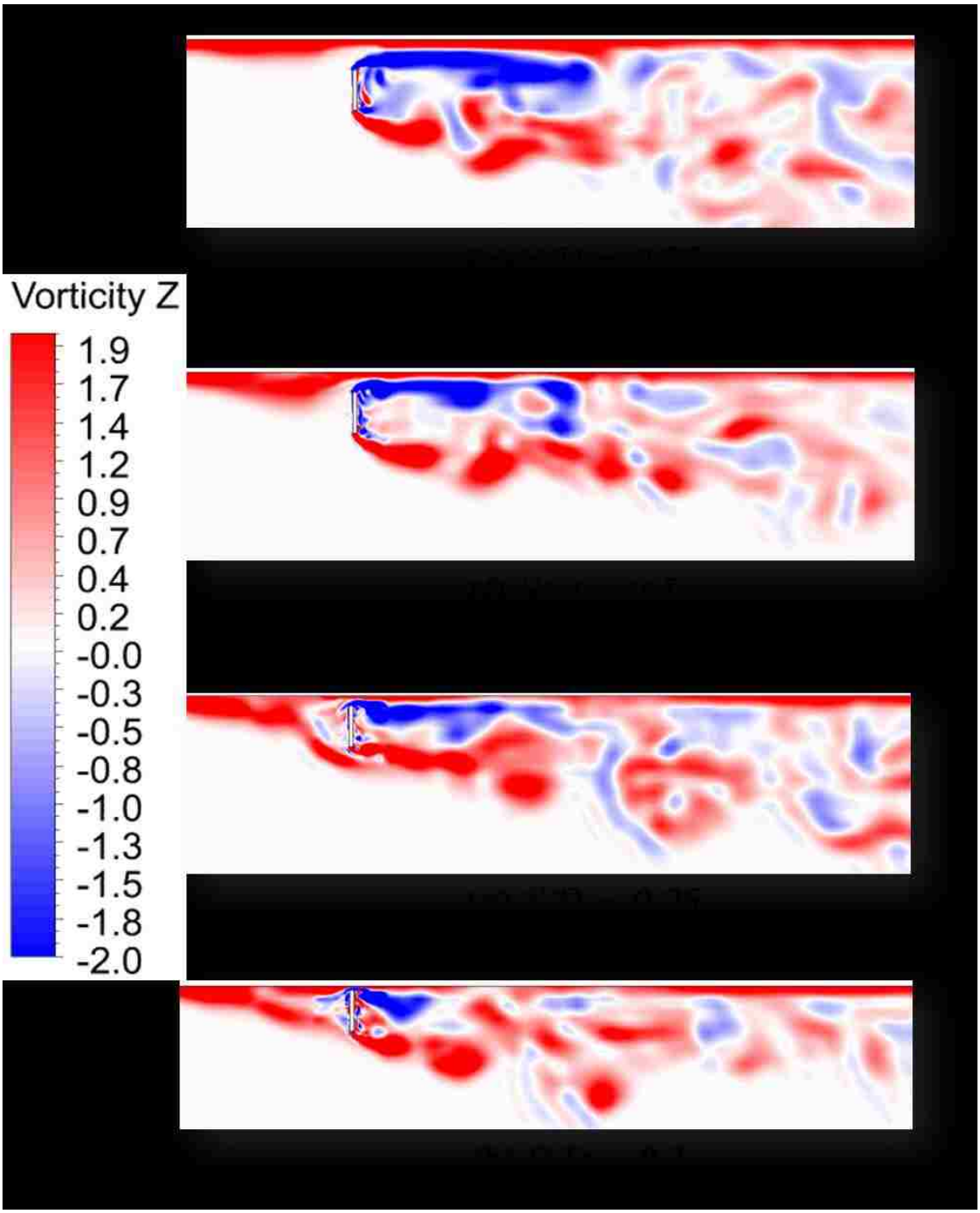

Figure 22. Contours of z- component of the vorticity at λ = 250 for various values of S/D = (a) 7.5, (b) 4.0, (c) 2.5, (d) 1.5, (e) 0.75, (f) 0.5, (g) 0.25, and (h) 0.1 at Z = 0 plane.

An illustration of vortex shedding is depicted in Figure 23 for S/D = 7.5. Figure 23 illustrates instantaneous isosurfaces of Q-criterion (Q = 0.01) in span-wise view for S/D = 7.5 and for $\lambda = 232 \leq \lambda \leq 250$. The time interval between each image is $\Delta\lambda = 4$ and the total time, $232 \leq \lambda \leq 250$, spans approximately two vortex shedding cycles. Tip vortices are observed at the side of the plate due to the presence of free ends. Shear layers generated from the top and the bottom edges of the plate convect downstream and roll up into vortices. The rolls of vortices shed from the top edge of the plate at various instances are indicated by numbers in open circles while vortices shed from the bottom of the plate are indicted by numbers in solid blue circles. These vortices travel downstream through time and expand in the cross-stream direction. Successive images shown in Figure 23 provides evidence of regular vortex shedding. Vortices shed from the top and bottom edges of the plate dominate the wake flow structure. The flow pattern presented here agree with LES result reported by Tian *et al*. [61] and DNS result reported by Hemmati *et al*. [63].

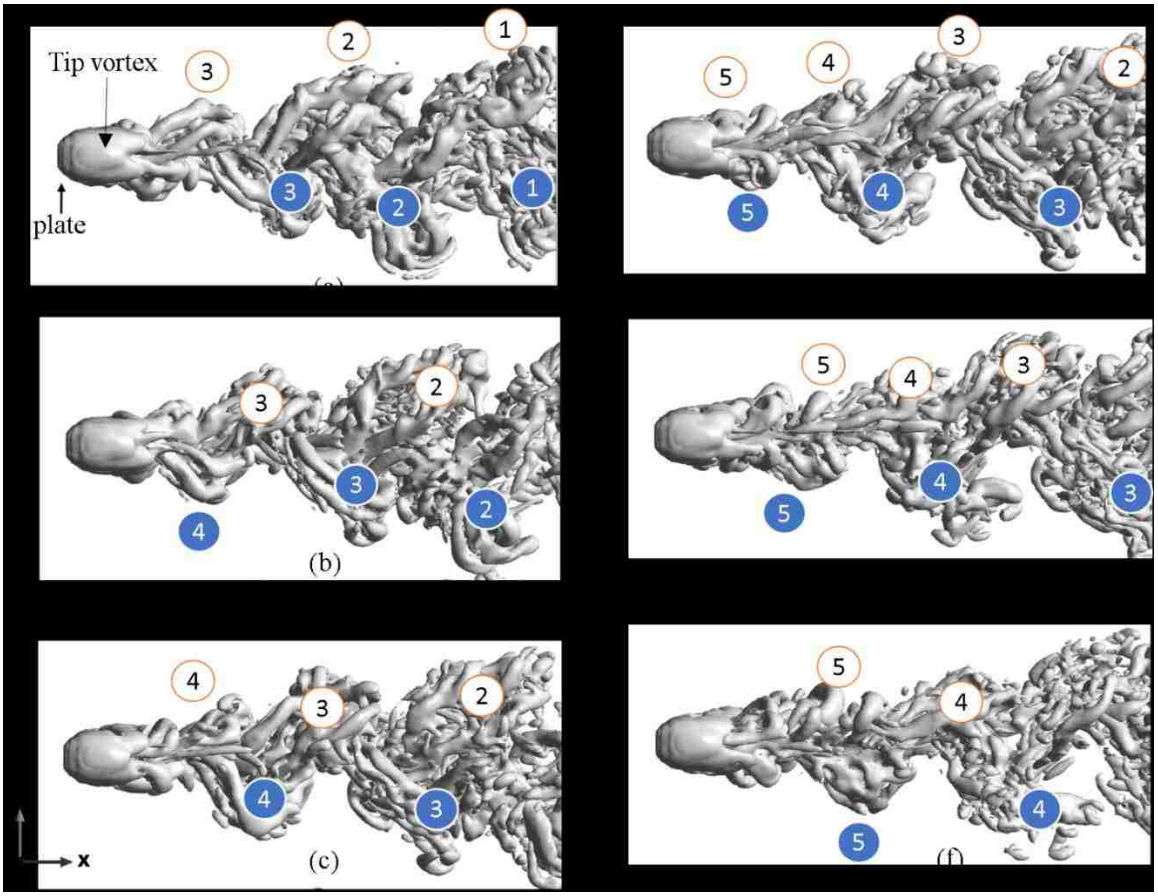

Figure 23. Instantaneous isosurfaces of Q-criterion (Q = 0.01) in the spanwise view (-z) for *S*/*D* = 7.5 and for 232 ≤ λ ≤ 250 at *Z* = 0 plane. The images are rendered at time interval of Δλ = 4.

Time signatures of drag and lift coefficients for *S*/*D* = 0.1, 0.5, 1.5, and 7.5 are depicted in Figure 24. Drag coefficients are plotted in the left column while lift coefficients are illustrated in the right column. The lift coefficient is defined by $C_L = F_L / \left(\frac{1}{2}\rho U_\infty^2 A\right)$, where F_L is the lift force acting on the plate. Time signatures for *S*/*D* = 0.1, 0.5, 1.5, and 7.5 are shown at rows, as indicated in Figure 24. For *S*/*D* = 0.1, the wall gap is smaller than the wall boundary layer thickness, 0.286*D*, hence the influence of the wall on the plate is pronounced. Such strong interactions induce larger amplitude

fluctuations in force coefficients. As the *S*/*D* increases, the wake become regular and the force coefficients exhibit stationary behavior.

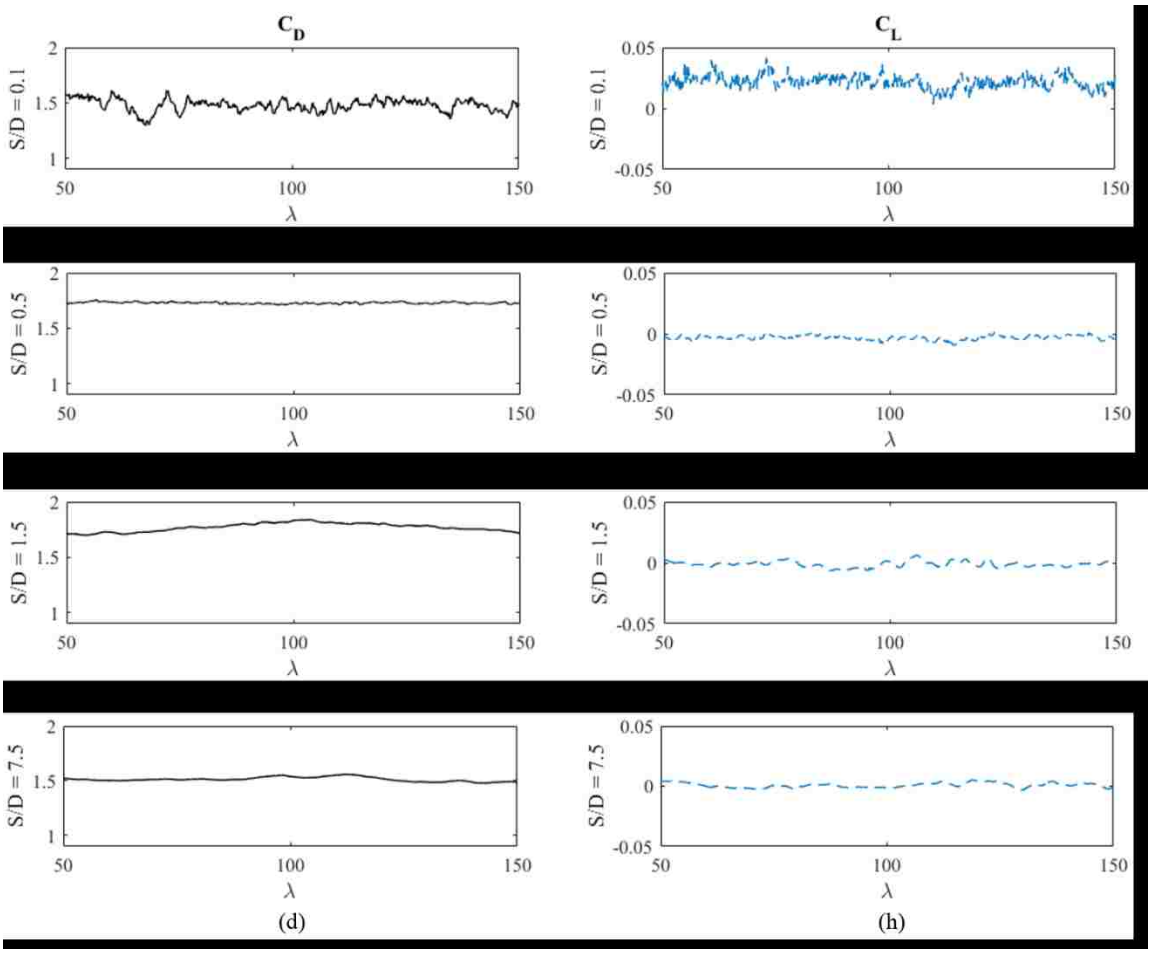

Figure 24. The drag (left column) and lift (right column) coefficients as a function of time for *S*/*D* of (a,e) 0.1, (b,f) 0.5, (c,g) 1.5, and (d,h) 7.5.

Drag and lift coefficients are plotted as a function of *S/D* in Figure 25(a) and Figure 25(b), respectively. The drag and lift coefficients presented in Figure 25 represent the time-averaged value. The error bars shown in Figure 25 are determined from the standard deviation calculated for each value of *S*/*D*. The larger value of the error bars

obtained when the plate is in close proximity to the wall are due to the strong interaction between the wall boundary layer and the wake flow behind the plates. Such interaction causes fluctuations in pressure exerted on the front and the back side of the plate, which results in larger amplitude fluctuations in drag coefficient. When the plate is placed away from the wall, the amplitude of fluctuations becomes significantly smaller. When the plate is placed very close to the wall, S/D = 0.1, the drag coefficient is calculated to be 1.48. C_D increases with the increasing S/D, it achieves a maximum at S/D = 1.5, and then decreases as S/D increases further from 1.5. The maximum value of the drag coefficient is calculated to be 1.75. It is also noted that the drag coefficient is lower compared to the drag coefficient of the plate in an infinite medium when the plate is placed inside the boundary layer.

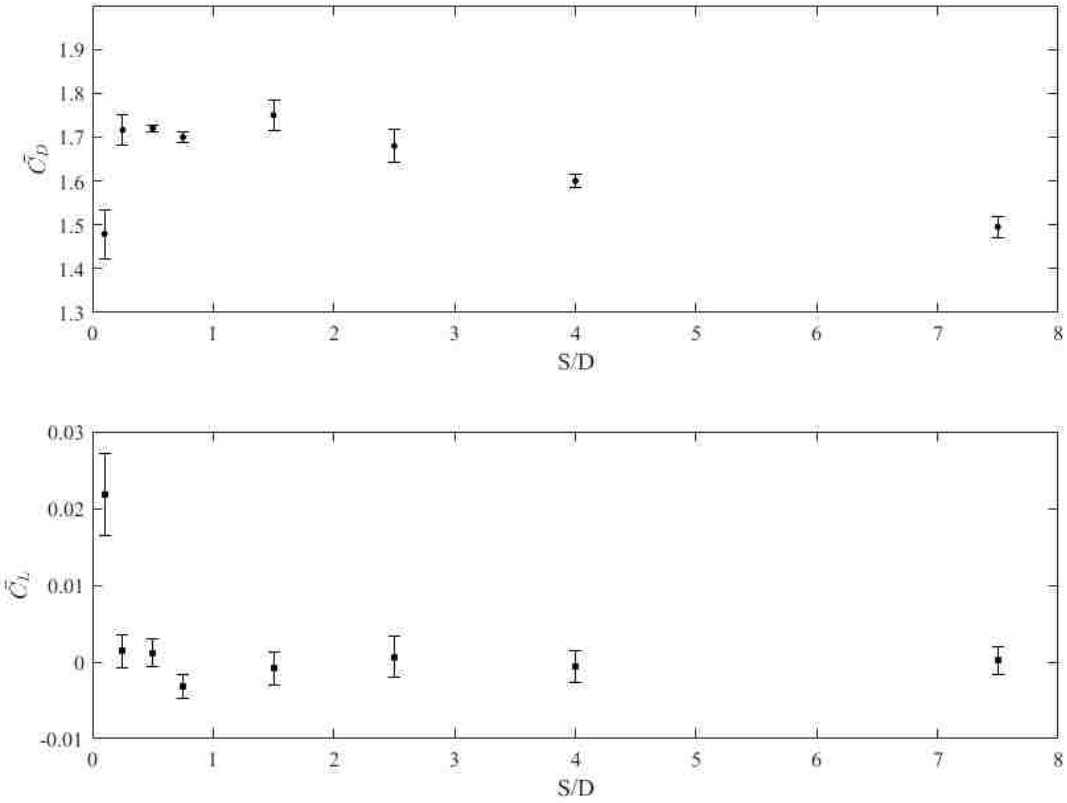

Figure 25. Time-averaged (a) drag coefficient and (b) lift coefficient as a function of *S/D*.

Large variation in drag coefficient is attributed to the strong variation in the pressure at the front and the back surfaces of the plate caused by the wall effect. Contours of pressure at the front and the back surfaces of the plate are shown in Figure 26. Images on the top row denote pressure contours over the front surface while images on the bottom row denote pressure contours over the back surface. As *S*/*D* decreases from 7.5 to 1.5, the pressure over the front increases slightly while the pressure over the back surface decreases. That results in an increase of the drag coefficient as *S*/*D* is decreased from 7.5 to 1.5. When the plate is placed inside the wall boundary layer, *S*/*D* = 0.25 and 0.1,

vortices induced by the wall boundary layer upstream of the plate give rise to a significant drop on the pressure over the front surface. While the pressure over the back surface has little change as the plate is placed closer to the wall. This explains the rapid drop of the drag coefficient when the plate is inside the wall boundary layer. The variation of C_D with S/D is consistent with what is reported in refs. [19, 64-70]. For $S/D \geq 1.5$, the regular Karman vortex shedding occurs and C_D asymptotically approaches 1.5 as S/D is increased. $C_D = 1.5$ is the value of the drag coefficient for flows past a single prism with free ends placed in an unbounded fluid domain. At larger values of S/D, as the influence of the wall becomes weaker, symmetrical wake flow patterns are observed. Tip vortices emanating from the free ends of the plate alter the pressure field around the plate. As a result, the drag coefficient for the plate with free ends is significantly lower than that of an infinite plate [37, 42, 63]. The drag coefficient of a finite plate with $L/D = 10$ for flows in an infinite domain is calculated to be 1.5 [71]. In the present study for the case of $S/D = 7.5$ the mean value of the drag coefficient is calculated to be 1.50, which matches well with what is reported in Liu *et al.* [71].

The lift coefficient is depicted in Figure 25(b) as a function of S/D. The mean value of the lift coefficient is nearly zero for large values of S/D, as seen in Figure 25(b). As stated several times earlier, the flow structures near the plate are symmetric when the plate is placed away from the wall. The time-averaged value of the lift coefficient is expected to be zero when flow field near the plate is symmetric about the center plane. The lift coefficient is calculated to be positive when the wall distance is smaller. It increases rapidly as the plate is placed in close proximity to the wall. Positive values of

lift coefficients characterize that the plate is pulled toward the wall as the wall influence gets stronger. Generally, the lift force caused by the near wall effect is due to either asymmetric vorticity distribution or pressure difference based on the inviscid theory [70]. Asymmetric vorticity results in a lift force that push the prism away from the wall. On the other hand, based on the inviscid theory, fluids passing through the gap between the plate and the wall have higher speed that causes a lower fluid pressure in this region. Such pressure difference creates a lift force that pushes the plate toward the wall. Lei *et al.*[64] and Nishino *et al*.[65] studied flow past a circular cylinder placed near a wall. These investigators documented that the cylinder is pushed away from the wall. Martinuzzi *et al*.[25] studied flow past a square prism near a wall. They reported that the prism is being pushed away from the wall at smaller wall gaps while at intermediate to larger gaps the prism is being pulled toward the wall. It has been reported that the prism can be pushed from or pulled toward the wall depending on geometry and flow conditions. For the plate geometry and flow conditions considered in the present study, it is demonstrated that the plate is being pulled toward the wall at smaller wall distances. The root-mean-square values of both drag and lift coefficients show that the amplitude of fluctuations of the drag and the lift is significantly larger when the plate is closer to the wall compare to that of when the plate is placed further away from the wall.

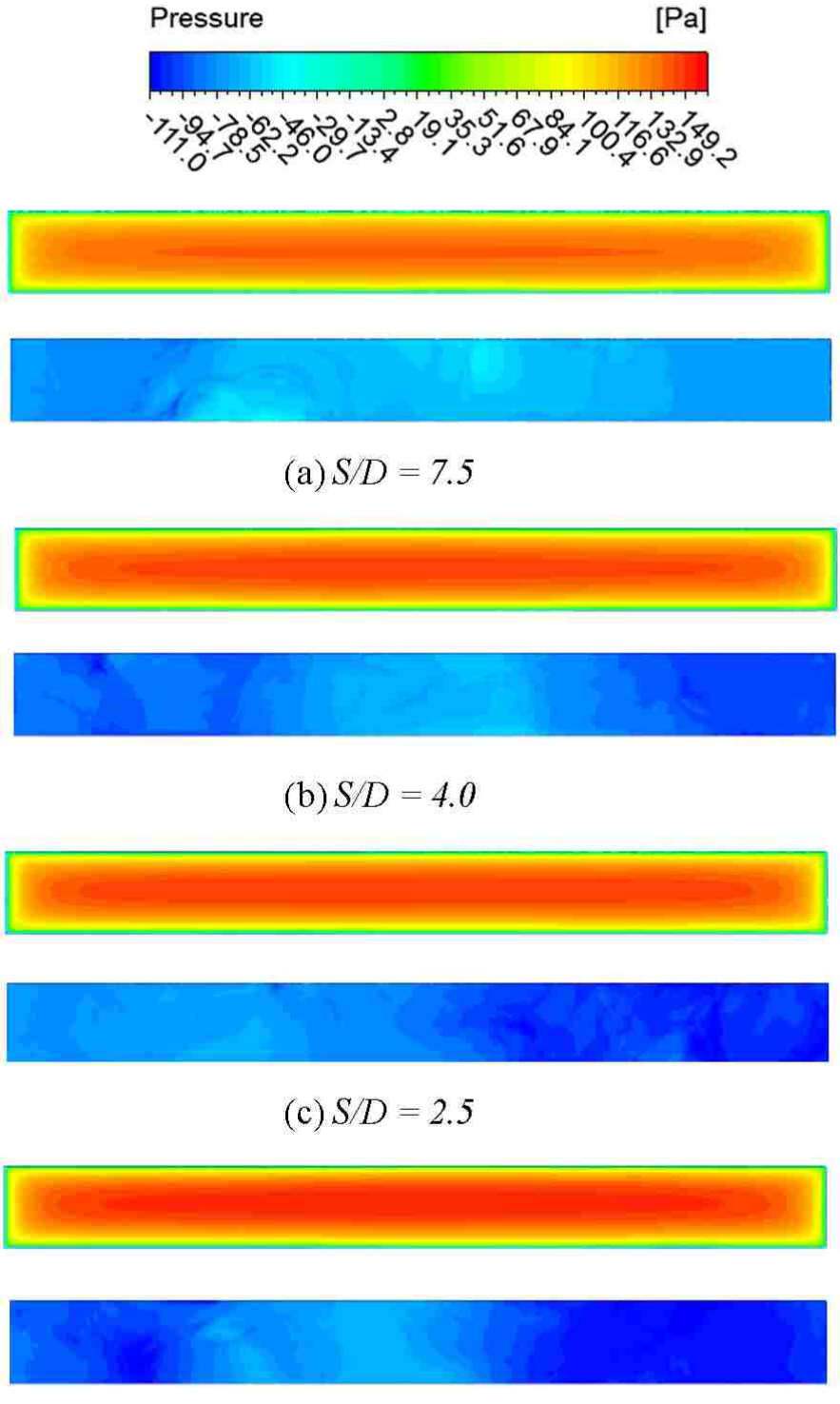

(a) $S/D = 7.5$

(b) $S/D = 4.0$

(c) $S/D = 2.5$

(d) $S/D = 1.5$

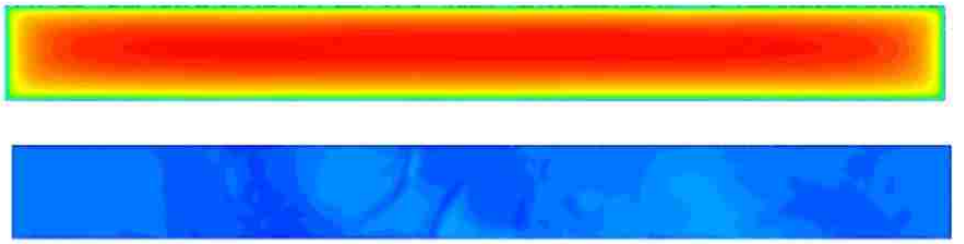

(e) $S/D = 0.75$

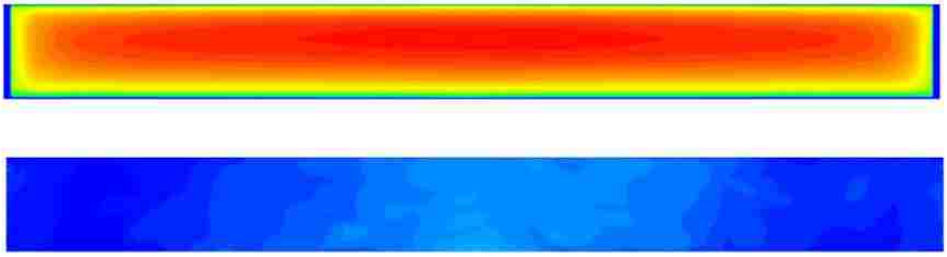

(f) $S/D = 0.5$

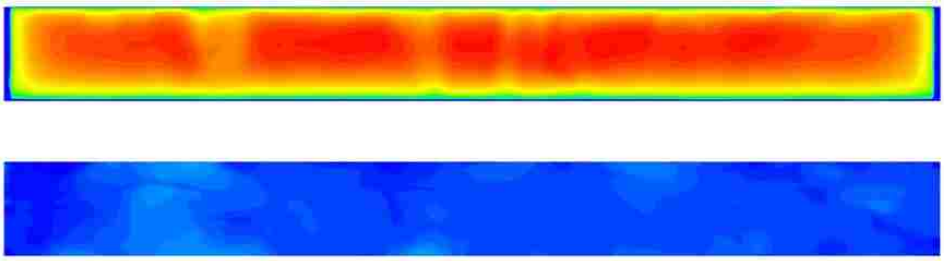

(g) $S/D = 0.25$

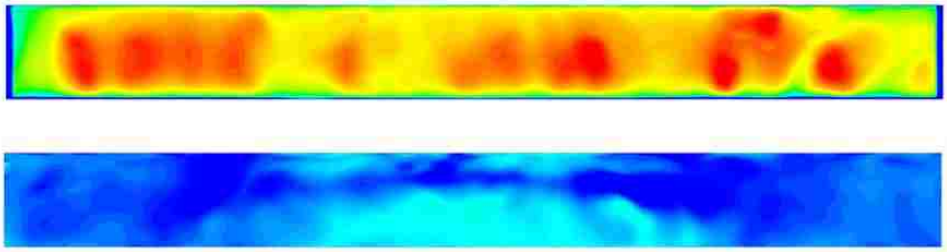

(h) $S/D = 0.1$

Figure 26. Pressure contours at the front and at the back surface of the plate for values of S/D = (a) 7.5, (b) 4.0, (c) 2.5, (d) 1.5, (e) 0.75, (f) 0.5, (g) 0.25, and (h) 0.1.

The time history of drag and lift coefficients and the corresponding fast Fourier transform (FFT) of the lift coefficient for the infinite plate, the finite plate, and the finite plate near a wall are depicted in Figure 27. The top and bottom boundary are located 8*D* away from the center of the plate. The boundary effect is negligible as the plate is placed far from walls [61] and [15]. By comparing the time history of the lift coefficient for the infinite plate and the finite plate, see Figure 27(a) and Figure 27(b), it is shown that the infinite plate has more regular vortex shedding and larger amplitude of fluctuations. The lift coefficient signal shows that the vortex shedding is mostly dominated by a single frequency, as depicted in Figure 27(d). On the other hand, the lift coefficient of the finite plate has more complicated dynamics. Presence of several modes with much smaller magnitude is obvious in the lift coefficient signal. Multiple dominant frequencies are shown in the FFT spectra, see Figure 27(e). Tip vortices originated from the free ends of the plate complicate the flow field, as described in refs. [37, 40, 42, 71]. Similarly, flows past a finite plate placed in the vicinity of a wall show the similar behavior as seen in Figure 27(c) and Figure 27(f). Defining Strouhal number ($St = fD/U_\infty$) for flows past a plate with free ends is not as clear.

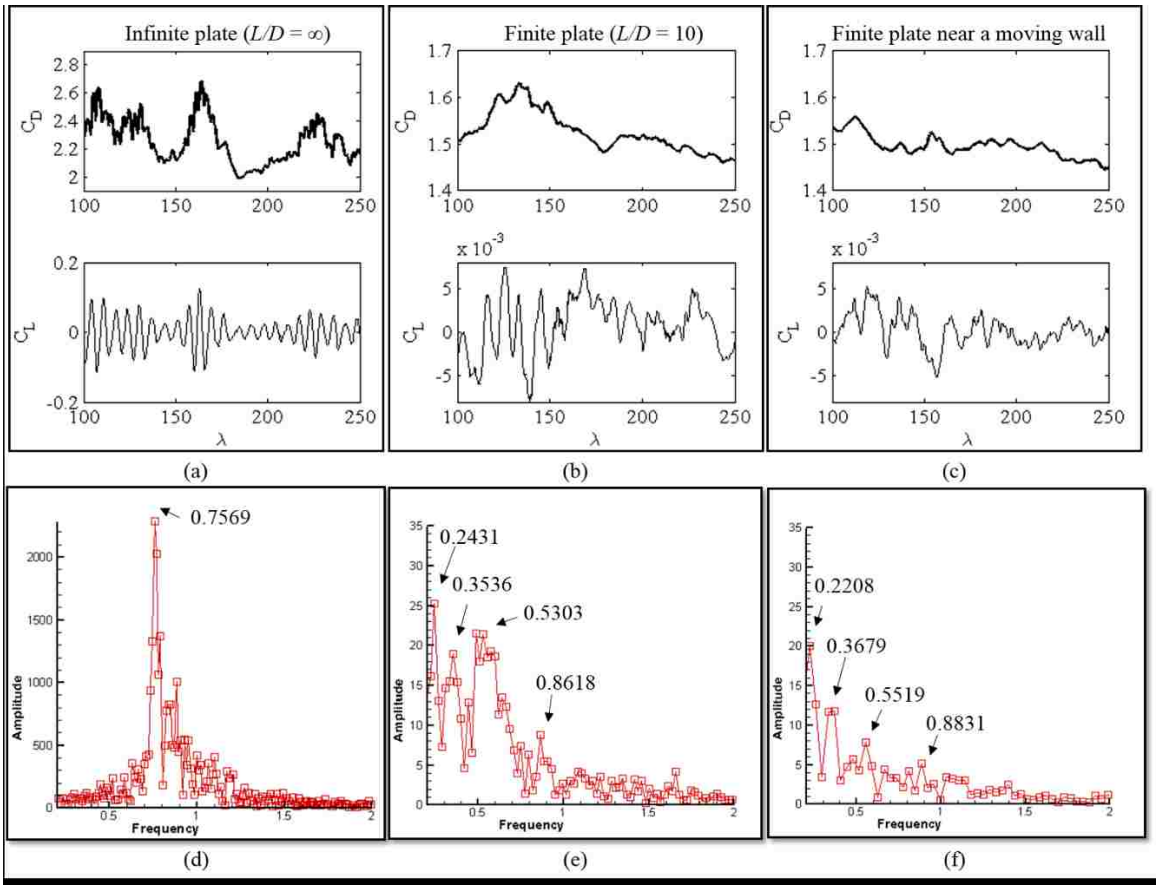

Figure 27. Drag and lift coefficient as a function of non-dimensional time λ and the corresponding fast Fourier transform (FFT) of lift coefficients at S/D = 7.5 for (a), (d) an infinite plate (b), (e) a finite plate (L/D = 10) and (c), (f) a finite plate (L/D = 10) near a moving wall.

Extended time history of the drag and lift coefficients for a finite plate with L/D = 10 is depicted in Figure 28 for the dimensionless flow time up to λ = 750. The drag signal demonstrates non-stationary behavior, as shown Figure 28. Irregular fluctuations in both drag and lift coefficients signal depicted here have also been reported by previous investigators for flow past a normal plate [5, 61].

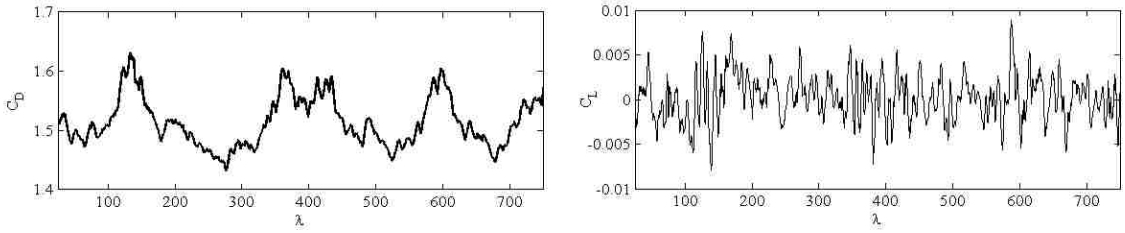

Figure 28. Drag and lift coefficient as a function of non-dimensional flow time λ for a finite plate (L/D = 10) at S/D = 7.5 with the entry length of 12D.

4.2.2 Flows past Staggered Arrays of Yawed Plates in the Vicinity of a Wall

The flow field around arrays of plates placed near a wall is examined next. Flow structures are characterized by interactions between wakes of both upstream and downstream plates and the boundary layer of the wall. It is demonstrated above that the drag coefficient is the highest for a single finite plate at S/D = 1.5. As a reference, S/D = 1.5 is selected to investigate flows past arrays of plates near a wall. It is well-documented in ref. [7, 11, 71] that flow patterns and hydrodynamic forces acting on the prisms are profoundly influenced by the value of G/D. Arrays of plates with G/D of 2.5 and 5 are considered here to characterize the flow structure around the plates subject to the wall proximity effects.

Flow patterns for a single plate and arrays of plates near a wall are depicted in Figure 29. Flow images over the X-Z plane (top view) and the X-Y plane (side view) are shown in Figure 29. Contours of the normalized vorticity are shown in Figure 29(a-c) acquired at Y = 0 plane while contours of the vorticity shown in Figure 29(d-f) are acquired at Z = 0 and Z = 6D planes, as labeled in the figure. Black dash lines in Figure 29(a-c) indicate locations of Z = 0 and Z = 6D planes. Flow images are shown in Figure

29(a, d) are for a single plate while flow images shown in Figure 29(b,e) and Figure 29(c,f) are for arrays of yawed plates with G/D = 2.5 and 5, respectively. Tip vortices generated from free ends of the perpendicular single plate are stronger than the tip vortices generated from the leading edge of yawed plates, see Figure 29(b,c). In addition, vortices emanating from surfaces of the perpendicular plate are uniformly distributed along the surface, while vortices generated from yawed plates are more concentrated toward the trailing edge of the plate. It is noticed that when the array of yawed plates is tightly spaced, G/D = 2.5, the flow near downstream plates is strongly influenced by the wake of the upstream plate, as shown in Figure 29(b). Vortices originated from the upstream plate impinge on the downstream plate. When the spacing is increased to G/D = 5, vortices shed from the upstream plate are partially impinge on the downstream plate and their intensities are much less compared to those for G/D = 2.5, as shown in Figure 29(c). The Karman vortex shedding occurs from both upstream and downstream plate individually, which indicates that flow patterns near the downstream plate are influenced less by the presence of the upstream plate.

Side view images acquired for arrays of yawed plates with G/D = 2.5 and 5 are illustrated in Figure 29(e,f), respectively. The image for a single plate perpendicular to the flow is presented in Figure 29(d) for comparisons. Regular vortex shedding from the top and bottom of the plate is seen in each case. As seen in Figure 29(d), due to the streamlining effect, shear layers separated from the perpendicular plate convected further downstream than shear layers generated from yawed plates. The effect of spacing (G/D) on flow structures is well documented in the literature [10, 72, 73]. At G/D = 2.5, vortices

emanate from the upstream plate and impinge on the downstream plate before they dissipate, as shown in Figure 29(e). For *G/D* = 5, however, the distance between the upstream and downstream plate is large enough that large-scale eddies generated from the upstream plates dissipate before they are impinged on the downstream plate, as shown in Figure 29(f). It should also be noted that there is a weak interaction between the boundary layer flow and the wake flow in these geometries with *S*/*D* = 1.5. Turbulent boundary layer thickness of the wall, δ_x, calculated at x=18*D* for the array geometry is estimated to be 0.396*D*, hence the plates are placed far from the wall boundary layer. When arrays of yawed plates are placed closer to a wall, vortices formed in the wall boundary layer are expected to be strongly interacted with the wake flow.

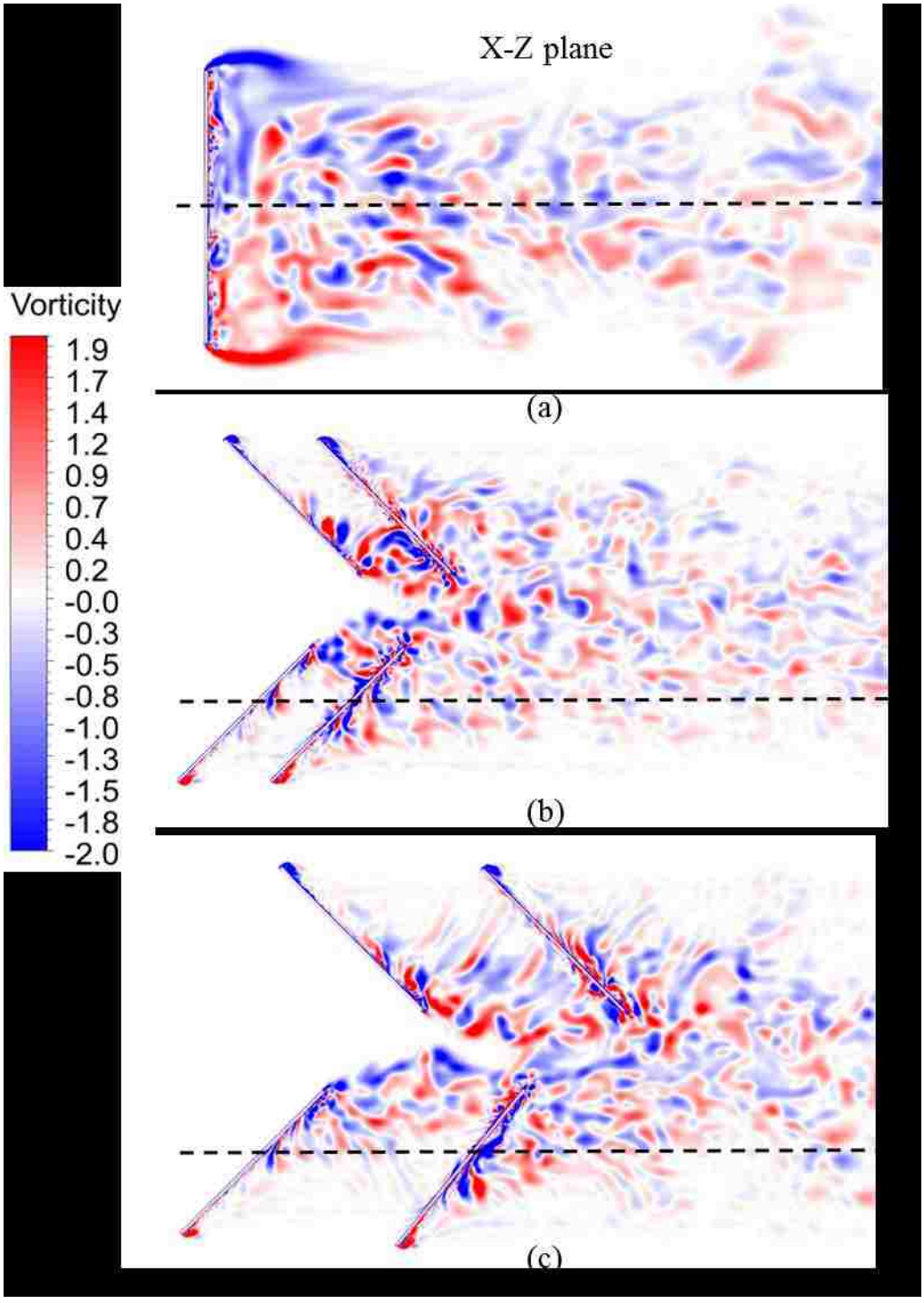
X-Z plane
Vorticity
1.9
1.7
1.4
1.2
0.9
0.7
0.4
0.2
-0.0
-0.3
-0.5
-0.8
-1.0
-1.3
-1.5
-1.8
-2.0
(a)
(b)
(c)

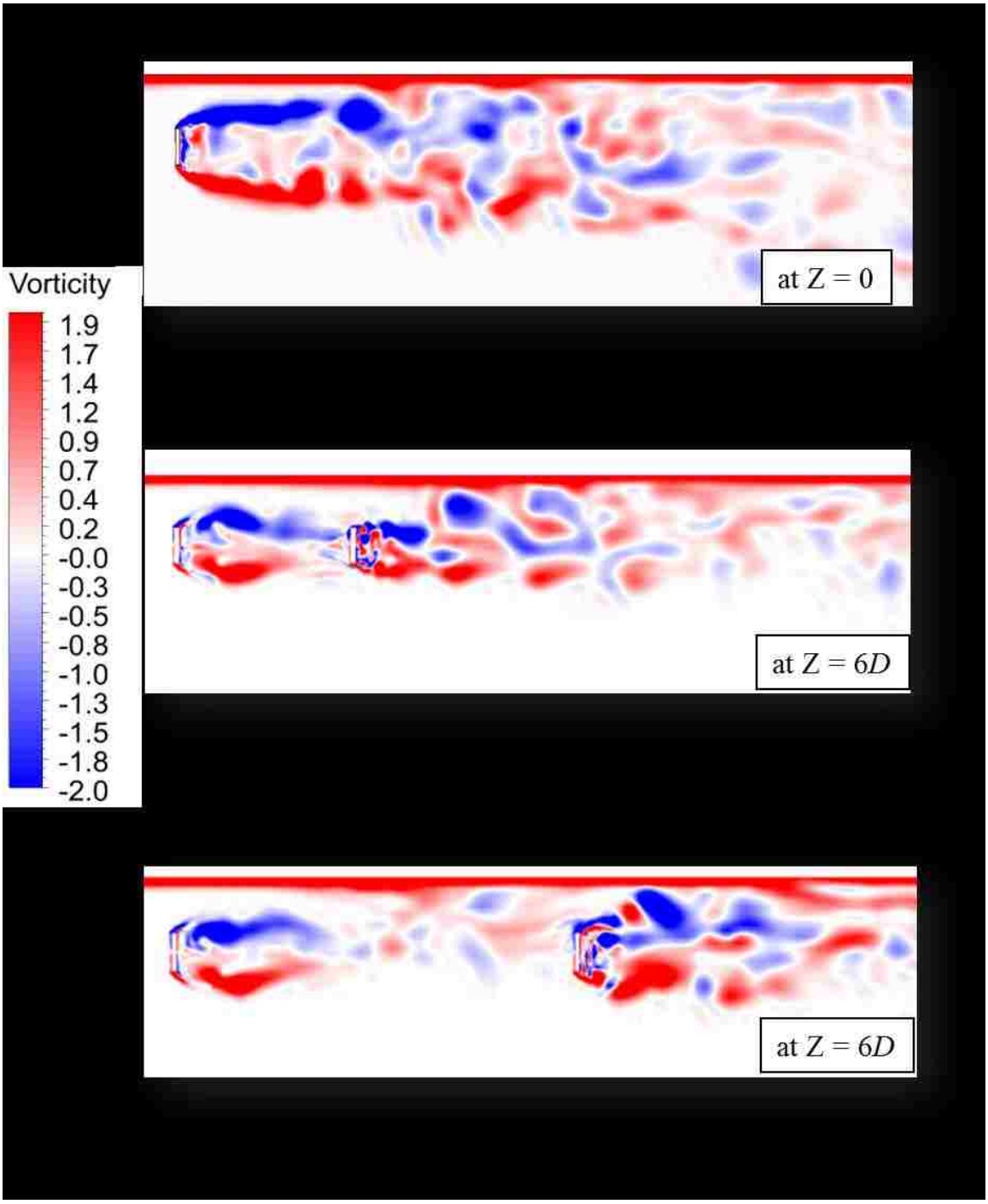

Figure 29. Contours of normalized vorticity at λ = 250 for a single and arrays of plates at *S/D* = 1.5. Images are for (a,d) single plate, (b,e) four plates array at *G/D* = 2.5, and (c,f) four plates array at *G/D* = 5.

The mean drag coefficient of plates, A1 to A4, for *S/D* of 1.5 and 7.5 and *G/D* of 2.5 and 5 are listed in Table 9. It is noticed that for *G*/*D* = 5 the drag coefficient of all plates in the proximity of wall are at least 12% larger than those placed away from the wall. For *G/D* = 2.5 the mean drag coefficients of upstream plates, A1 and A2, placed near a wall are greater compared to drag coefficient of plates placed away from the wall. Drag coefficient of downstream plates are insensitive to their proximity to the wall when they are tightly spaced. These results show that while staggered arrays of plates are under the influence of the wall, with adequate spacing the drag coefficient of plates are higher compared to the arrays of plates that are placed in infinite flow domain. These results will aid in designing marine current energy harvesting devices consisting of packed blades operating near platforms.

Table 9. Mean drag coefficient of yawed plates, A1 to A4, for various *S/D* and *G/D*.

	S/D = 1.5		***S/D = 7.5***	
G/D	**2.5**	**5**	**2.5**	**5**
$\overline{C}_{D\_A1}$	1.16	1.20	1.04	1.06
$\overline{C}_{D\_A2}$	1.25	1.29	1.08	1.11
$\overline{C}_{D\_A3}$	0.67	1.38	0.66	1.20
$\overline{C}_{D\_A4}$	0.67	1.07	0.66	0.92

4.2.3 Flow Past Arrays of Yawed C-Shape Plates Near a Wall

Simulations for flows past arrays of C-shape plates with *G*/*D* of 2.5 and 5 at *S*/*D* = 1.5 are performed here to characterize the effect of plate geometry on flow patterns and hydrodynamic forces. Flow patterns for arrays of yawed C-shape plates near a wall are

depicted in Figure 30. Isosurfaces of vortex structure at Q = 0.01 are shown in Figure 30(a, c), while vorticity contours over the *X*-*Y* plane (side view) acquired at *Z* = 6*D* planes are depicted in Figure 30(b, d). Images shown in Figure 30 (a, b) and Figure 30 (c, d) are for arrays of yawed C-shape plates with *G*/*D* = 2.5 and 5, respectively. Unlike arrays of yawed flat plates, vortices shed from each of the C-shape plates do not roll up together toward the center of the computational domain, as seen in Figure 30(a, c). More complex small eddies that have higher vorticity magnitude are observed near surfaces of C-shape plates. As shown in Figure 30(b, d), vortices generated from the top and bottom surfaces mixed with each other along the back side of the plate. Shear layers separate from the top and bottom surfaces for upstream C-shape plates, A1 and A2, does not extend further in the stream-wise direction when compared to the vortex structure for arrays of flat plates. Discontinuous vortices are because of the shape effect. Vortices shed from the top surface move downward and vortices shed form the bottom surface move upward, those vortices interact in the middle of the C-shape plate. These interactions create more complicated flow structures than arrays of flat plates. It is noted that for *G*/*D* = 2.5, vortex shedding from the upstream C-shape plates, A1 and A2, reattached to the downstream plates, A3 and A4. For *G*/*D* = 5, since the upstream C-shape plates and downstream plates are further away from each other, both of them generate Karman vortex shedding. Overall, in both cases of *G*/*D* = 2.5 and 5, the wake generated from upstream plates impinges on downstream plates, which explains why more small eddies are observed near downstream plates.

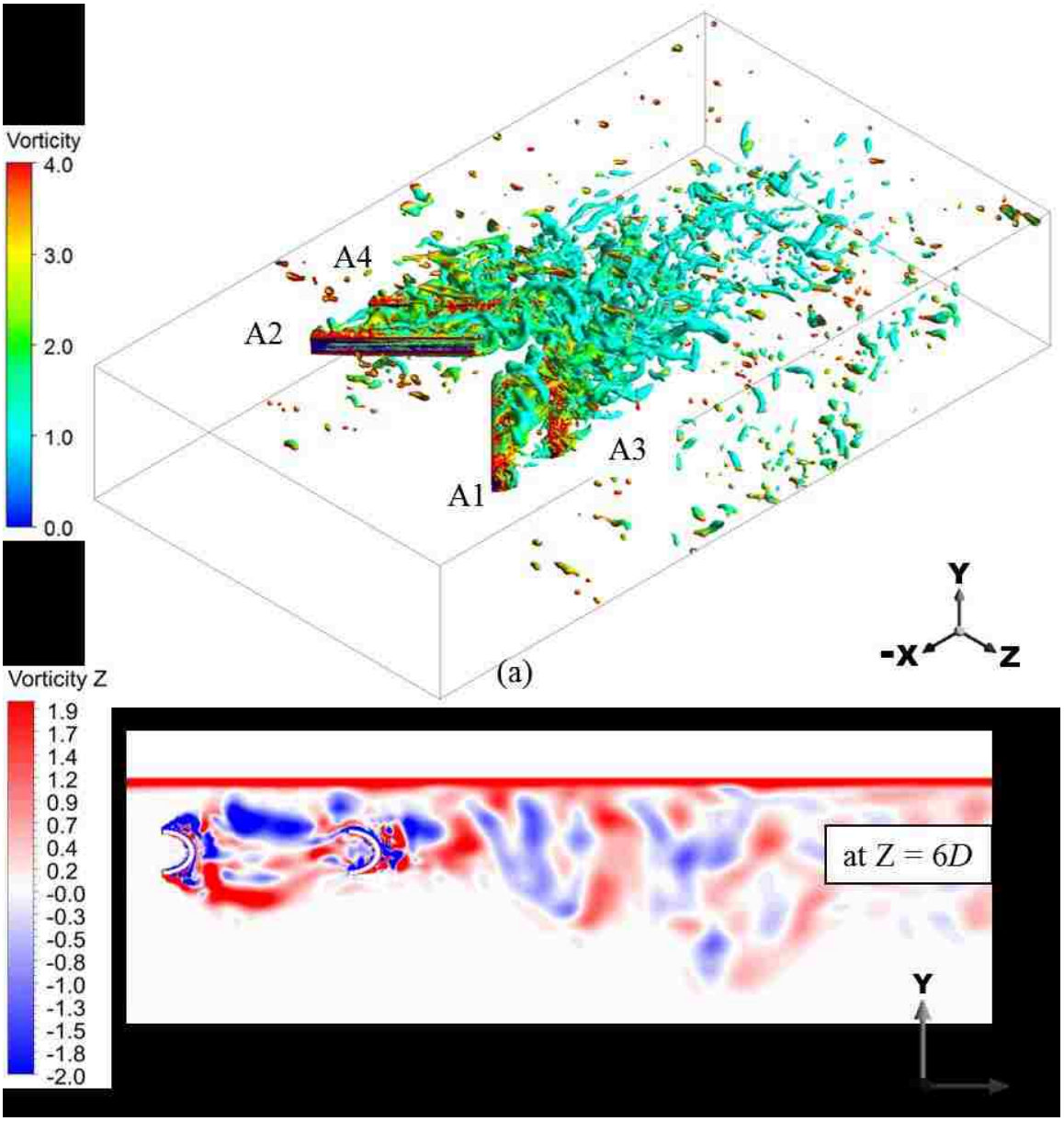
Vorticity
4.0
3.0
2.0
1.0
0.0
A4
A2
A3
A1
Y
-X
Z
(a)
Vorticity Z
1.9
1.7
1.4
1.2
0.9
0.7
0.4
0.2
-0.0
-0.3
-0.5
-0.8
-1.0
-1.3
-1.5
-1.8
-2.0
at Z = 6D
Y

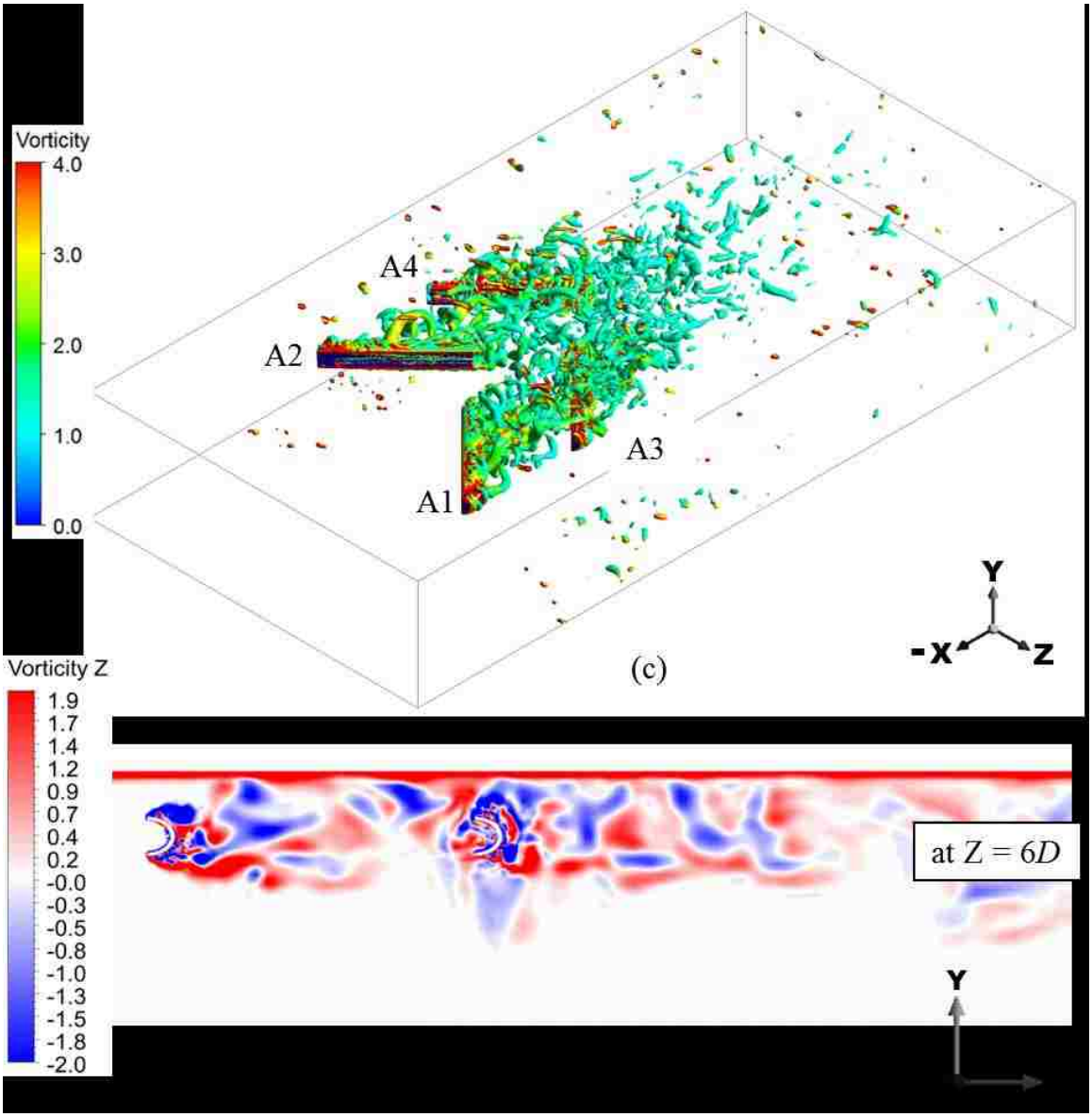

Figure 30. (a,c) Isosurfaces of vorticity at Q = 0.01 and (b,d) contours of normalized vorticity for C-shape plates at *S/D* = 1.5 and (a,b) *G/D* = 2.5, (c,d) *G/D* = 5.

Mean drag coefficients of C-shape plates, A1 to A4, for *G*/*D* of 2.5 and 5 at *S*/*D* = 1.5 are listed in Table 10. Generally, drag coefficients of C-shape plates are larger than that of flat plates. For *G*/*D* = 2.5, when the plates are tightly spaced, the mean drag coefficient of downstream plates are at least 55% lower than that of the upstream plates.

For G/D = 5, when the downstream plates are situated further away from the upstream plates, the mean drag coefficients for downstream plates are around 30% lower. Less decrease in drag coefficient means at spacing ratio 5, downstream C-shape plates are less influenced by the wake generated from upstream plates. Note that at G/D = 5, downstream plates in arrays of yawed flat plates have similar drag coefficients to upstream plates. At the same spacing ratio, drag coefficients for downstream C-shape plates are 30% lower than that of upstream C-shape plates. One can conclude that for C-shape plates in an array, downstream plates have to be placed further away than arrays of flat plates in order to minimize the upstream wake effect.

Table 10. Mean drag coefficient of yawed C-shape plates, A1 to A4, for G/D of 2.5 and 5 at S/D = 1.5.

	S/D = 1.5	
G/D	**2.5**	**5**
$\overline{C}_{D\_A1}$	1.61	1.64
$\overline{C}_{D\_A2}$	1.73	1.76
$\overline{C}_{D\_A3}$	0.72	1.22
$\overline{C}_{D\_A4}$	0.75	1.18

In summary, flows past arrays of finite plates near a moving wall were investigated in three-dimensional geometries. LES simulations were performed at Re = 50,000. Flow structures around a single plate for values of S/D range from 0.1 to 7.5 near a wall were presented. Flow patterns for staggered arrays of yawed plates at S/D ratio 1.5 and longitudinal spacing G/D ratios 2.5 and 5 were also examined. A shape effect was studied for arrays of yawed plates. Hydrodynamic forces acting on plates were calculated.

The influence of the wall is characterized in flows past a single finite plate as the wall gap was varied. When the plate was placed away from the wall, $S/D \geq 4$, symmetric flow patterns were observed similar to those in unbounded flows. Wake flow structures far downstream of the plate revealed that the wall influence onsets for $2.5 \geq S/D \geq 1.5$. As the plate was placed even closer, S/D = 0.75 and 0.5, vortices generated from the side closer to the wall were partially suppressed and asymmetric flow patterns were observed. At S/D = 0.25 and 0.1, the wall gap was smaller than the wall boundary layer thickness, 0.286D, vortices generated from the side closer to the wall were fully suppressed and eddies were formed upstream near the plate. The drag coefficient varied strongly with the wall distance. It is the lowest at S/D = 0.1 while it is the highest at S/D = 1.5. The drag coefficient asymptotes to 1.5 as S/D was increased from 1.5. For flow conditions considered in this study, the plate was pulled toward the wall while under strong wall proximity effect.

There were strong interactions between the wall boundary layer and the wake of yawed plates when staggered arrays of yawed plates were situated close to a wall. The drag coefficient of upstream plates at S/D = 1.5 were slightly greater than those placed far

away from the wall. The drag coefficient of downstream plates dropped significantly when plates were tightly spaced. While under the influence of the wall, staggered arrays of yawed plates encountered larger drag force than those of unbounded plates. The compact design of plate arrays within marine current energy harvesting devices enabled more power extraction. The present study demonstrated that while designing energy harvesting systems that operates beneath a platform or docks, the wall proximity effect should be taken into account.

CHAPTER 5 FLOW PAST A SINGLE PLATE IN THE VICINITY OF A FREE SURFACE

In this chapter, numerical simulations of two- and three-dimensional flows are carried out to investigate the change of flow field and hydrodynamic forces on the normal plate as the plate depth is varied. A validation simulation in three-dimensional geometry is conducted to compare with the experimental results provided by Malavasi and Guadagnini [14]. The flow pattern, drag and lift coefficients, and the Strouhal number as a function of plate depth (Froude number) are reported in this chapter. This study will aid the design of a hydropower system for river and ocean current applications.

5.1 Computational Overview – Two-Dimensional

The schematic of the flow geometry is shown in Figure 31. URANS VOF simulations in two-dimensional geometry are conducted at Re = 50,000. The Reynolds number is based on the upstream water velocity U_∞ and the plate height D. The entire fluid domain is divided into two parts: water at the bottom and air on the top. The upstream water velocity is set to be U_∞ = 0.5 m/s and the air velocity is set to be U_{air} = 0.01 m/s. The upstream water speed, U_∞, is the relative fluid speed with respect to the plate. The plate height is D. The plate is placed perpendicular to the upstream flow inside a flow channel, which is a simple duct with a height of 16D. The channel is large enough to eliminate the boundary effects from side walls. The coordinate origin is located at the plate center. The inlet is 20D upstream the plate to assure fully developed flow and the

outlet is 20*D* downstream the plate to obtain wake dynamics free of outlet effects. The depth to plate height ratio is $d^* = d/D$. Simulations are conducted for d^* of 7.5, 0.6, 0.5, 0.45, and 0.3. The corresponding local Froude number calculated based on depths of the plate are 0.18, 0.65, 0.71, 0.75, and 0.92, respectively. The property ratio between air and water for all the simulations presented in this manuscript are described as $\rho_1/\rho_2 = 1.23 \times 10^{-3}$, $U_{air}/U_\infty = 2.00 \times 10^{-2}$, and $\mu_1/\mu_2 = 1.82 \times 10^{-2}$. Modeling the flow past a plate normal to oncoming flow is achieved using ANSYS 14.5 Fluent simulation tool (see ANSYS theory guide and ANSYS user guide [57, 58]). Table 11 lists all the parameter values used in the simulations.

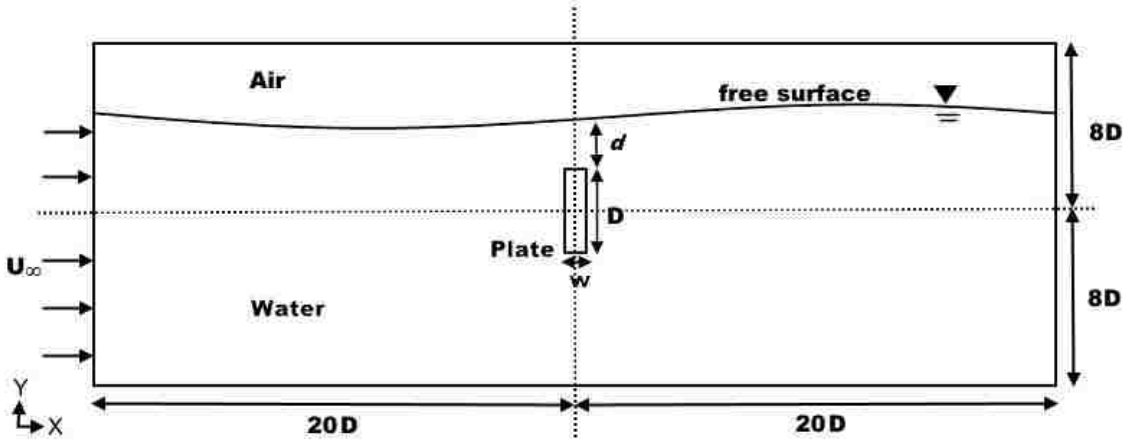

Figure 31. The schematic of the flow geometry.

Table 11. Parameter values used in the simulations

Parameter Values					
A	0.1	[m^2]	U_{air}	0.01	[$m\ s^{-1}$]
g	9.81	[$m\ s^{-2}$]	U_∞	0.5	[$m\ s^{-1}$]
D	0.1	[m]	w	0.01	[m]
d	0.75,0.06, 0.05, 0.045 0.03	[m]	ρ_2	1000	[$kg\ m^{-3}$]
Re_2	50,000	[-]	μ_2	0.001	[$kg\ m^{-1}\ s^{-1}$]

The combination of two separate models is required when modeling flows of two fluids separated by a free surface. Turbulence is modeled with the k-ω SST model [47] and the VOF multiphase model [55, 56] is used to determine interface dynamics separating water from air. In order to examine the free surface effect, the VOF model is necessary to track where the air-water interface is located.

The boundary conditions for the simulations are as follows. The mass flow rates for both water and air are specified at the inlet. The computational domain behind the plate is large enough, so zero gauge pressure is imposed at the outlet. At the inlet and the outlet, the free surface levels are defined in the VOF model based on the plate depth. A no-slip boundary condition is invoked on the plate surfaces, top, and bottom boundary.

The Semi-Implicit Method for Pressure-Linked Equations (SIMPLE) solution method is used to resolve the coupling between the pressure and the velocity fields. Discretization of time, momentum, turbulent kinetic energy and specific dissipation rate were accomplished through a second-order upwind scheme. The modified High Resolution Interface Capturing (HRIC) discretization scheme is used to solve the volume fraction equation. The transient simulation is stopped after the solution reached periodic stability.

5.2 Validation

In order to verify the accuracy of the multiphase simulation, a validation test is conducted. Malavasi and Guadagnini [14] provides experimental data of a rectangular cylinder in the free surface flow. The transient validation simulation in three-dimensional

geometry is to simulate one of the cases presented in the reference. The schematic of the geometry is shown in Figure 32. The channel is 5 m long with a cross-section width B = 0.5 m. The rectangular cylinder is fully submerged in water and the depth is represented as h^*, where $h^* = (h-h_b)/s$. Values of parameters used in the simulation are listed in Table 12. The case with the Reynolds number of 2.02×10^4, $h^* = 4$, and the ratio $h_b/s = 2.33$ is chosen to be modeled.

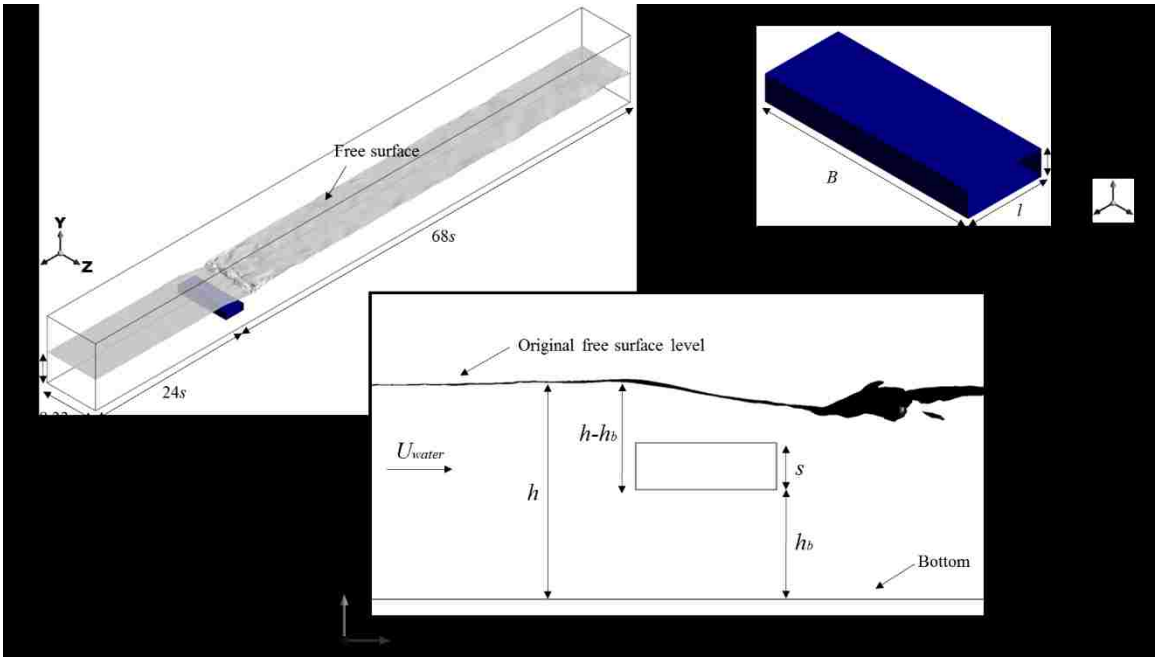

Figure 32. Geometry of the validation simulation.

Table 12. Parameter values used in the validation simulation.

Parameter	*Values*	
l	0.18	[m]
s	0.06	[m]
h	0.3798	[m]
h_b	0.1398	[m]
h^*	4	[-]
B	0.5	[m]
U_{water}	0.334	[m s^{-1}]

Figure 33 depicts the drag and lift coefficients as functions of time. The mean value of the drag and the lift coefficient, and the Strouhal number observed from validation simulation are 1.69, -0.67, and 0.17, respectively. These values are determined by the time signature of the drag and the lift coefficient at flow time 24 s to 32 s in order to avoid the initial transient effects. Predicted results from the present study have relative errors of less than 6% when compared with the drag and the lift coefficients and the Strouhal number documented by Malavasi and Guadagnini [14]. Figure 34 depicts an instantaneous velocity and vorticity contours for flow time 30.3 s. The black horizontal line above the rectangular cylinder indicates the free surface location, which is slightly perturbed from its resting state.

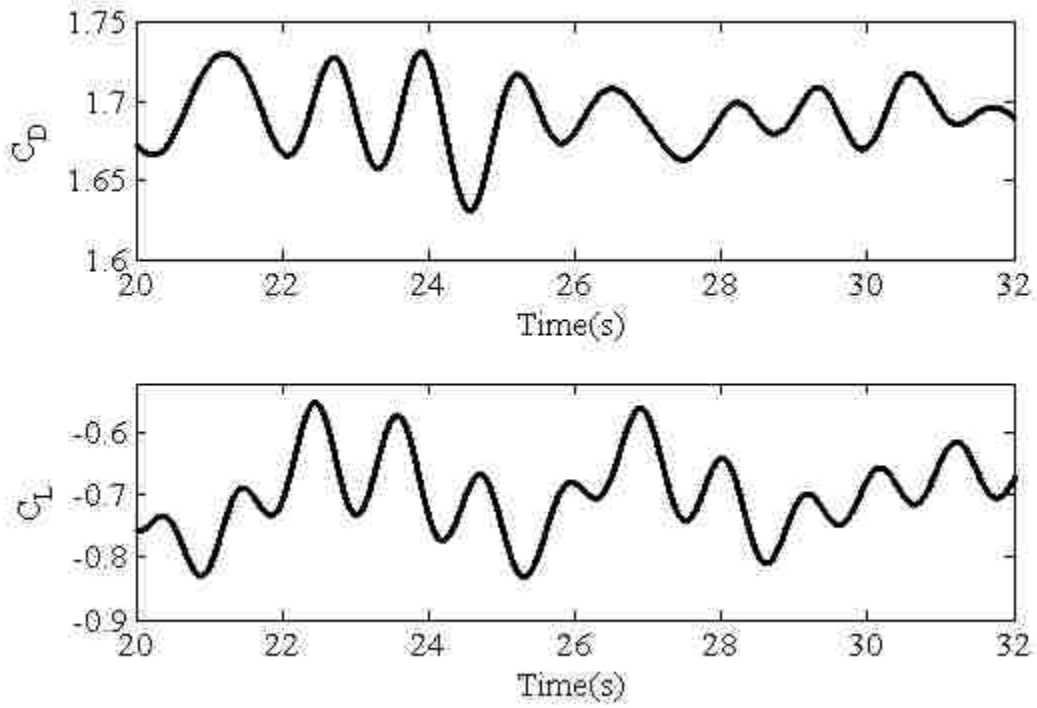

Figure 33. Drag and lift coefficients as functions of time. The validation simulation is conducted at Re = 2.02×10^4, h^* = 4, and h_b/s = 2.33.

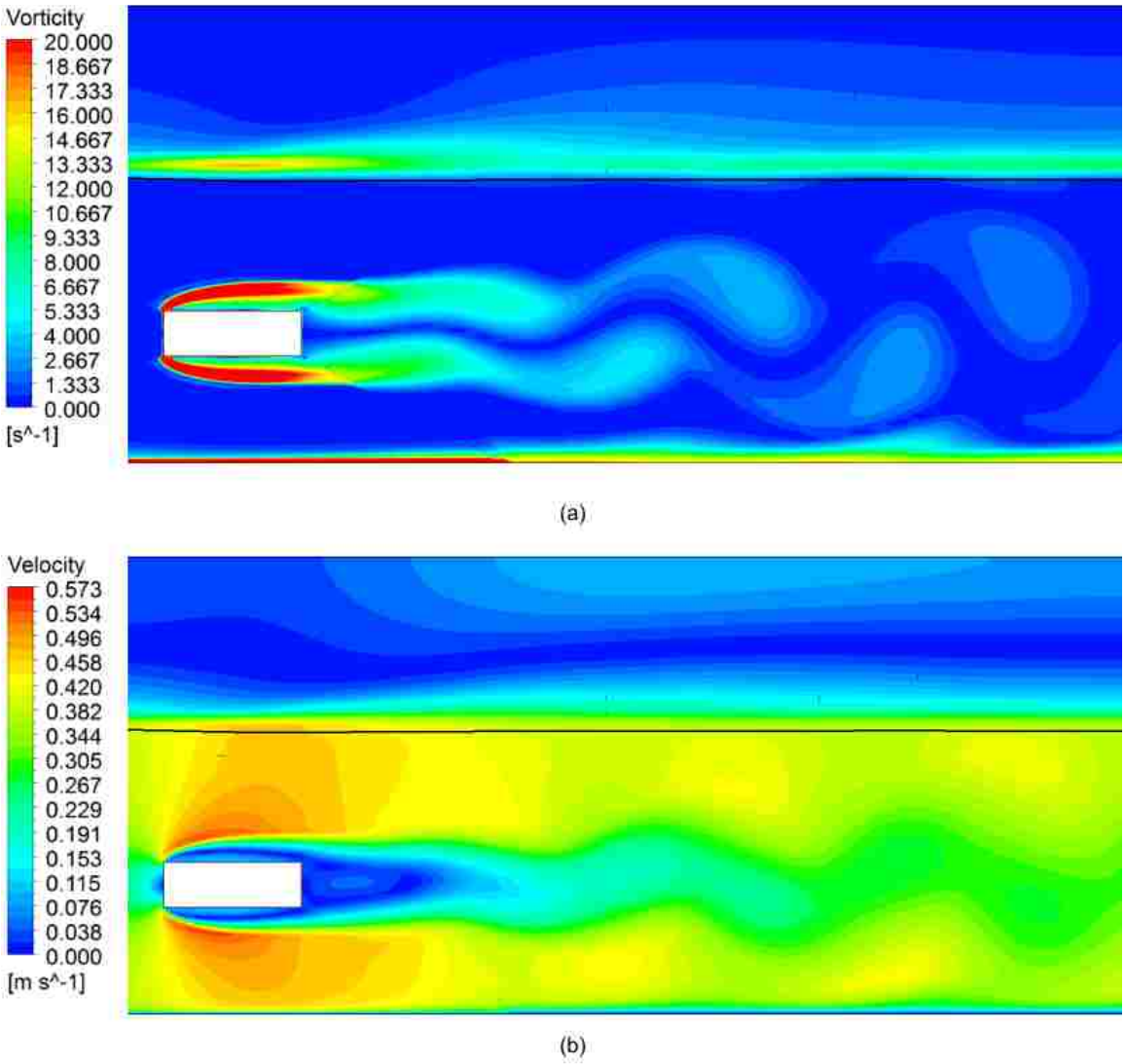

Figure 34. Instantaneous (a) vorticity and (b) velocity contours at t = 30.3 s. Validation simulation is conducted at Re = 2.02×10^4, h^* = 4, and h_b/s = 2.33.

5.3 Temporal and Spatial Convergence

The VOF model is susceptible to instabilities if non-orthogonal elements exist in the discretized fluid mesh. Therefore, the mesh used for the multiphase simulations must be carefully chosen to allow for acceptable accuracy as well as numerical stability.

Increasing the number of cells in the mesh may produce more accurate simulation results; however, a higher mesh density results in substantially longer computational time and increased CPU usage.

A spatial convergence test is conducted in order to assess the numerical accuracy of the simulations. The grid size used in this paper is verified using the Richardson extrapolation based Grid Convergence Method (GCI method) given in Celik, *et al.*[74]. This procedure is used to estimate the numerical uncertainty and error due to discretization in CFD studies. The methodology of this procedure is first to define a representative cell size. Second, select three significantly different grid sets N_1 = 90620 cells, N_2 = 158200 cells, and N_3 = 282050 cells. The grids are selected to make sure the refinement factors $r_1 = h_1/h_2$ and $r_2 = h_2/h_3$ are greater than 1.3, where $h_i = \left[\frac{1}{N_i}\sum_{j=1}^{N_i}\left(\Delta A_j\right)\right]^{\frac{1}{2}}$ is the representative cell size for the *i*th grid. The drag coefficient value is determined as the key variable of each grid. The grid convergence index (GCI value) is calculated to estimate discretization errors between grids. The GCI value for the finer grid should be relatively small to show that the solution can be replicated when the finest grid is employed. In the present study, the GCI value between meshes N_1 and N_2 is 2.9% and the value between meshes N_2 and N_3 is 1.1%. This indicated that the mesh size used in the study, N_3, provides results that can be considered mesh independent. The detailed description of the GCI method is presented by Celik, *et al.*[74].

A structured, hexahedral mesh is used for the computations. The mesh is finer closer to the plate walls and downstream of the plate to resolve the boundary layer and to observe vortex shedding. Figure 35 depicts the mesh in the vicinity of the plate.

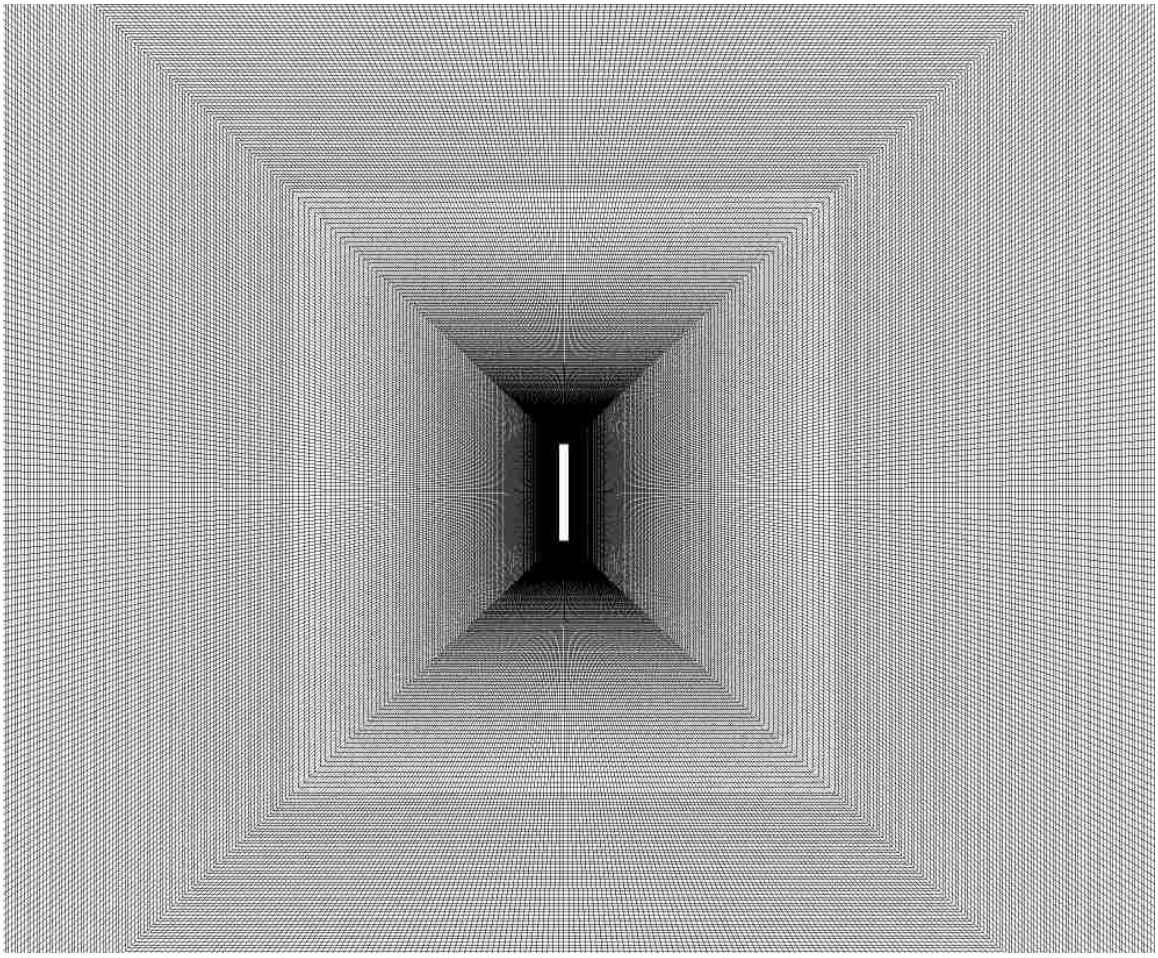

Figure 35. Structured mesh in the vicinity of the plate.

Discrete time steps are used in transient simulations. The sensitivity of the simulation results to the time step size must be examined to accurately capture the unsteady flow field. A temporal convergence test is conducted for the case of plate depth equal 0.6*D*. Drag coefficients are determined for three time step sizes Δt = 0.008 s, 0.0016 s, and 0.00032 s with corresponding values of 3.32, 3.55, and 3.55. This shows that Δt = 0.0016 s is sufficient to ensure the temporal convergence.

A non-dimensional wall distance in a wall-bounded flow is defined as $y^+ = u_* y/\nu$, where u_* is the friction velocity at the nearest wall and y is the distance to the nearest wall. The average y^+ value at the plate wall for cases of Fr = 0.18, 0.65, 0.71, 0.75, and 0.92 are 4.76, 3.31, 2.81, 2.57, and 1.80, respectively. The y^+ values are all below 5, ensuring that the viscous sublayer is numerically resolved. The Courant number ($C = u\Delta t/\Delta x$) is a non-dimensional parameter that describes how fast flow information is propagated through the computational domain. The Courant-Friedrichs-Lewy (CFL) condition is a numerical stability criterion that requires $C \leq 1$ for a stable, unsteady solution. The average value of the Courant number for all plate depths cases are all below unity. The maximum value of the local Courant number is 46.2, which occurs at a few cells near the top and the bottom plate corners.

5.4 Results and Discussions

5.4.1 Multiphase and Single Phase Flows

For additional validation of the model, results predicted by the multiphase model are compared to those predicted by the single-phase model. The single-phase simulation considers the flow past a plate in a nearly infinite fluid domain. In order to make the boundary conditions of the multiphase simulation similar to the single-phase simulation, the plate is fully submerged in the channel and oriented at a distance of approximately 7.5D away from the water surface. The volume fraction contour of multiphase simulation is illustrated in Figure 36. As shown in Figure 36, the water depth of the multiphase

simulation is set to be the same as the channel height in the single-phase simulation. Figure 36 shows no disturbances at the water surface, which suggests the flow field near the plate is not influenced by the presence of the free surface. Therefore, the results of the multiphase simulation should be identical with the single-phase simulation.

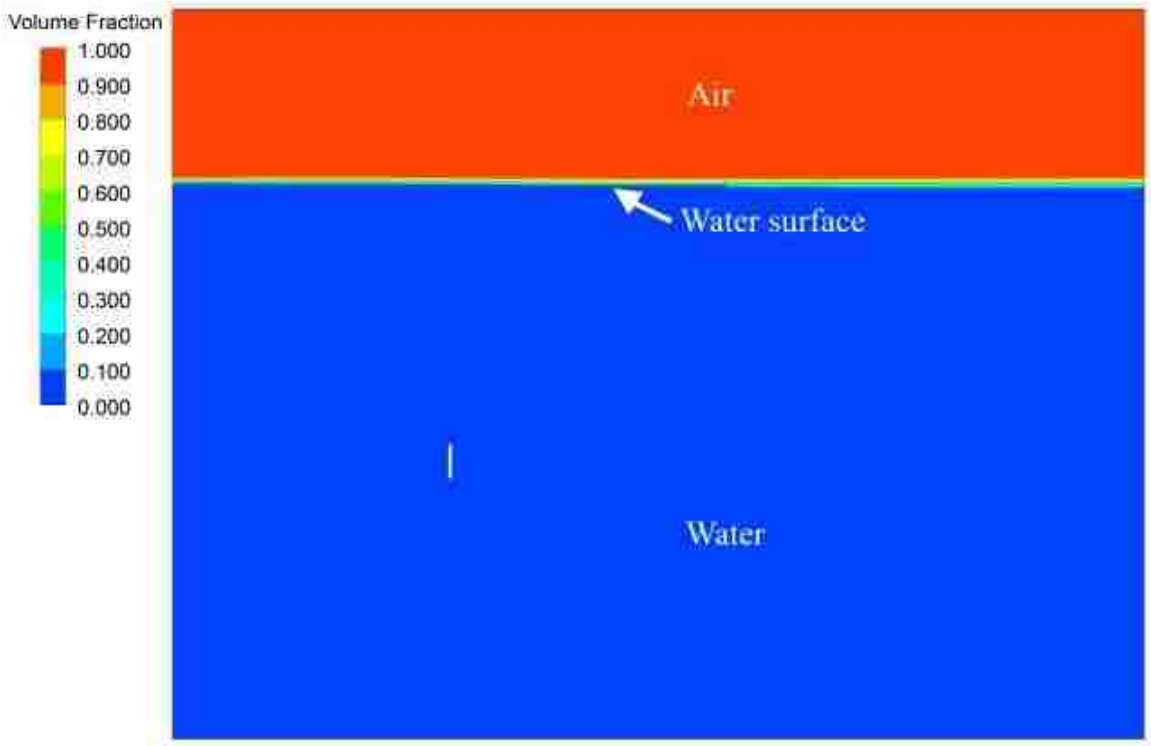

Figure 36. Volume fraction contour predicted by multiphase simulation.

Figure 37 depicts the same velocity and vorticity distribution for both single-phase and multiphase simulations. Figure 37(b) shows the vortices shed from both the top and bottom surfaces of the plate interact with one another, which then gradually dissipate downstream. The vortices are shed alternatively from the top and the bottom corner of the plate and generate a regular flow pattern in the wake. Other than the volume fraction and

the vorticity contour, the mean drag coefficient and the Strouhal number are calculated from at least ten vortex shedding cycles. As reported by many earlier investigators [5, 6, 60, 75-77], the two-dimensional flow simulation over predicts the drag coefficients. Najjar and Balachandar [60] compared the numerical results for two-dimensional and three-dimensional simulations, indicating that the three-dimensional effect is the reason for the over prediction of the two-dimensional simulations. The present study is in agreement with the two-dimensional numerical results reported in the literature. The drag coefficient value and the Strouhal number for the single-phase simulation are 3.86 and 0.125, while the same values predicted by the multi-phase simulation are 3.86 and 0.126, respectively. Results show that the single-phase and multiphase simulations yield identical values for desired performance characteristics regardless of the use of multiphase VOF model when the plate is sufficiently far away from the free surface.

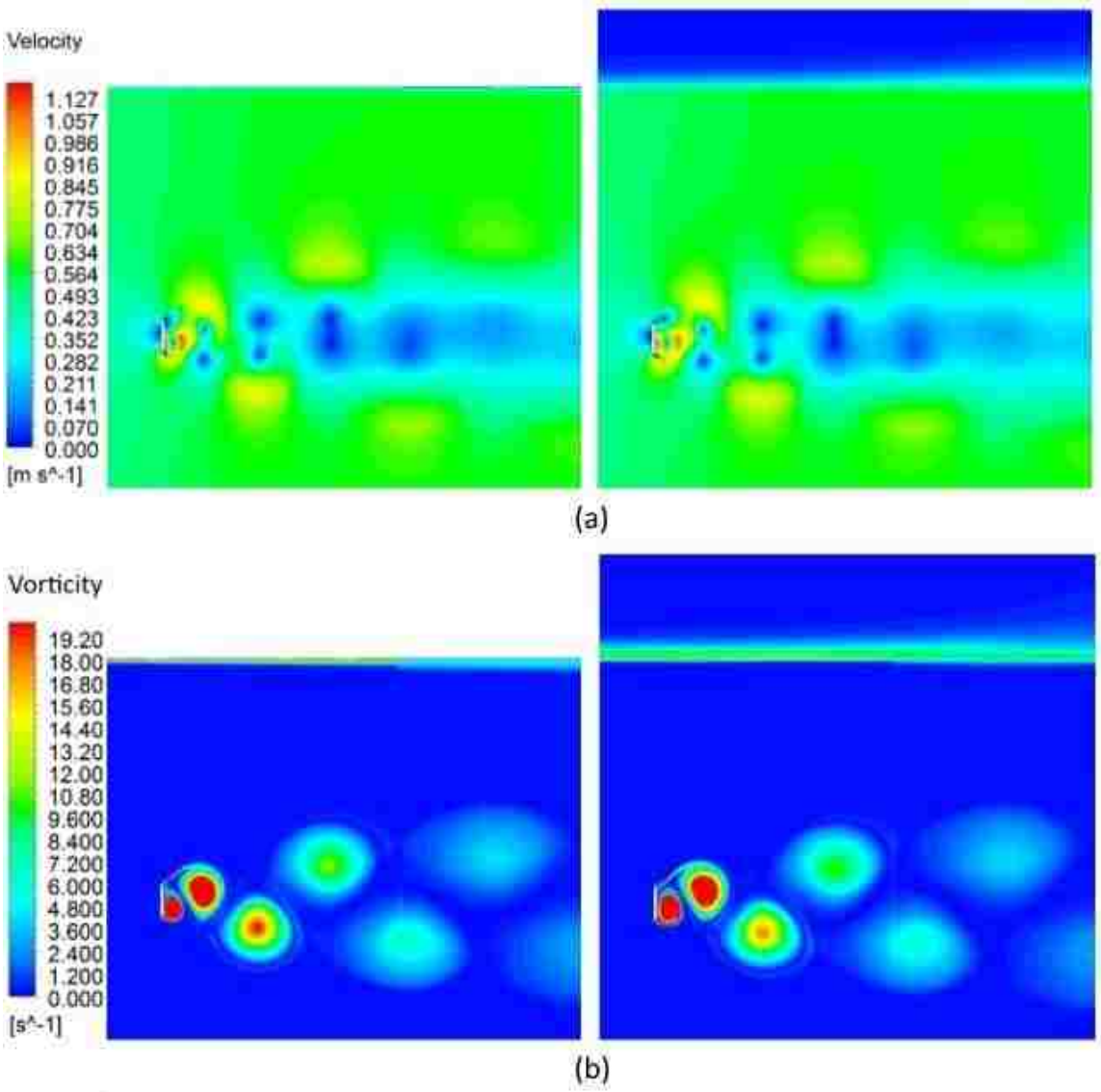

Figure 37. Instantaneous (a) velocity and (b) vorticity contours. Results of single-phase simulation are shown in the left column and the results of multiphase simulation are shown in the right column.

5.4.2 Volume Fraction Contours

Investigating the free surface effects is the primary focus of this study. It is observed that the proximity of the plate to the surface has a profound effect on the spatial

and temporal characteristics of the vorticity and velocity field. The wake structure is distinctly different from the deeply submerged plate.

Figure 38 shows the instantaneous volume fraction contour at different plate depths. The volume fraction contour depicts the local air and water fraction, where zero represents pure water and one represents pure air. When the plate is submerged 7.5D (Fr = 0.18), no surface deformation is observed. When the plate is 0.6D submerged (Fr = 0.65), some surface deformation is observed. The flow above the plate interacts with the surface, resulting in a drop in the surface right behind the plate. The surface wave decays in magnitude far downstream of the plate. When the plate is submerged 0.3D (Fr = 0.92), additional fluctuation along the surface is observed. As depicted in Figure 38(c), more air is entrained into the water region behind the plate and results in larger surface distortion.

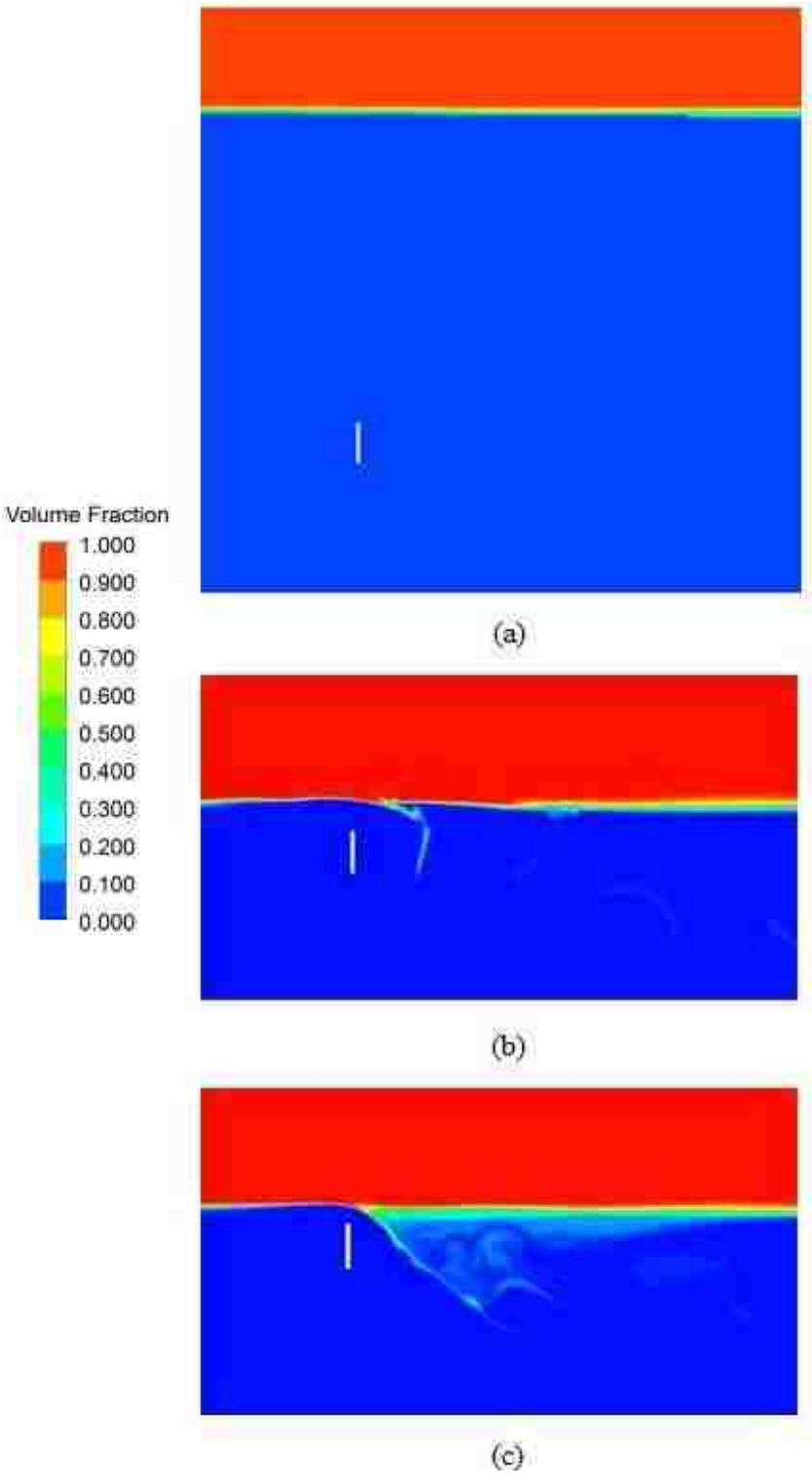

Figure 38. Instantaneous volume fraction contour for (a) *Fr* = 0.18 at t = 26.4 s, (b) *Fr* = 0.65 at t = 28.8 s and (c) *Fr* = 0.92 at t = 28 s.

5.4.3 Flow Patterns

The present study observes similar flow features as depicted in Miyata *et al*. [26] and Sheridan *et al*. [29]. Figure 9 illustrates the velocity and vorticity contour for different values of the Froude number. The black horizontal line above the plate shown in Figure 39(b) and (c) indicates the free surface location. The free surface penetrates into the plate's near wake as the Froude number becomes larger. Vortex shedding alternating between upper and lower plate boundary is observed in all cases. The vorticity contour shows that the free surface has a drastic effect on the flow. The vortex shedding is symmetric and regular for Fr = 0.18 as seen in Figure 39(a). For the cases of Fr = 0.65 and 0.92 (Figure 39(b,c)), the upper vortex shedding component is influenced by the free surface, resulting in asymmetric vortex shedding and irregular flow patterns in the wake. As shown in Figure 39(b) for the case of Fr = 0.65, the large-scale vortex shedding is asymmetric. The upper vortices are dissipated by the free surface and then break into small eddies near the surface, leaving the bottom vortices to dissipate further downstream. When the plate approaches even closer to the surface as shown in Figure 39(c) for the case of Fr = 0.92, a vortex forms above the top of the plate and adjacent to the free surface. A jet-like flow is observed from the free surface on top of the plate. This jet-like flow is dominated by the vortices generated from the free surface, which induce strong free surface deformation. Smaller vortices are seen in this case compared to others. The jet flow tends to merge with the vortices originating from the bottom of the plate. The vortex shedding from top and bottom of the prism are pushed downward due to the presence of the jet-like flow. Moreover, the upper vortices are not only compromised by

the free surface, but are also blended together with the bottom vortices and dissipate together downstream and the wake flow becomes even more irregular. Characteristics of the drag and lift coefficients are directly affected by different vortex shedding motions.

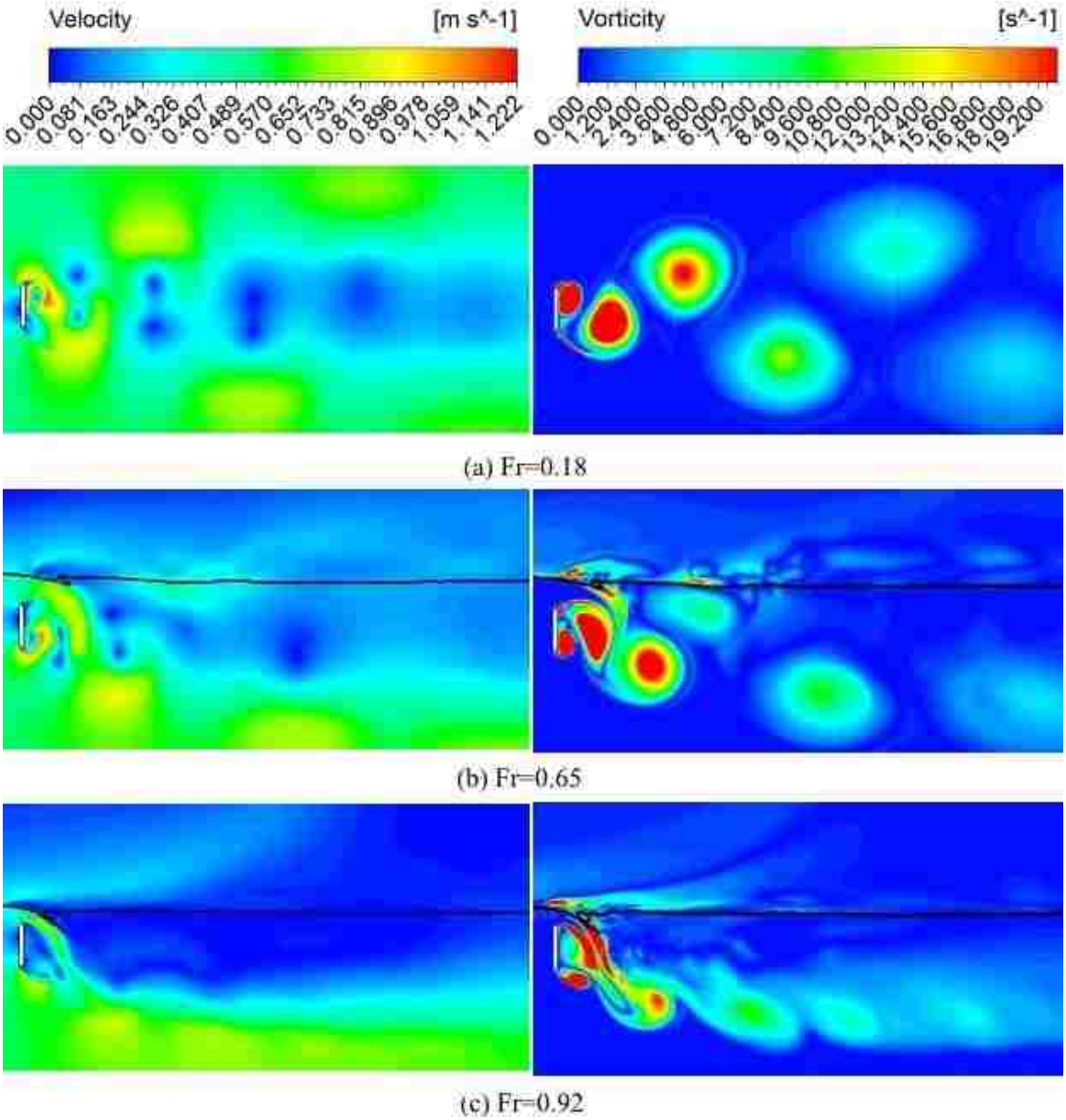

Figure 39. Instantaneous velocity and vorticity contours for (a) *Fr* = 0.18 at t = 26.4 s, (b) *Fr* = 0.65 at t = 28.8 s and (c) *Fr* = 0.92 at t = 28 s.

The profiles of time averaged streamwise component of the velocity at the upstream and the downstream of the plate are shown in Figure 40 for Fr = 0.65. The velocity profiles are averaged over 5 vortex shedding cycles. Upstream velocity profiles are plotted at locations 2.5D, 5D, 12D, 14D, and 16D away from the plate, as depicted in Figure 40(a). The velocity profiles at about 12D and 14D from the plate are nearly the same; suggesting that the fully developed flow conditions are attained at these locations. The velocity profiles approaching plates (5D and 2.5D) are influenced by the presence of the plate and the free surface. The water speed decreases near the free surface due to the slower air velocity above. Downstream velocity profiles are plotted 1D, 2.5D, 5D, and 10D away from the plate, as depicted in Figure 40(b). Irregular flow pattern caused by the interaction of the vortices shed by the plate, and the free surface effects in near wake velocity profiles are shown at 1D and 2.5D away from the plate. Further away from the plate at 5D and 10D the velocity profiles gradually recover to regular wake flow patterns.

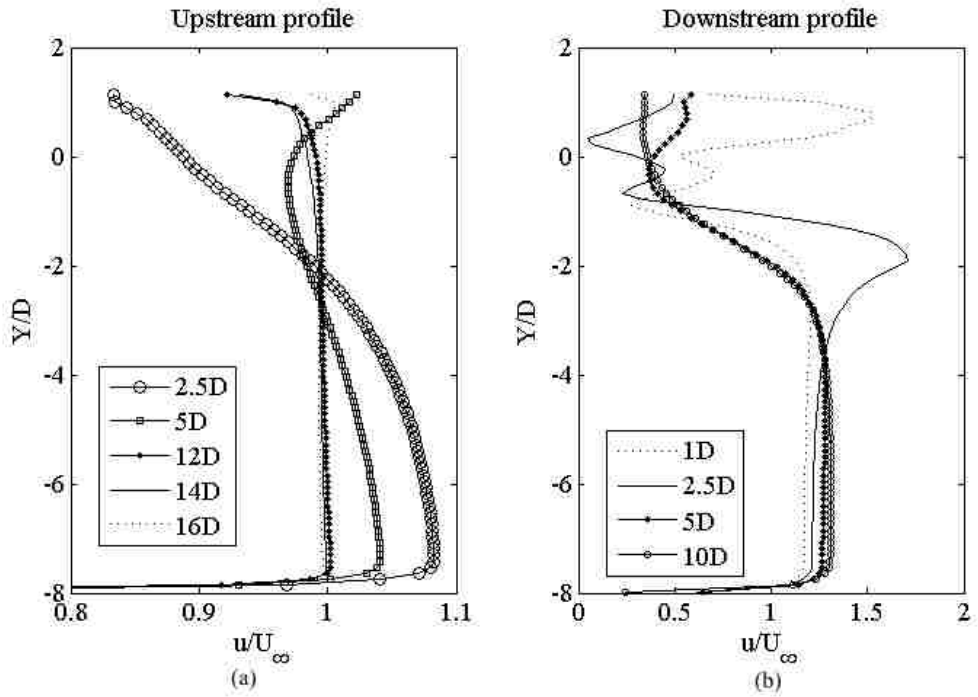

Figure 40. Normalized profiles of the time-averaged streamwise component of velocity for Fr = 0.65 at various locations (a) upstream and (b) downstream of the plate.

5.4.4 Force Coefficients and Strouhal Number

Figure 41 shows the drag and the lift coefficient as functions of time for various values of the Froude number. The mean values of the force coefficients are calculated when the periodic state is reached. Mean values are determined from the time signature of drag and the lift coefficient at flow time between 30 s to 40 s which spans nearly 6 vortex shedding cycles. It is seen that the drag coefficient (C_D) has a mean value of 3.86 in the case of Fr = 0.18 (where the plate is far away from the surface). In the case of Fr = 0.65, C_D decreases to 3.55. By further decreasing the submergence depth to the case of Fr = 0.92, C_D reduces to 2.18, corresponding to a 38% drop relative to the case of Fr = 0.65.

Results show that the influence of the free surface is significant when the plate approaches the free surface. The different vortex shedding motion effects are revealed when investigating the variation for both drag and lift coefficients. The drag and the lift coefficients display periodic behavior for all cases. When the plate is far away from the free surface, (see Figure 41(a)), the vortex shedding in this case is symmetric and very regular. When the plate is near the free surface, (see Figure 41(b) and (c)), the drag and lift coefficients have more complicated dynamics with several modes present. In Figure 41(c), the variation of the force coefficients shows that multiple wave motions are combined due to the domination of the jet-like flow formed from the free surface. Table 13 lists the mean and the root mean square (rms) of fluctuating force coefficients and the Strouhal number determined for various values of *Fr*. The drag coefficient decreases from 3.86 (*Fr* = 0.18) to 3.55 (*Fr* = 0.65) and then rapidly drops to 2.75 at *Fr* = 0.71. The drag coefficient does not change as much as *Fr* increases from 0.71 to 0.75, while it decreases substantially to 2.18 as *Fr* is increased to 0.92. The rms of C_D fluctuation at first increases to 0.51 (*Fr* = 0.65) and then drops significantly to 0.29 (*Fr* = 0.71). Another significant drop from 0.27 (*Fr* = 0.75) to 0.07 (*Fr* = 0.92) is also obtained. Past studies of flow past a circular cylinder have reported a reduction in drag coefficient and an increase in the Strouhal number when reducing the gap ratio between the cylinder and the free surface. The Strouhal number increases from 0.162 (*Fr* = 0.65) to 0.355 (*Fr* = 0.92), and simultaneously the rms of fluctuating lift force decreases. The change of vortex shedding frequency is closely related to the substantial decrease of drag coefficient. Furthermore, the lift coefficient shows that there are several modes of flow transitions

dominating the flow. This implies that the vortex shedding at shallow depths is not governed by a single mode in comparison when the prism is submerged in a nearly infinite flow domain.

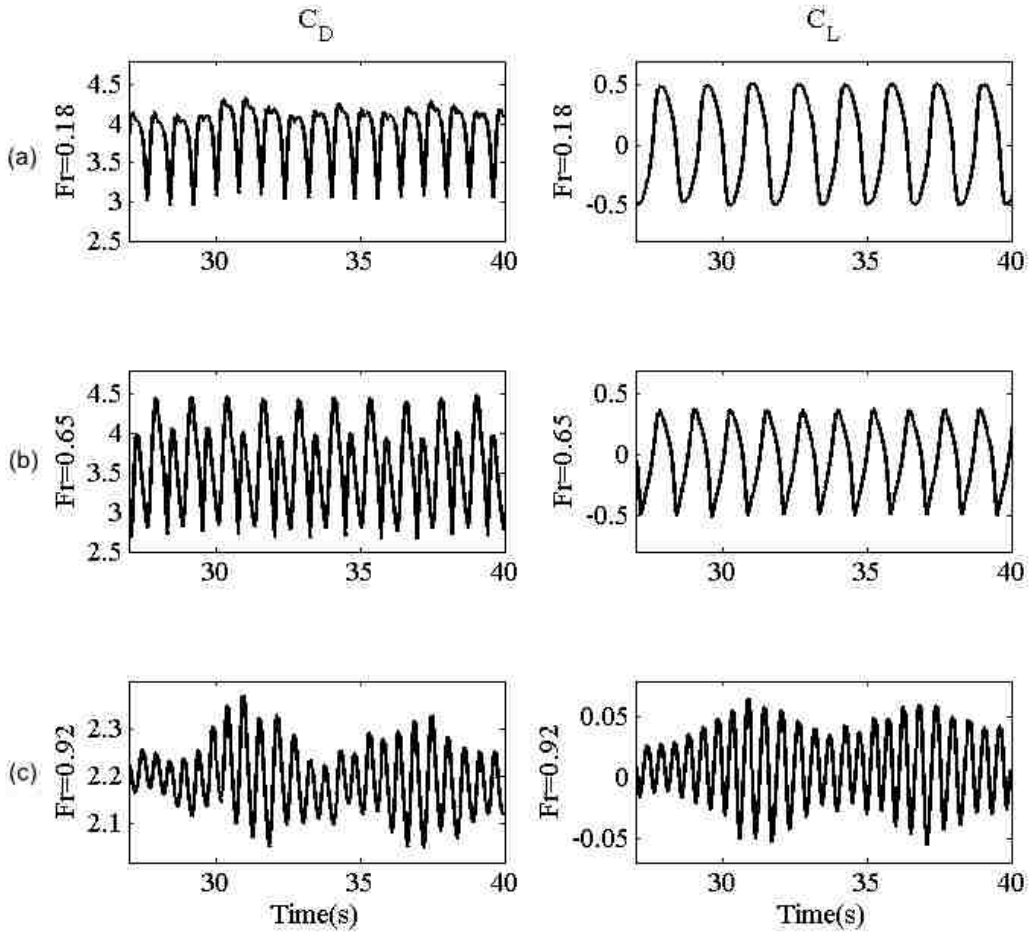

Figure 41. Drag and lift coefficients as functions of time for (a) *Fr* = 0.18 (b) *Fr* = 0.65 (c) *Fr* = 0.92.

Table 13. Mean and root mean square of fluctuating drag and lift coefficients and the Strouhal number for different values of the Froude number

	Fr = 0.18	***Fr = 0.65***	***Fr = 0.71***	***Fr = 0.75***	***Fr = 0.92***
C_D	3.86	3.55	2.75	2.65	2.18
C_{Drms}	0.36	0.51	0.29	0.27	0.07
C_L	0.00	-0.02	-0.04	-0.03	0.01
C_{Lrms}	0.38	0.28	0.17	0.14	0.03
St	0.125	0.162	0.208	0.233	0.355

The cumulative mean of drag and lift coefficient as a function of time is shown in Figure 42 for various values of *Fr*. The cumulative mean values tend to constant asymptotically, implying that the force coefficients have reached stability. The mean values of the force coefficient listed in Table 13 have a relative error less than 5% when compared to the asymptotic values of the cumulative mean of force coefficients. This discrepancy is due to the initial transient at early simulation time influences the overall cumulative mean values. As simulations are carried out further in time this difference naturally becomes smaller.

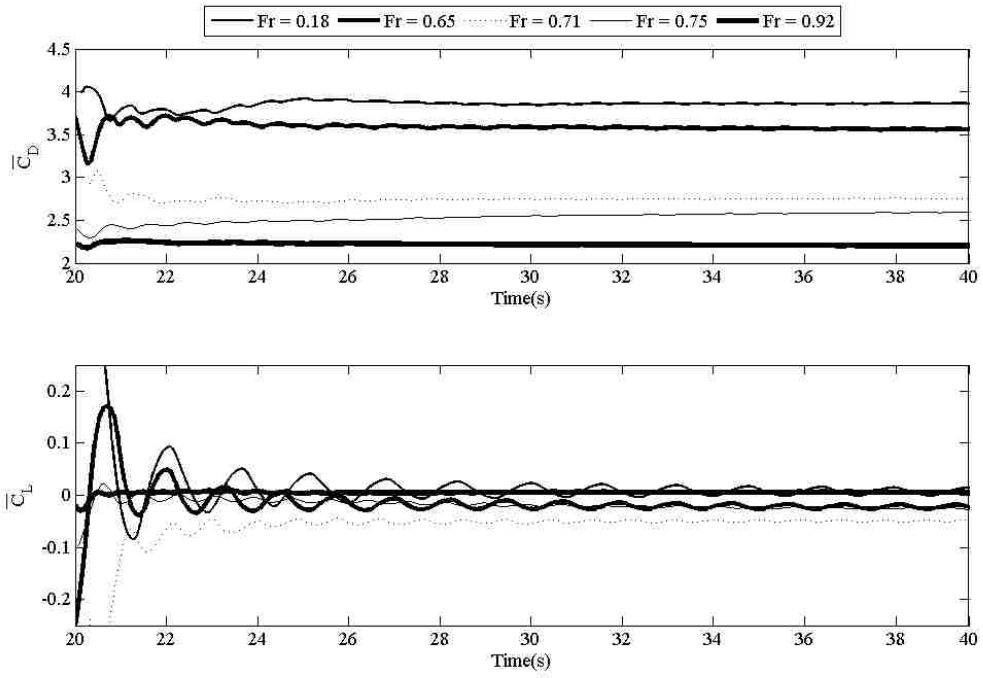

Figure 42. Cumulative mean of drag and lift coefficients for *Fr* = 0.18, 0.65, 0.71, 0.75 and 0.92.

To determine the cause of the drag coefficient reduction, a simulation is conducted with a solid surface (no-slip surface) replacing the free surface. The solid surface is placed 0.5*D* away from the top of the plate; this case would correspond to *Fr* = 0.71 if the free surface is present. The mean value of the drag coefficient is calculated to be 3.67 with the solid surface, which is much closer to the value of the drag coefficient, 3.86, for a plate in an infinite domain. As presented above the drag coefficient is 2.75 for *Fr* = 0.71. It can be concluded that the reduction in drag coefficient is not simply by the confinement. The interaction of the free surface waves and the wake flow should be the

reason for drag reduction. This does not rule out the possibility of the adverse influence of the air entrainment deep into the wake, as seen in Figure 38.

5.5 Computational Overview – Three-Dimensional

The schematic of the computational domain for three-dimensional flows past a finite plate is illustrated in Figure 43(a). The gray plane indicates the location of the free surface, which varies with the submergence depth of the plate. Above the plane is air region, where below the plane is water region. The single finite plate geometry is shown in Figure 43(b). The length, width, and height of the plate are L, w, and D, respectively. The length to height ratio (L/D) of the plate used in this study is 10. The origin of the computational domain is located at the center of the plate. The plate is located at $12D$ from the inlet, $23D$ from the outlet, $4D$ from the top surface, and $8D$ from the bottom surface. Similar to simulations done in two-dimensional flows, the upstream water velocity is U_∞ = 0.5 m/s and the air velocity is set to U_{air} = 0.01 m/s. The Reynolds number based on water velocity, U_∞, and the plate height, D, is 50,000. Simulations are conducted for three depths: $0.5D$, $0.3D$, and $0.15D$, which corresponds to Froude number of 0.71, 0.92, and 1.3, respectively. The parameter used in this study are listed in Table 14.

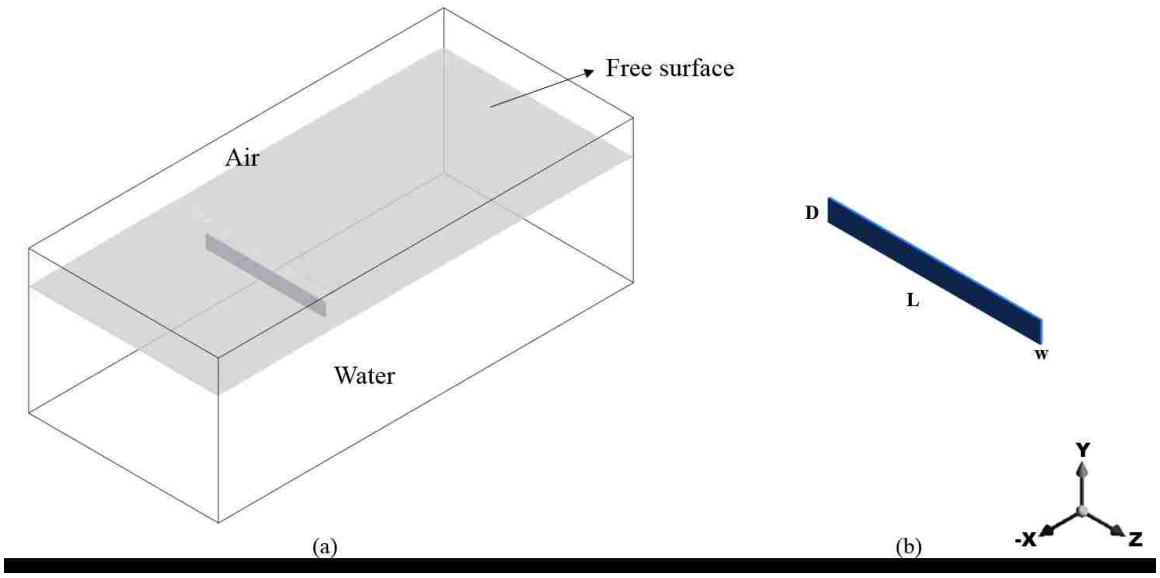

Figure 43. (a) Schematic diagram of the computational domain. (b) Plate geometry.

Table 14. Parameter values used in the simulations

Parameter	*Values*				
A	0.1	[m^2]	L	1	[m]
g	9.81	[m s^{-2}]	U_{air}	0.01	[m s^{-1}]
D	0.1	[m]	U_∞	0.5	[m s^{-1}]
d	0.05, 0.03, 0.015	[m]	w	0.01	[m]
Fr	0.71, 0.92, 1.3	[-]	ρ_2	1000	[kg m^{-3}]
Re_2	50,000	[-]	μ_2	0.001	[kg m^{-1} s^{-1}]

The boundary conditions are given in the following: the mass flow rate for both air and water are specified at the inlet. Zero gauge pressure is applied to the outlet. Depend on the plate depth, the free surface levels are defined at both inlet and outlet in the VOF model. No-slip boundary conditions are defined at the plate surface, top, and bottom surfaces of the computational domain. Periodic boundary conditions are imposed at the side surfaces of the computational domain.

The pressure-velocity coupling Semi-Implicit Method for Pressure-Linked Equations (SIMPLE) solution method is used to resolve velocity and pressure filed. Discretization of time and momentum are done through bounded central differencing and bounded second order implicit scheme. The PREssure STaggering Option (PRESTO!) scheme is used to discretize pressure equation. The modified High Resolution Interface Capturing (HRIC) discretization scheme is employed to solve the volume fraction equation. Simulations are accomplished by using ANSYS FLUENT software with LES turbulence model and VOF multiphase model.

5.6 Results and Discussions

Results for three submergence depths of the plate, Fr = 0.71, 0.92, and 1.3 are presented. Instantaneous contours and hydrodynamic forces exerted on the plate are acquired for the non-dimensional time, $\lambda = tU_\infty/D$.

5.6.1 Flow Patterns

Instantaneous isosurfaces of free surface locations for Fr = 0.71, 0.92, and 1.3 are depicted in Figure 44. Three-dimensional views are shown in Figure 44 (a-c) and side views showing only close upstream and downstream of the plate are shown in Figure 44 (d-f), respectively. Isosurfaces are acquired at air volume fraction of 0.1 with colored normalized free surface level. The free surface level is ranging from 0.1D above the original free surface to 1.2D below the original free surface. As seen in Figure 44, the surface dipped down a bit behind the plate, as it goes downstream the free surface gradually get back to the undisturbed free surface level. The surface deformation

becomes more pronounced as the plate become closer to the surface. As seen in Figure 44 (c,f), at $Fr = 1.3$ the plate is shallowly submerged, a wave is seen around the plate. The surface dipped down both upstream and downstream of the plate and the variation of the free surface level is more enhanced compare to other cases. Complicated structure are observed at the top surface of the plate, where the free surface above the plate in other cases are relatively smooth. One can conclude that the free surface effect is significant when the plate is close to the free surface.

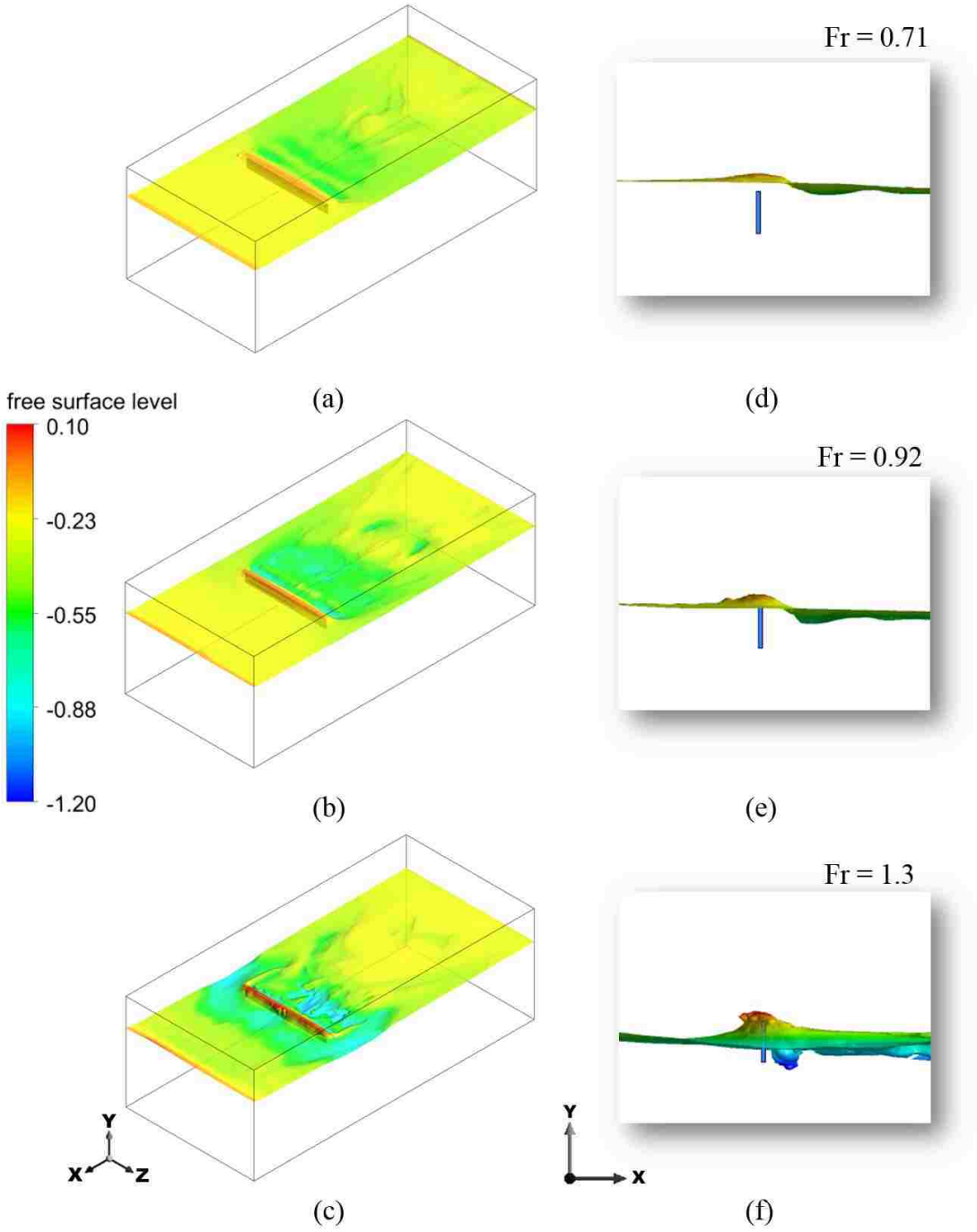

Figure 44. Instantaneous isosurfaces of air volume fraction at 0.05 colored with free surface level normalized by plate height *D*. (a,d) *Fr* = 0.71 at λ = 200 (b,e) *Fr* = 0.92 at λ = 203 (c,f) *Fr* = 1.3 at λ = 195.

Isosurfaces of Q-criterion (Q = 0.01) near a plate close to the free surface at different Froude numbers are depicted in Figure 45. Isosurfaces of Q-criterion is colored with the normalized vorticity magnitude, $\omega D/U_\infty$. As the plate gets closer to the surface, interactions between the free surface and the plate are enhanced. More small eddies and intense vorticity dynamics are observed at the free surface above the plate at Fr = 1.3, along with more surface deformation. In these three cases upper vortices generate from the plate are suppressed due to the presence of the free surface, vortices shed from the bottom of the plate expand downward and dissipate downstream. The suppression of upper vortices become pronounced as the Froude number become larger. At Fr = 1.3, the upper vortices seem to be fully suppressed. Vortex structure for the plate further away from the surface (Fr = 0.71) is more intact and regular compare to shallowly submerged cases. While the plate becomes very close to the free surface, at Fr = 1.3, the vortex structure breaks into small eddies and they are concentrated near the free surface and at the near wake region.

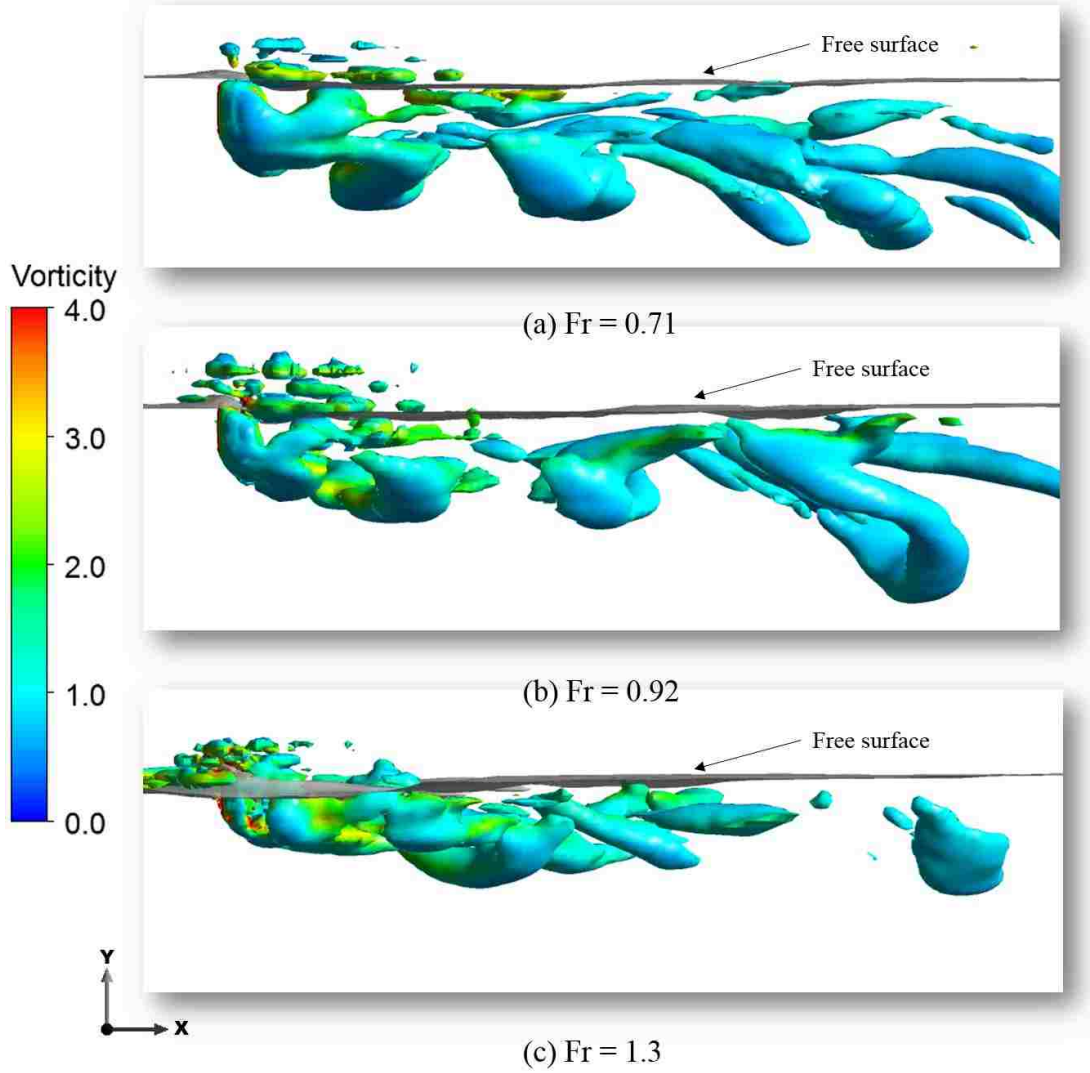

Figure 45. Isosurfaces of vortex structure at Q = 0.01 with colored normalized vorticity magnitude in side view for (a) *Fr* = 0.71 at λ = 200 (b) *Fr* = 0.92 at λ = 203 (c) *Fr* = 1.3 at λ = 195.

5.6.2 Force Coefficients

Time signatures of drag and lift coefficients for *Fr* = 0.71, 0.92, and 1.3 are depicted in Figure 46. Drag coefficients are plotted in the left column while lift coefficients are shown in the right column. Force coefficients for various *Fr* numbers, 0.71, 0.92, and 1.3, are depicted in rows from top to bottom, respectively. In general, drag coefficients for a finite plate close to a free surface are higher than that of in the unbounded domain. Time-averaged drag coefficients with standard deviation for *Fr* = 0.71, 0.92, and 1.3 are 1.61 ± 0.018, 1.73 ± 0.042, and 1.69 ± 0.18, respectively. Signatures of case *Fr* = 0.71 have regular periodic oscillating behavior (see Figure 46a,b), while for the closest case, at *Fr* = 1.3, irregular behavior such as a rapid decrease in drag coefficient is observed (see Figure 46e,f). The case of *Fr* = 1.3 has higher fluctuation in drag coefficient. Note that if a system that consists of arrays of blades that is placed close to a free surface, higher fluctuation in hydrodynamic forces exerted on the blades may lead to system failure. It is suggested that such devices should be placed in flow condition less than *Fr* number 1.3. The lift coefficient of case *Fr* = 0.71 indicate that regular vortex shedding is generated from the plate. When the plate is moving closer to the free surface, at *Fr* = 0.92 and 1.3, hydrodynamic signals become more complicated, which implied that various modes of vortex shedding occur in the flow field. For the case of *Fr* = 1.3, at the time of significant decrease in drag coefficient, a rapid increase in lift coefficient is shown, as depicted in Figure 46(f). At these instantaneous time, air entrainment is recognized near the plate.

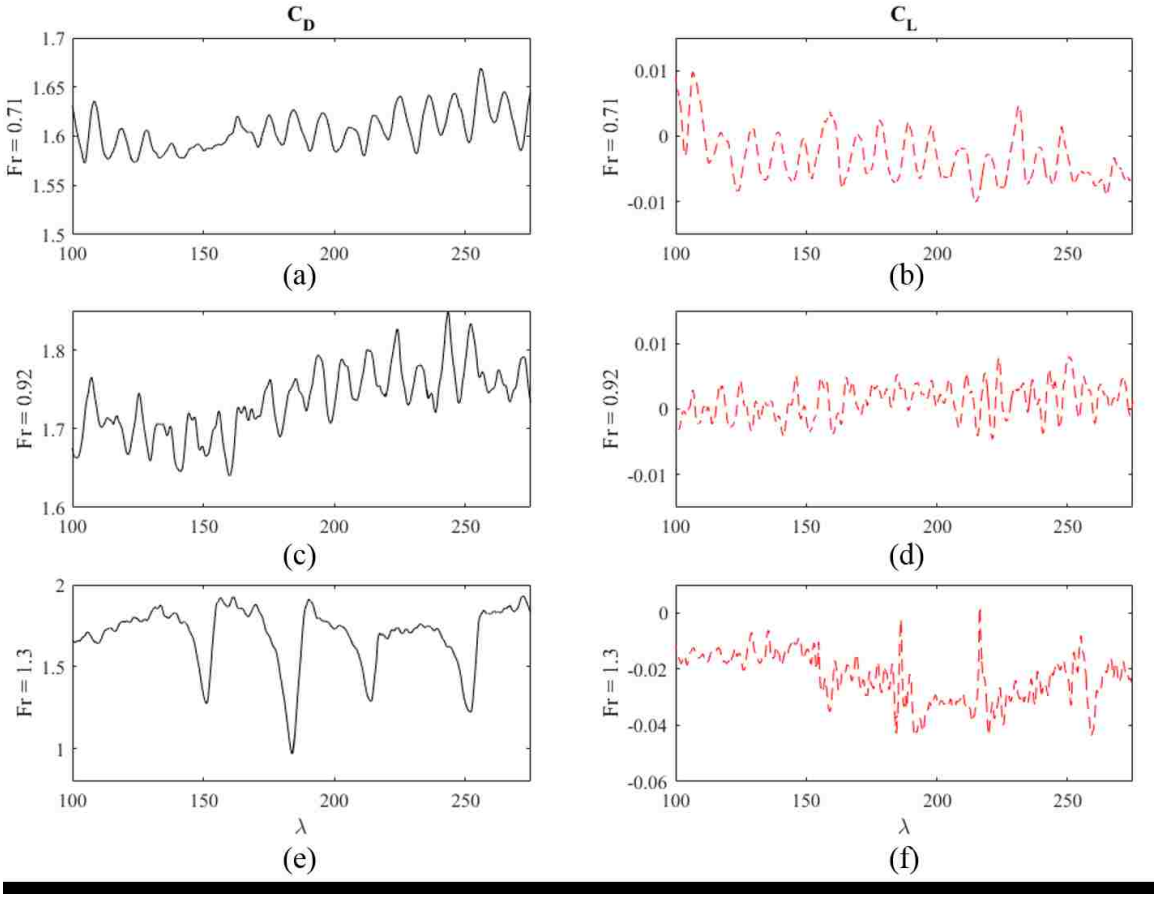

Figure 46. The drag (left column) and lift (right column) coefficients as a function of non-dimensional time, λ, for *Fr* of (a,b) 0.71, (c,d) 0.92, and (e,f) 1.3.

Free surface deformation level for the case of *Fr* = 1.3 at higher regime drag coefficient and lower drag coefficient regime are compared in Figure 47. Figure 47 depicts instantaneous isosurfaces of air volume fraction at 0.05, which colored by normalized free surface level for the case of *Fr* = 1.3 at (a) high drag regime and (b) low drag regime. At higher drag regime, the plate is fully submerged, as seen in Figure 47(a). Air upstream of the plate moves above the plate and then entrained into the water after passing the plate. However, at lower drag regime, as seen in Figure 47(b), air gathered

around the middle of the plate and then entrained into the water. Air moves under the bottom of the plate as it goes downstream. When air is entrained in the water, the drag force is decreased due to the presence of air at the center region in front of the plate. Lower pressure applied to the front of the plate results in a rapid decrease in drag coefficient.

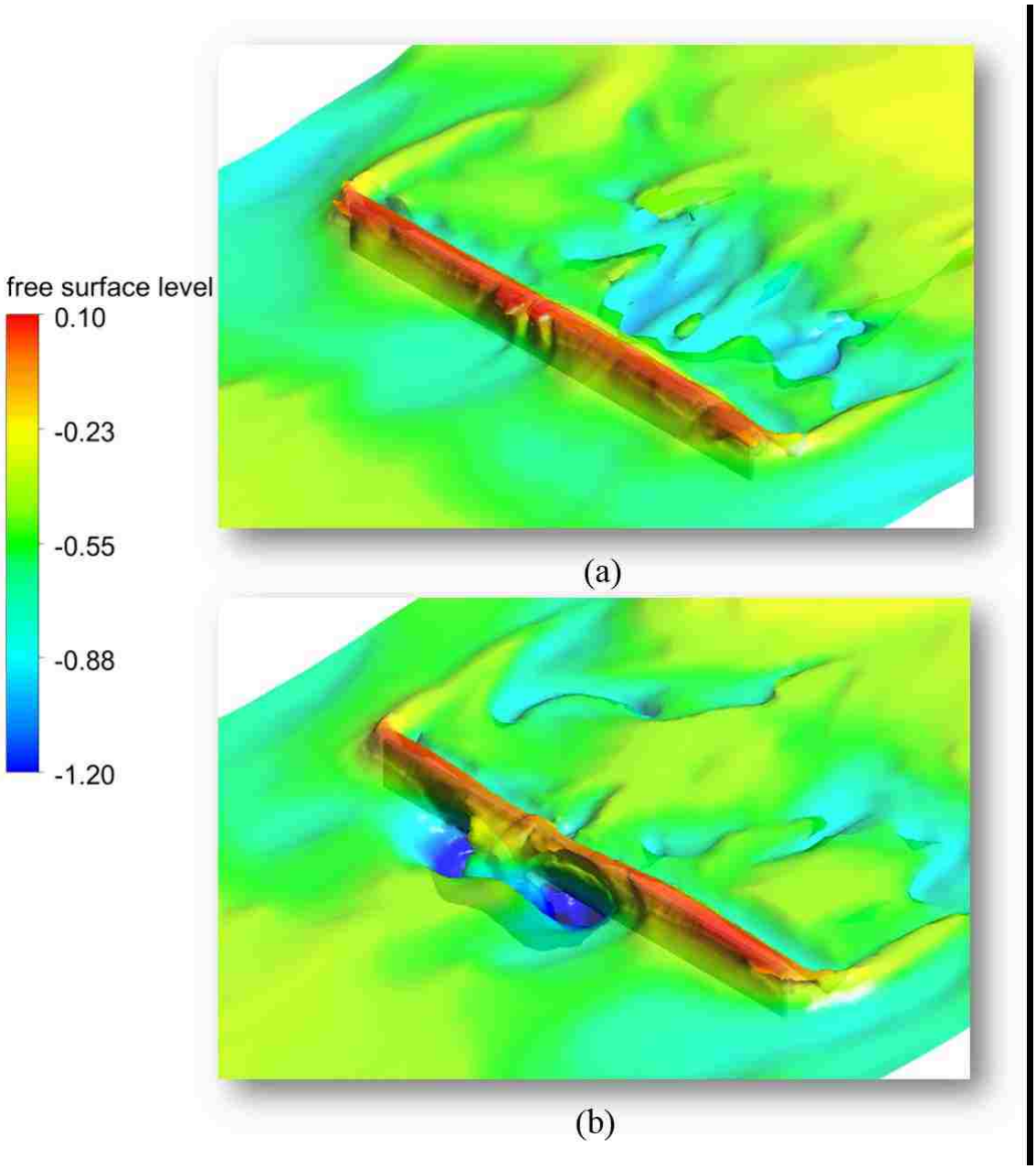

Figure 47. Free surface level for Fr = 1.30 at (a) high C_D regime at λ = 200 and (b) low C_D regime at λ = 214.

In summary, numerical simulations were performed to understand the flow structure of a plate placed near the free surface. The free surface effect on the plate was

investigated by performing simulations at 7.5*D*, 0.6*D*, 0.5*D*, 0.45*D*, 0.3*D*, and 0.15*D* depths corresponding to local Froude number values of 0.18, 0.65, 0.71, 0.75, 0.92, and 1.3. Two- and three-dimensional transient simulations were conducted for the Reynolds number of 50,000. Turbulence models, LES and k-ω SST models and VOF multiphase model were employed with a transient SIMPLE solver to solve flow past a plate close to the free surface. A three-dimensional validation simulation was conducted to compare with a previously published experimental result presented in [14]. Results for both drag and lift coefficients and the Strouhal number match well with their results.

The presented results showed that as the depth decreased from 0.6*D* (i.e., Fr = 0.65) to 0.3*D* (i.e., Fr = 0.92), the drag coefficient decreased 38% from 3.55 to 2.18. The Strouhal number increased from 0.162 to 0.355. The substantial changes observed are similar to flow past a circular cylinder close to the free surface. The variation of drag coefficient with depth was consistent with the results reported in [26]. The flow pattern observed is also consistent with the results in [29] and [30]. The wake structure for a near-surface plate is distinctly different from the wake of a deeply submerged plate. The wake flow becomes more irregular as depth decreases. The vortex formed from the top of the plate break into small eddies due to the presence of the free surface. Furthermore, a jet-like flow formed from the surface on top of the plate was observed, which weakened the upper vortices and results in large surface deformation. The presented study demonstrates that the proximity of the blades to the free surface has a profound influence on the energy harvesting devices performance in the river or ocean currents. The rapid decrease in drag coefficient occurs between a depth of 0.6*D* (Fr = 0.65) and 0.5*D* (Fr =

0.71) at the flow conditions considered. Therefore, the plate depths greater than 0.6*D* are suggested for the energy harvesting devices utilizing rectangular prism shape blades.

CHAPTER 6 CONCLUSION

Simulations for flows past a single and arrays of plates in the vicinity of surfaces are conducted in the present work. Two- and three-dimensional transient turbulence flows at Re = 50,000 were studied by k-ω SST RANS model and LES model. VOF multiphase model was used to characterize free surface flows. Finite plates, with a length to height ratio of 10, was used in all simulations. Various yaw angles of the plates and spacing ratios between upstream and downstream plates in a staggered array configuration were examined. This dissertation was mainly focused on characterizing flow patterns and hydrodynamic forces for plates that were placed close to a rigid surface or a free surface. Staggered arrays of plates under the influence of a rigid surface were examined as well. This study was able to aid in optimizing the design of marine energy harvesting devices, which consisted of multiple translating blades that operated near a free surface or beneath an offshore platform.

Based on the study of flows past an infinitely long plate and a finite plate, one can conclude that the drag coefficient of a finite plate is lower than that of an infinitely long plate. From the investigation of flows past tandem plates, it was found that the effect of spacing in tandem arrays predicted by three-dimensional simulations was drastically different from that predicted by two-dimensional modeling due to the three-dimensional effect. Higher drag coefficient values of downstream plates were obtained in three-dimensional flows. Flow transitions observed in the wake flows were responsible for the influence of spacing on drag coefficients. Different flow patterns were found with respect

to different spacings. Due to streamlining effects, drag coefficients of yawed plates were less than that of plates oriented perpendicular to oncoming flows. However, when arrays of yawed plates were placed in the flow, the overall drag coefficients were higher than those in tandem arrays. This is because of the vortex structure for arrays of yawed plates concentrated toward the center, which in turn decrease the impact on downstream plates. This could be favorable in terms of structural stability and power generation for marine current energy harvesting applications.

The wall proximity effect was investigated by performing simulations for flows past a single plate and arrays of finite plates near a moving wall. Simulations for various wall gap ratios of a single plate, S/D, range from 0.1 to 7.5, and a wall gap ratio at 1.5 with longitudinal spacing ratios, G/D, 2.5 and 5 for staggered arrays of yawed plates were conducted. The influence of the wall was varied depending on wall gaps. When the plate was placed near the wall, asymmetric flow patterns were observed. Vortices generated from the side closer to the wall were suppressed. When the gap was smaller than the wall boundary layer thickness, significant interactions between the plate and the wall boundary layer occurred. Small eddies were formed upstream near the plate. Drag coefficients varied strongly with the wall distances. At $S/D \leq 0.25$, where the wall gaps were smaller than the wall boundary layer thickness, larger fluctuations in force coefficients were observed in these cases. When the S/D increased, the highest drag coefficient value of 1.75 was found for plate at $S/D = 1.5$. When the plate was further away from the wall, as S/D increased, the drag coefficient asymptotes to the unbounded value of 1.5.

Strong interactions between the wall boundary layer and the wake of yawed plates were found when staggered arrays of yawed plates were situated close to a wall. A blade shape effect was also studied. Staggered arrays of yawed plates encountered larger drag force than those of unbounded plates. The compact design of plate arrays within marine current energy harvesting devices provided more power extraction. The present study demonstrated that while designing energy harvesting systems that operates beneath a platform or docks, the wall proximity effect should be taken into account.

The free surface effect was examined by conducting simulations for flows past a single plate at different depths beneath a free surface. Simulations in two-dimensional geometries were performed for depths at 7.5*D*, 0.6*D*, 0.5*D*, 0.45*D*, and 0.3*D*, corresponding to local Froude number values of 0.18, 0.65, 0.71, 0.75, 0.92. Finite plates that have depths at 0.5*D*, 0.3*D*, and 0.15*D*, which corresponds to Froude number of 0.71, 0.92, and 1.3, were simulated in three-dimensional flows. Results showed that as the depth decreased, the drag coefficient decreased with an increase in Strouhal number. The wake structure for a near-free surface plate is distinctly different from the wake of a deeply submerged plate. Similar to the flow patterns observed for flows past plates near a wall, the presence of the free surface breaks the symmetry of vortex shedding, results in irregular wake structures. A jet-like flow formed from the surface on top of the plate was observed, which weakened the upper vortices and results in larger surface deformation. It is found in three-dimensional results that when the finite plate was placed 0.15*D* (*Fr* = 1.3) under the free surface, the drag coefficient experienced significant decrease at some instantaneous time. This is due to the air entrained in the water and passed through the

bottom of the plate. Higher fluctuation was also observed in force coefficients. This could lead to structure failure when the system was operating under this flow condition. Therefore, plate depths larger than $0.15D$ were suggested for the energy harvesting devices utilizing flat shape blades.

The present study demonstrated the proximity of blades to a rigid surface and a free surface had a profound influence on the performance of energy harvesting devices in marine current applications. In addition, orientation, arrangement, spacing, and shape of the blades for such systems were critical variables in designing and optimizing of energy harvesting mechanisms.

REFERENCES

[1] Rodi, W., *Large-eddy simulations of the flow past bluff bodies: State of the art.* Jsme International Journal Series B-Fluids and Thermal Engineering, 1998. **41**(2): p. 361-374.

[2] Fage, A. and F.C. Johansen, *On the flow of air behind an inclined flat plate of infinite span.* Proceedings of the Royal Society A: Mathematical, Physical and Engineering Sciences, 1927. **116**(773): p. 170-197.

[3] Knisely, C.W., *Strouhal numbers of rectangular cylinders at incidence - a review and new data.* Journal of Fluids and Structures, 1990. **4**(4): p. 371-393.

[4] Narasimhamurthy, V.D. and H.I. Andersson, *Numerical simulation of the turbulent wake behind a normal flat plate.* International Journal of Heat and Fluid Flow, 2009. **30**(6): p. 1037-1043.

[5] Najjar, F.M. and S.P. Vanka, *Simulations of the unsteady separated flow past a normal flat-plate.* International Journal for Numerical Methods in Fluids, 1995. **21**(7): p. 525-547.

[6] Tian, X., et al., *Unsteady RANS simulations of flow around rectangular cylinders with different aspect ratios.* Ocean Engineering, 2013. **58**: p. 208-216.

[7] Sakamoto, H., H. Hainu, and Y. Obata, *Fluctuating forces acting on two square prisms in a tandem arrangement.* Journal of Wind Engineering and Industrial Aerodynamics, 1987. **26**(1): p. 85-103.

[8] Liu, C.H. and J.M. Chen, *Observations of hysteresis in flow around two square cylinders in a tandem arrangement.* Journal of Wind Engineering and Industrial Aerodynamics, 2002. **90**(9): p. 1019-1050.

[9] Yen, S.C., K.C. San, and T.H. Chuang, *Interactions of tandem square cylinders at low Reynolds numbers.* Experimental Thermal and Fluid Science, 2008. **32**(4): p. 927-938.

[10] Sohankar, A., *A LES study of the flow interference between tandem square cylinder pairs.* Theoretical and Computational Fluid Dynamics, 2014. **28**(5): p. 531-548.

[11] Sumner, D., *Two circular cylinders in cross-flow: A review.* Journal of Fluids and Structures, 2010. **26**(6): p. 849-899.

[12] Zhao, M., et al., *Numerical simulation of viscous flow past two circular cylinders of different diameters.* Applied Ocean Research, 2005. **27**(1): p. 39-55.

[13] Auteri, F., et al., *Interacting wakes of two normal flat plates an investigation based on phase averaging of LDA signals.* Journal of Visualization, 2009. **12**(4): p. 307-321.

[14] Malavasi, S. and A. Guadagnini, *Interactions between a rectangular cylinder and a free-surface flow.* Journal of Fluids and Structures, 2007. **23**(8): p. 1137-1148.

[15] Liu, I.-H., et al., *Flow past a plate in the vicinity of a free surface.* Ocean Engineering, 2016. **111**: p. 323-334.

[16] Bhattacharyya, S. and D.K. Maiti, *Shear flow past a square cylinder near a wall.* International Journal of Engineering Science, 2004. **42**(19–20): p. 2119-2134.

[17] Bhattacharyya, S. and D.K. Maiti, *Vortex shedding from a square cylinder in presence of a moving wall.* International Journal for Numerical Methods in Fluids, 2005. **48**(9): p. 985-1000.

[18] Bosch, G., M. Kappler, and W. Rodi, *Experiments on the flow past a square cylinder placed near a wall.* Experimental Thermal and Fluid Science, 1996. **13**(3): p. 292-305.

[19] Mahir, N., *Three-dimensional flow around a square cylinder near a wall.* Ocean Engineering, 2009. **36**(5): p. 357-367.

[20] Shi, L.L., Y.Z. Liu, and J.J. Wan, *Influence of wall proximity on characteristics of wake behind a square cylinder: PIV measurements and POD analysis.* Experimental Thermal and Fluid Science, 2010. **34**(1): p. 28-36.

[21] Maiti, D.K. and R. Bhatt, *Numerical study on flow and aerodynamic characteristics: Square cylinder and eddy-promoting rectangular cylinder in tandem near wall.* Aerospace Science and Technology, 2014. **36**: p. 5-20.

[22] Agelinchaab, M., et al., *Turbulent wake of rectangular cylinder near plane wall and free surface.* Aiaa Journal, 2008. **46**(1): p. 104-117.

[23] Bayraktar, S., et al., *Wall proximity effects on flow over cylinders with different cross sections.* Canadian Journal of Physics, 2014. **92**(10): p. 1141-1148.

[24] Kumaran, M. and S. Vengadesan, *Flow characteristics behind rectangular cylinder placed near a wall.* Numerical Heat Transfer Part a-Applications, 2007. **52**(7): p. 643-660.

[25] Martinuzzi, R.J., S.C.C. Bailey, and G.A. Kopp, *Influence of wall proximity on vortex shedding from a square cylinder.* Experiments in Fluids, 2003. **34**(5): p. 585-596.

[26] Miyata, H., N. Shikazono, and M. Kanai, *Forces on a circular cylinder advancing steadily beneath the free-surface.* Ocean Engineering, 1990. **17**(1–2): p. 81-104.

[27] Arslan, T., et al., *Turbulent Flow Around a Semi-Submerged Rectangular Cylinder.* Journal of Offshore Mechanics and Arctic Engineering-Transactions of the Asme, 2013. **135**(4).

[28] Riglin, J., et al., *Characterization of a micro-hydrokinetic turbine in close proximity to the free surface.* Ocean Engineering, 2015. **110, Part A**: p. 270-280.

[29] Sheridan, J., J.C. Lin, and D. Rockwell, *Flow past a cylinder close to a free surface.* Journal of Fluid Mechanics, 1997. **330**: p. 1-30.

[30] Reichl, P., K. Hourigan, and M.C. Thompson, *Flow past a cylinder close to a free surface.* Journal of Fluid Mechanics, 2005. **533**(00): p. 269-296.

[31] Negri, M., F. Cozzi, and S. Malavasi, *Self-synchronized phase averaging of PIV measurements in the base region of a rectangular cylinder.* Meccanica, 2010. **46**(2): p. 423-435.

[32] Shirakashi, M., A. Hasegawa, and S. Wakiya, *Effect of the secondary flow on Karman vortex shedding from a yawed cylinder.* Bulletin of JSME, 1986. **29**(250): p. 1124-1128.

[33] Yeo, D. and N.P. Jones, *Investigation on 3-D characteristics of flow around a yawed and inclined circular cylinder.* Journal of Wind Engineering and Industrial Aerodynamics, 2008. **96**(10-11): p. 1947-1960.

[34] Zhao, M., L. Cheng, and T.M. Zhou, *Direct numerical simulation of three-dimensional flow past a yawed circular cylinder of infinite length.* Journal of Fluids and Structures, 2009. **25**(5): p. 831-847.

[35] Jordan, S.A., *Transition to turbulence in the separated shear layers of yawed circular cylinders.* International Journal of Heat and Fluid Flow, 2010. **31**(4): p. 489-498.

[36] Wang, H.F., et al., *Effect of initial conditions on interaction between a boundary layer and a wall-mounted finite-length-cylinder wake.* Physics of Fluids, 2006. **18**(6): p. 065106.

[37] McClean, J.F. and D. Sumner, *An experimental investigation of aspect ratio and incidence angle effects for the flow around surface-mounted finite-height square prisms.* Journal of Fluids Engineering, 2014. **136**(8): p. 081206.

[38] Liu, I.H. and A. Oztekin, *Three-dimensional transient flows past plates translating near a wall.* Ocean Engineering, 2018. **159**: p. 9-21.

[39] Sumner, D., *Flow above the free end of a surface-mounted finite-height circular cylinder: A review.* Journal of Fluids and Structures, 2013. **43**: p. 41-63.

[40] Kawamura, T., et al., *Cylinder height greater than turbulent boundary-layer thickness - Flow around a finite circular-cylinder on a flat-plate.* Bulletin of the Jsme-Japan Society of Mechanical Engineers, 1984. **27**(232): p. 2142-2151.

[41] Rostamy, N., et al. *Flow above the free end of a surface-mounted square prism*. in *Proceedings of the 7th International Colloquium on Bluff Body Aerodynamics and Applications (BBAA7)*. 2012. Shanghai, China.

[42] Zdravkovich, M.M., et al., *Flow past short circular cylinders with two free ends.* Journal of Fluid Mechanics, 1989. **203**: p. 557-575.

[43] Inoue, O. and A. Sakuragi, *Vortex shedding from a circular cylinder of finite length at low Reynolds numbers.* Physics of Fluids, 2008. **20**(3): p. 033601.

[44] Wang, H.F. and Y. Zhou, *The finite-length square cylinder near wake.* Journal of Fluid Mechanics, 2009. **638**: p. 453.

[45] Hu, G., et al., *Large eddy simulation of flow around an inclined finite square cylinder.* Journal of Wind Engineering and Industrial Aerodynamics, 2015. **146**: p. 172-184.

[46] Menter, F.R., *Zonal two equation k-ω turbulence models for aerodynamic flows.* AIAA 24th Fluid Dynamics Conference, 1993.

[47] Menter, F.R., *Two-equation eddy-viscosity turbulence models for engineering applications.* AIAA Journal, 1994. **32**(8): p. 1598-1605.

[48] Wilcox, D.C., *Turbulence modeling for CFD*. 3rd ed. ed. 2006, La Cãnada, Calif.: DCW Industries.

[49] Schleicher, W., et al., *Characteristics of a micro-hydro turbine.* Journal of Renewable and Sustainable Energy, 2014. **6**(1): p. 1-14.

[50] Schleicher, W.C., et al., *Design and simulation of a micro hydrokinetic turbine*, in *1st Marine Energy Technology Symposium*. 2013: Washington, D.C.

[51] Schleicher, W.C., J.D. Riglin, and A. Oztekin, *Numerical Characterization of a Preliminary Portable Micro-hydrokinetic Turbine Rotor Design.* Renewable Energy, 2014.

[52] Schleicher, W.C., J.D. Riglin, and A. Oztekin, *Numerical characterization of a preliminary portable micro-hydrokinetic turbine rotor design.* Renewable Energy, 2015. **76**(0): p. 234-241.

[53] Schleicher, W.C., et al. *Numerical Optimization of a Portible Hydrokinetic Turbine*. in *2nd Marine Energy Technology Symposium*. 2014. Seattle, WA.

[54] Nicoud, F. and F. Ducros, *Subgrid-scale stress modelling based on the square of the velocity gradient tensor.* Flow Turbulence and Combustion, 1999. **62**(3): p. 183-200.

[55] Hirt, C.W. and B.D. Nichols, *Volume of fluid (VOF) method for the dynamics of free boundaries.* Journal of Computational Physics, 1981. **39**(1): p. 201-225.

[56] Monaghan, J.J., *Simulating Free Surface Flows with SPH.* Journal of Computational Physics, 1994. **110**(2): p. 399-406.

[57] *ANSYS FLUENT Theory Guide 14.5.* 2012.

[58] *ANSYS FLUENT User Guide 14.5.* 2012.

[59] Greenshields, C.J., *The Open Source CFD Toolbox, Programmer's Guide, Version 3.0.1*. 2015.

[60] Najjar, F.M. and S. Balachandar, *Low-frequency unsteadiness in the wake of a normal flat plate.* Journal of Fluid Mechanics, 1998. **370**: p. 101-147.

[61] Tian, X.L., et al., *Large-eddy simulation of the flow normal to a flat plate including corner effects at a high Reynolds number.* Journal of Fluids and Structures, 2014. **49**(0): p. 149-169.

[62] Hunt, J.C.R., A.A. Wray, and P. Moin, *Eddies, streams, and convergence zones in turbulent flows*, in *1988 Summer program of the center for turbulent research*. 1988: NASA Ames/ Stanford University. p. 193-208.

[63] Hemmati, A., D.H. Wood, and R.J. Martinuzzi, *Effect of side-edge vortices and secondary induced flow on the wake of normal thin flat plates.* International Journal of Heat and Fluid Flow, 2016. **61, Part A**: p. 197-212.

[64] Lei, C., L. Cheng, and K. Kavanagh, *Re-examination of the effect of a plane boundary on force and vortex shedding of a circular cylinder.* Journal of Wind Engineering and Industrial Aerodynamics, 1999. **80**(3): p. 263-286.

[65] Nishino, T., G.T. Roberts, and X. Zhang, *Vortex shedding from a circular cylinder near a moving ground.* Physics of Fluids, 2007. **19**(2): p. 025103.

[66] Bimbato, A.M., L.A.A. Pereira, and M.H. Hirata, *Simulation of viscous flow around a circular cylinder near a moving ground.* Journal of the Brazilian Society of Mechanical Sciences and Engineering, 2009. **31**(3): p. 243-252.

[67] Ong, M.C., et al., *Numerical simulation of flow around a circular cylinder close to a flat seabed at high Reynolds numbers using a k–ε model.* Coastal Engineering, 2010. **57**(10): p. 931-947.

[68] Rao, A., et al., *The flow past a circular cylinder translating at different heights above a wall.* Journal of Fluids and Structures, 2013. **41**: p. 9-21.

[69] Wang, X.K., et al., *Influence of wall proximity on flow around two tandem circular cylinders.* Ocean Engineering, 2015. **94**: p. 36-50.

[70] D'Souza, J.E., R.K. Jaiman, and C.K. Mak, *Dynamics of tandem cylinders in the vicinity of a plane moving wall.* Computers & Fluids, 2016. **124**: p. 117-135.

[71] Liu, I.H., B. Attiya, and A. Oztekin, *Transient flows past arrays of yawed finite prisms.* Canadian Journal of Physics, 2017. **95**(12): p. 1285-1298.

[72] Devarakonda, R. and J.A.C. Humphrey, *Experimental study of turbulent flow in the near wakes of single and tandem prisms.* International Journal of Heat and Fluid Flow, 1996. **17**(3): p. 219-227.

[73] Nikfarjam, F. and A. Sohankar, *Study of hysteresis associated with power-law fluids past square prisms arranged in tandem.* Ocean Engineering, 2015. **104**: p. 698-713.

[74] Celik, I.B., et al., *Procedure for estimation and reporting of uncertainty due to discretization in CFD applications.* Journal of Fluids Engineering-Transactions of the Asme, 2008. **130**(7).

[75] Tamura, T., I. Ohta, and K. Kuwahara, *On the reliability of two-dimensional simulation for unsteady flows around a cylinder-type structure.* Journal of Wind Engineering and Industrial Aerodynamics, 1990. **35**: p. 275-298.

[76] Mittal, R. and S. Balachandar, *Effect of three-dimensionality on the lift and drag of nominally two-dimensional cylinders.* Physics of Fluids (1994-present), 1995. **7**(8): p. 1841-1865.

[77] Bosch, G. and W. Rodi, *Simulation of vortex shedding past a square cylinder with different turbulence models.* International Journal for Numerical Methods in Fluids, 1998. **28**(4): p. 601-616.

Vita

I-Han Liu was born on April 25, 1985 in Tainan, Taiwan. Her father is Jung-Tsai Liu and mother is Mei-Ying Hung. After attended National Tainan Girls' Senior High School, she entered National Cheng Kung University and studied in mechanical engineering in Tainan, Taiwan. She received her Bachelor of Science degree in Mechanical Engineering in 2008. After that, she joined Servo Control Laboratory in National Cheng Kung University. She completed her master thesis, title "Planning and implementation of motion trajectory based on C^2 PH spline", and graduated with her Master of Science degree in 2010. Upon graduating, she worked as a research assistant in Electric Motor Technology Research Center until 2011.

I-Han then enrolled at Lehigh University in Bethlehem, Pennsylvania in August 2011. There, she met her advisor Dr. Alparslan Oztekin and worked on simulations of fluid-structure interactions. She has successfully defended her dissertation on December 1st, 2017.